

ISSN 1913-1844 (Print)
ISSN 1913-1852 (Online)

MODERN APPLIED SCIENCE

**Vol. 3, No. 9
September 2009**



Canadian Center of Science and Education

Editorial Board

- Abdul Talib Bon Universiti Tun Hussein Onn Malaysia, Malaysia
- Ahmad Mujahid Ahmad Zaidi Universiti Tun Hussein Onn Malaysia, Malaysia
- Alessandra Crosato Delft University of Technology, the Netherlands
- J S Prakash Sri Bhagawan Mahaveer Jain College of Engineering, India
- Jiantao Guo The Scripps Research Institute, United States
- Justin Madigan Intel, United States
- K.V. Ramana Rao University of Rajasthan, India
- Lim Hwee San Universiti Sains Malaysia, Malaysia
- Mohamed S. Gaafar National Institute of Standards (NIS), Egypt
- Moussaoui Abdelkrim University of Guelma, Algeria
- Musa Mailah Universiti Teknologi Malaysia, Malaysia
- Panagiotis Vlamos Ionian University, Greece
- Peter Kusch Bonn-Rhein-Sieg University of Applied Sciences, Germany
- Rajiv Pandey Indian Council of Forestry Research and Education, India
- Stefanos Dailianis University of Patras, Greece
- Sujatha. C.H Cochin University of Science and Technology, India
- Sundus H Ahmed Ministry of Science and Technology, Iraq
- Susan Sun Canadian Center of Science and Education, Canada
- Sutopo Hadi University of Lampung, Indonesia
- Wichian Sittiprapaporn Mahidol University, Thailand



Contents

Narrowband Elliptic Bandpass Filter Using Dual-Mode Microstrip Square Loop Resonator for WiMax Application <i>Babak Kazemi Esfeh, Alyani Ismail & Raja Syamsul Azmir Raja Abdullah</i>	2
The Implement of MPEG-4 Video Encoding Based on NiosII Embedded Platform <i>Fugang Duan & Zhan Shi</i>	11
Optimal Design of Capacitive Micro Cantilever Beam Accelerometer <i>Othman Sidek, Muhamad Azman Miskam, H.M.T. Khaleed, Mohd Fauzi Alias & Shukri Korakkottil Kunhi Mohd</i>	16
Dynamic Texture Segmentation Using Fourier Transform <i>Jianghong Li, Liang Chen & Yuanhu Cai</i>	29
Recovery of Nickel (II) Ions from Electroplating Rinse Water Using Hectorite Clay <i>V.Ramamurthi, P. Gomathi Priya, S.Saranya & C.Ahmed Basha</i>	37
Study on Design Method of SRC Abnormal Exterior Joint of Large-scale Thermal Power Plant Frame-bent Structure <i>Xiaoli Yang, Guoliang Bai & Hongxing Li</i>	52
Electrospinning Preparation of LaFeO ₃ Nanofibers <i>Jinxian Wang, Xiangting Dong, Zhen Qu, Guixia Liu & Wensheng Yu</i>	65
A New Method of Hierarchical Text Clustering Based on Lsa-Hgsom <i>Jianfeng Wang, Lina Ma, Xinye Li, Yangxiu Zhou & Dong Qiao</i>	72
Design of the License Plate Recognition Platform Based on the DSP Embedded System <i>Zhikun Zhang & Qilan Huang</i>	78
Optimal Programming Models for Portfolio Selection with Uncertain Chance Constraint <i>Limei Yan</i>	84
Pattern Synthesis of Sparse Phased Array Antenna Using Genetic Algorithms <i>Rongcang Han</i>	91
The Performance Study of Hybrid-driving Differential Gear Trains <i>Lei Wang, Jiancheng Yang & Xiaoqin Han</i>	95
The Model-Matching Error and Optimal Solution in Locally Convex Space <i>Lixin Ma</i>	103
Higher Education Tuition Standard Model Analysis <i>Dongping Wang & Tao Ma</i>	111



Narrowband Elliptic Bandpass Filter Using Dual-Mode Microstrip Square Loop Resonator for WiMax Application

Babak Kazemi Esfeh

Department of Computer and Communication Systems Engineering

Faculty of Engineering, Universiti Putra Malaysia

43400 Serdang, Malaysia

Tel: 60-3-8946-4352, Fax: 60-3-8656-7127 E-mail: kiaertebat2004@yahoo.com

Alyani Ismail

Department of Computer and Communication Systems Engineering

Faculty of Engineering, Universiti Putra Malaysia

43400 Serdang, Malaysia

Tel: 60-3-8946-4352, Fax: 60-3-8656-7127 E-mail: alyani@eng.upm.edu.my

Raja Syamsul Azmir Raja Abdullah

Department of Computer and Communication Systems Engineering

Faculty of Engineering, Universiti Putra Malaysia

43400 Serdang, Malaysia

Tel: 60-3-8946-4352, Fax: 60-3-8656-7127 E-mail: rsa@eng.upm.edu.my

Abstract

In this paper, a narrowband bandpass filter using dual-mode microstrip square loop resonator is proposed. This structure has a 5.1% fractional bandwidth at 2.3GHz. By using some simple techniques, the optimum results will be achieved. The dual-mode resonator will be produced by adding a square patch inside the loop resonator. The simulation and measurement results are also presented. The filter is fabricated on RT/Duroid 6010 substrate having a relative dielectric constant of 10.2 and 0.635 mm thickness. The final dimension is measured at 19.65 mm × 19.65 mm. The minimum measured insertion loss is 1.68 dB and return loss obtained is better than -20 dB, where experimental results and simulated values are in good agreement.

Keywords: Dual-mode bandpass filter

1. Introduction

In comparison with waveguide filters, microstrip filters are smaller, but in some applications, there are needs to have smaller microstrip filters. Nowadays satellite and mobile communication systems are such applications that size reduction is of primary importance (Pozar, 2005). Of course, in addition to size reduction many other parameters in filter designing should be considered, such as low insertion loss, high return loss and high rejection band, where these are the characteristics of a good filter. Furthermore, lightweight and cost-effective filters are always desired. Although miniaturization of microstrip filters can be achieved by using high dielectric constant substrates, reduction in size with changing the filters geometry is more desirable, because high dielectric permittivity will often introduce more surface waves and losses. One useful method to achieve a compact size in filter designing is to have its different parts bended. This could be an optimum solution to get more compact in sizes especially for filters with stubs and long straight transmission lines. Ultra-wideband filters reported in (Razalli, 2008) and wideband filter reported in (El-Shaarawy, 2008) are among the structures making use of method of bending the lines. On the other hand, filters using dual-mode microstrip ring or square loop resonator are other techniques of minimizing microstrip filter structures (Hong, 1995).

The main advantage of using these types of resonators is that in dual-mode resonator, each resonator acts as a double tuned resonant circuit and therefore, an n -degree filter can be achieved in more compact configurations and less complicated due to the halved number of resonators (Hong, 2001). Various designs of dual-band filters are widely used as necessary filters in wireless industry and communication systems. A major portion of these designs utilizes dual-mode resonators. Among dual-mode resonators, those using patch, attract more interest and are used in both single band and dual-band filters (Chen, 2007). In this paper, a square form of dual-mode microstrip loop resonator with additional square patch perturbation technique for WiMax application is proposed with the aim to provide simple configuration with compactness in nature.

2. Dual-Mode Microstrip Resonators

A microstrip dual-mode resonator in any shape, having symmetry in two dimension (2-D), can be described by Wheeler’s cavity model. In this model, the top and bottom of the cavity are complete electric walls and the other sides are perfect magnetic walls. Therefore, three parameters, namely E_z , H_x , and H_y represent the Electro-Magnetic (EM) fields inside the cavity in terms of TM_{mn0}^z modes. Different modes introduce limitless resonant frequencies, which can be expressed by (Hong, 2001)

$$f_{res} = \frac{c}{2\pi\sqrt{\mu\epsilon_{eff}}} \sqrt{\left(\frac{m\pi}{a}\right)^2 + \left(\frac{n\pi}{a}\right)^2} \tag{1}$$

Where μ and ϵ_{eff} are permeability and effective dielectric constant of the used substrate respectively, and a is the effective width of the cavity.

By substituting proper values for m and n , equal frequencies can be obtained. For instance, $f_{100} = f_{010}$ and $f_{110} = f_{101}$. These modes are degenerate modes that have the same resonant frequency with orthogonal field distributions. Therefore, they have no coupling and no effect to each other. When some perturbations are added to the symmetry of the structure, the field distributions of them will be no longer orthogonal and couple to each other. In this condition, two coupled degenerate modes act like two coupled resonators and a two-pole dual-mode microstrip filter can be achieved. This is the simplest dual-mode bandpass filter using a single dual-mode resonator (Hong, 2001, Wolff, 1971 and Curtis, 1991). Figure 1 illustrates the equivalent lumped elements of coupled degenerate modes. The field theory for the ring resonator has been presented by Wolff and Knoppik (Wolff, 1971). In this theory only the frequency modes of the annular ring resonator has been derived. For closed loop resonators in shape of n -side polygon, because of their complex boundary condition, it is difficult to use magnetic-wall model to obtain the frequency modes. Thus, the best way is that they be considered as a special case of an annular ring resonator, though it is not a precise approximation (Chang, 2004). It is obvious that as n increases, better approximation can be achieved.

3. Design of Dual-Mode Microstrip Square Loop Resonator

The design of the proposed dual-mode microstrip resonator has been conducted for WiMax operating frequency of 2.3GHz and fabricated on a RT/Duroid substrate having 0.635mm thickness and a relative dielectric constant of 10.2. The layout of the resonator is depicted in Figure 2(a). It is shown in Figure 2(a) that the resonator is excited by using gap-coupling method where input port, *port 1* and output port, *Port 2* are spaced with a gap, G symmetrically on each side.

The resonator (basic part of our filter), is designed to resonate at 2.3GHz. Equations (2) and (3) are used to synthesize W/h (the conductor width and substrate thickness of microstrip) in terms of characteristic impedance (Z_0) and substrate dielectric permittivity (ϵ_r) (Hong, 2001),

$$\frac{W}{h} = \frac{8e^A}{e^{2A}-2} \quad \left(\frac{W}{h} \leq 2\right) \tag{2}$$

$$A = \frac{Z_0}{60} \sqrt{\frac{\epsilon_r-1}{2} + \frac{\epsilon_r-1}{\epsilon_r+1} \left(0.23 + \frac{0.11}{\epsilon_r}\right)} \tag{3}$$

The circumference of the ring resonator ℓ_r is calculated according to the following expression (chang, 2004):

$$\ell_r = n\lambda_g \tag{4}$$

Where n is the mode number and λ_g is the guided wavelength. The design is done for the first mode. The trace width (W) of 0.576 mm will produce a 50Ω characteristic impedance line and each side of the square loop resonator is $a = 12.2$ mm (one quarter of wavelength). The structure shown in Figure 2(a) is simulated using EM simulator software (EM, 2006) and simulated insertion loss and return loss for different values of feedlines gap, G are shown in Figure 2(b).

As can be seen in the simulation results, coupling gaps between the resonator and feedlines, G affect the resonant frequency. With smaller gap size, the insertion loss is lower and the resonant frequency is more affected, and bigger gap size causes higher insertion loss and lower affection on the resonant frequency. Therefore, by adjusting the gap sizes the

desired values for insertion loss and resonant frequency can be achieved.

4. Design of Narrowband Elliptic Bandpass Filter Using Dual-Mode Microstrip Square Loop Resonator

The structure of the single mode resonator shown in Figure 2(a) has been transformed into a dual-mode resonator shown in Figure 3 to create a narrowband bandpass filter. The feedlines positions excite two degenerate modes, T_{100}^z , and T_{010}^z . When $d = 0$, there is no perturbation and just a single mode is excited. In the T_{100}^z mode, the *port 1* is excited and we have two zeros located in the middle of the top and bottom arms, and two poles located in the middle of the left and right arms of the square ring. If the excitation port is changed to *port 2*, we have the T_{010}^z mode and the field configuration is rotated by 90° (Hong, 1995). By adding a square patch as a perturbation at $\phi = 45^\circ$ these two degenerate modes are coupled and a dual-mode resonator can be obtained (Hong, 1995 and Curtis, 1991). The dimension of the square patch controls the coupling between the two degenerate modes (Chen, 2008).

The dimension of square patch perturbation is set to $d = 1.2$ mm to obtain optimal results. The feed line widths W_1 and W_2 are fixed to 0.2 mm and 0.576 mm respectively, to achieve acceptable insertion loss and matched to 50Ω line connectors. The feedlines length is $L_f = 14$ mm, and the gap size is $G = 0.1$ mm. The structure in Figure 3 is simulated using EM simulator software (EM, 2006) and the results are shown in Figure 4.

The simulation results exhibit that the specifications for narrowband filter at WiMax frequency is obtained. The minimum insertion loss is 1.5 dB and the return loss better than -25 dB. The fractional bandwidth is about 5.1%. The two transmission zeros are located at 2.1GHz, and 2.62GHz, having a sharp rejection of more than 40 dB.

4.1 Extracting External Quality Factor, Q_e

The external quality factors can be extracted by using EM simulator software (EM, 2006). This method of extracting external quality factor is illustrated in Figure 5, where the single-mode resonator is set as weakly coupled to its feed at one side. The dimensions of the resonator shown in Figure 2(a) are $a = 12.2$ mm, $W_1 = 0.2$ mm, $W_2 = W = 0.576$ mm, and $G = 0.1$ mm. By using the simulation results from the EM simulator (EM, 2006) shown in Figure 6, Q_e can be calculated by using (Hong, 2001):

$$Q_e = \frac{f_0}{BW_{3dB}} \quad (5)$$

Where f_0 is the center resonating frequency, and BW_{3dB} is the 3dB bandwidth, expressed as:

$$BW_{3dB} = f_2 - f_1 \quad (6)$$

Substituting $f_1 = 2.25$ GHz and $f_2 = 2.34$ GHz in Equation (6), the 3dB bandwidth, $BW_{3dB} = 0.09$ is achieved, then by replacing it and $f_0 = 2.3$ GHz in Equation (5), the $Q_e = 25.5$ is obtained.

4.2 Extracting the Coupling Coefficient

Since a dual-mode resonator operates as two resonators, coupling coefficient exists between them. Coupling coefficient between resonators can be extracted by using the EM simulator. In this method, the resonators should be weakly coupled to their feeds on both sides as depicted in Figure 7. The coupling coefficient is calculated using the simulation result shown in Figure 8 and the general formulation for extracting the coupling coefficient, k_{12} between the first and the second modes is expressed by Equation (7) (Hong, 2001):

$$k_{12} = \frac{f_2^2 - f_1^2}{f_2^2 + f_1^2} \quad (7)$$

Where f_1 and f_2 are the resonant frequencies of mode 1 and mode 2, respectively as illustrated in Figure 8.

For optimal design, with $d = 1.2$ mm, two degenerate modes frequencies obtained are shown in Figure 8. Substituting $f_1 = 2.27$ GHz, and $f_2 = 2.36$ GHz, in Equation (7), the coupling coefficient in this design is obtained $k_{12} = 0.0388$. Since the modes frequencies change by perturbation size therefore, the coupling coefficient is a function of the perturbation size (d). The variation of coupling coefficient, k_{12} versus perturbation size, d is demonstrated in Figure 9.

5. Experimental Results

The filter is fabricated using standard photolithography process on R/T Duroid 6010 having relative permittivity, $\epsilon_r = 10.2$, 0.636 mm of substrate thickness, and substrate loss of $\tan \delta = 0.0023$. Figure 10 shows the photograph of the BPF and its dimensions with respect to Figure 3 are shown in Table 1. As shown in Figure 10, two 50Ω SMA connectors are joined to 50Ω feedlines to connect to the Vector Network Analyzer (VNA) for measurement in the best matching condition. The measurement was performed using an HP8510B Vector Network Analyzer.

Figure 11 shows that the simulated and measured results are in good agreement. The fractional bandwidth is about 5.1%, the return loss is better than -20 dB and the minimum insertion loss of the filter is 1.68 dB. Conductor loss, and connector mismatches are the main factors to contribute to the total loss. By using superconductors and designing with

very narrow gap feedlines, using micromachining technique can reduce the insertion loss to its minimum, but it should be mentioned that the size of the coupling gaps between the feedlines and ring resonator affects not only the strength of coupling but also the resonant frequency (Chang, 1987 and Hsieh, 2003). Furthermore, micromachining is costly and superconductors need the use of cryostats that makes the application limited and not robust. In this design, some simple techniques are used to improve the filter performance. One of them is using proper substrate material with high dielectric constant and low loss tangent. This leads to having more compact size and lower insertion loss in passband. It is also possible to increase the system performance by using good feed line structure including proper feed line gap, width and length. Another simple technique used here in this filter design is the 45° mitered bend that helps to have less insertion loss and better return loss with simpler and cost effective fabrication, compared to similar designs reported in (Hong, 1995, Chen. C. H., 2007 and Hsieh, 2000). A research in (Razalli, 2008), presents four types of bending (discontinuity), and shows that 45° mitered bend technique gives the lowest insertion loss and the best return loss in passband.

6. Conclusions

A compact narrowband bandpass filter using dual-mode microstrip square loop resonator is designed and tested. The simulated and measured results are in good agreement. The dual-mode was excited by adding a square patch to the resonator, and a narrowband bandpass filter was introduced. In this design, the minimum measured insertion loss is 1.68 dB and the return loss better than -20 dB operating at 2.3GHz with a fractional bandwidth of 5.1% with two transmission zeros on both sides of the passband. It is fabricated on Duroid 6010 substrate having a relative dielectric constant of 10.2 and 0.635 mm of thickness. By applying proper substrate material, feedlines gap, length and width, as well as 45° mitered bend; the filter performance has been enhanced. This filter is attractive for further development and hence, it could be applied to support modern wireless communications and WiMax applications as it offers compactness in size with good performance and sharp rejection.

References

- Chang, K. (2004). *Microwave Ring Circuits and Related Structures*, New York: John Wiley & Sons.
- Chang. K., Martin. T. S., Wang. F., and Klein. J. L. (1987). On the Study of Microstrip Ring and Varactor-Tuned Circuits. *IEEE Transactions on Microwave Theory and Techniques*, Vol. 35, 1288-1295.
- Chen. C. H., Lin. Y. F., and Chen. H. M. (2007). Miniaturized Dual-Mode Bandpass Filter Using Mender Square Ring Resonator. *IEEE Conference on Electronic Devices and Solid State Circuits*, 777-780.
- Chen. Z. X., Dai. X. W., and Liang. C. H. (2007). Novel Dual-Mode Dual-Band Bandpass Filter Using Double Square-Loop Structure. *Progress In Electromagnetics Research*, PIER 77, 409-416.
- Curtis. J. A., and Fiedziuszko. S. J. (1991). Miniature dual mode microstrip filters. *IEEE MTT-S Digest*, Vol. 2, 443-446.
- El-Shaarawy. H. B., Coccetti. F., Plana. R., El Said. M., Hashish. E. A. (2008). Compact Bandpass Ring Resonator Filter with Enhanced Wide-Band Rejection Characteristics Using Defected Ground Structures. *IEEE Microwave and Wireless Components Letters*, Vol. 18, 500-502.
- EM. User's Manual, Computer Simulation Technology (CST) Microwave Studio, Version 2006B.
- Hong. J. S., Lancaster. M. J. (1995). Bandpass Characteristics of New Dual-Mode Microstrip Square Loop Resonators. *Electronics Letters*, Vol. 31, No. 11, 891-892.
- Hong, J. S., and Lancaster, M. J. (2001). *Microstrip Filters for RF/Microwave Applications*, New York: John Wiley & Sons.
- Hsieh. L. H., Chang. K. (2003). Compact, Low Insertion-Loss, Sharp-Rejection, and Wide-Band Microstrip Bandpass Filters. *IEEE Transactions on Microwave Theory and Techniques*, Vol. 51, No. 4, 1241-1246.
- Hsieh. L. H., Chang. K. (2000). Compact Dual-Mode Elliptic-Function Bandpass Filter Using a Single Ring Resonator with One Coupling Gap. *Electronic Letters*, No. 19, Vol. 36, 1626-1627.
- Pozar, D. M. (2005). *Microwave Engineering*, New Jersey: John Wiley & Sons.
- Razalli. M. S., Ismail. A., Mahdi. M. A., and Hamidon. M. N. (2008). Novel Compact Microstrip Ultra-Wideband Filter Utilizing Short-Circuited Stubs With Less Vias. *Progress In Electromagnetics Research*, PIER 88, 91-104.
- Wolff. I. and Knoppik. N. (1971). Microstrip Resonator and Dispersion Measurements on Microstrip Lines. *Electronics Letters*, Vol. 7, 779-781.

Table 1. Dimensions of “dual-mode filter”, with reference to the layout depicted in Figure 3

Parameter	Dimension (mm)
Perturbation size, d	1.2
Feedlines length, L_f	14
Feedgaps size, G	0.1
Feedlines width, W_1	0.2
Feedlines width, W_2	0.576
Resonator width, W	0.576
Side length of square resonator, a	12.2

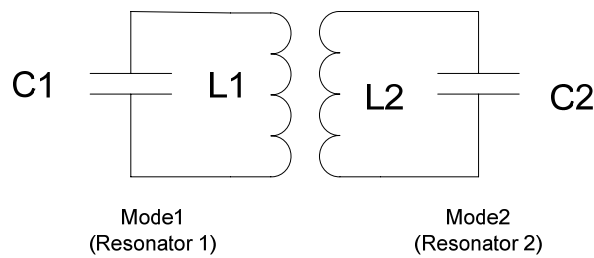


Figure 1. Lumped element equivalent circuit of a dual-mode resonator

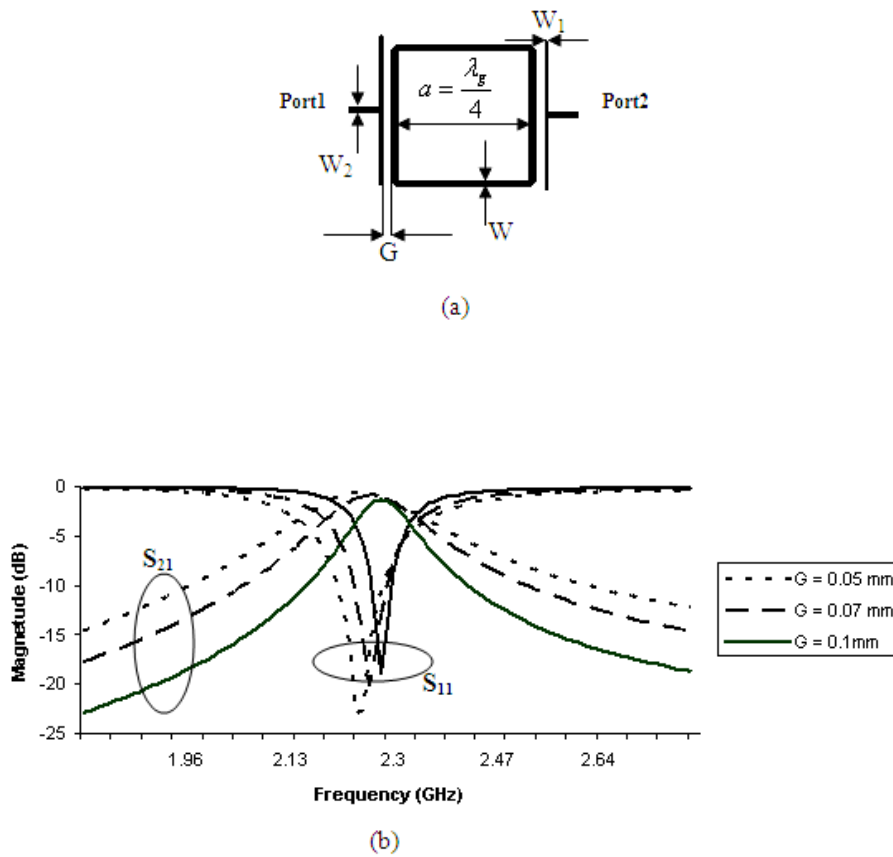


Figure 2. (a) Single mode square ring resonator, (b) simulation results (insertion loss, S_{21} and return loss, S_{11}) of a single mode resonator for different values of G .

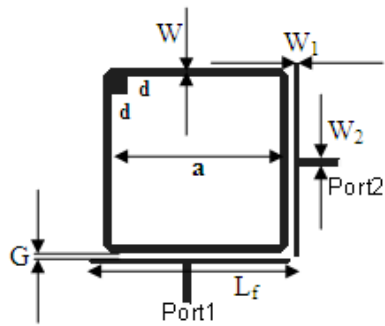


Figure 3. Dual-mode bandpass filter

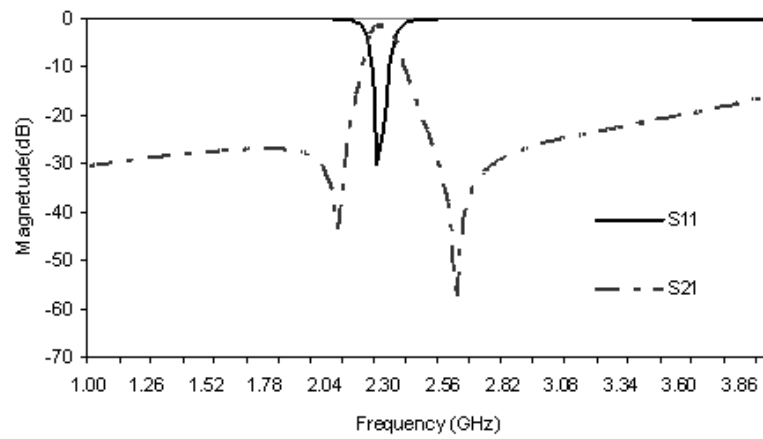


Figure 4. The simulation results for dual-mode filter

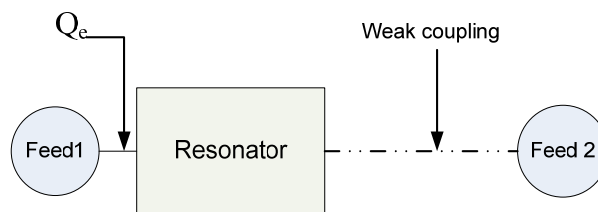


Figure 5. Extracting Q_e using EM simulator

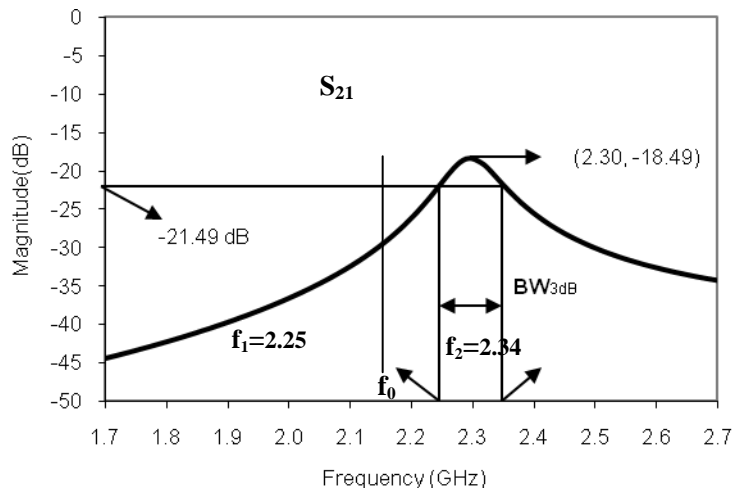


Figure 6. Simulated S_{21} for calculating Q_e .

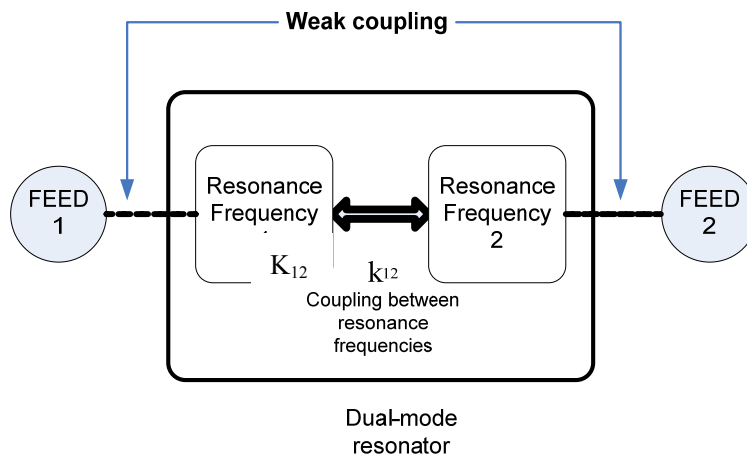


Figure 7. Extraction of coupling coefficient between resonators using an EM simulator

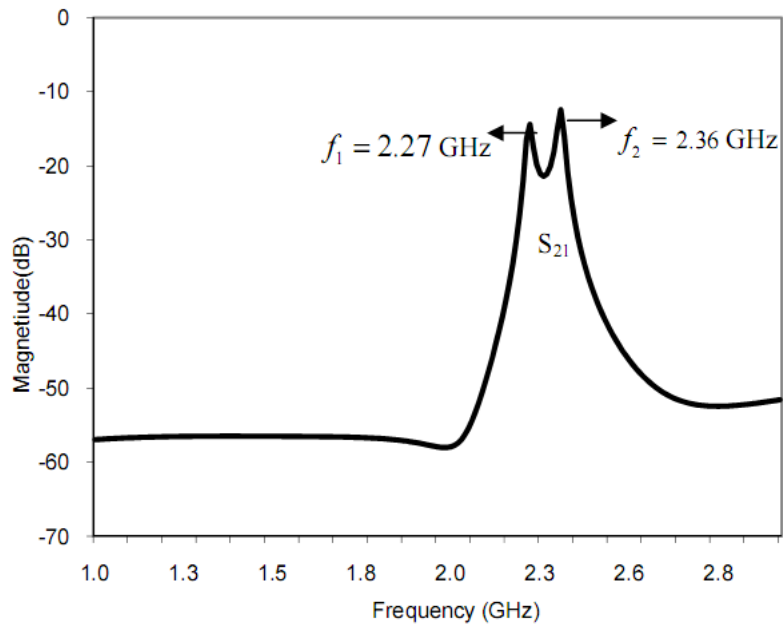


Figure 8. Simulated S_{21} for calculating coupling coefficient

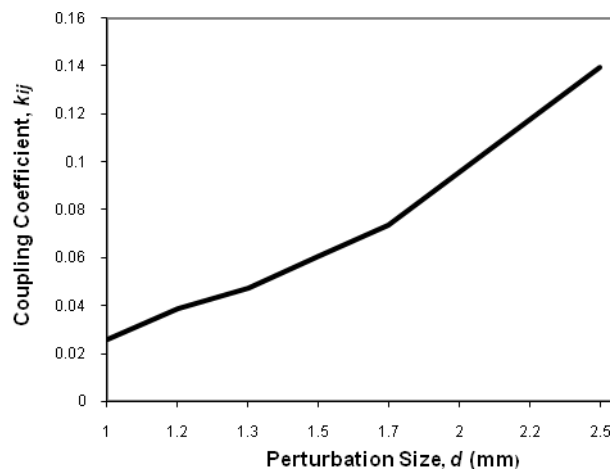


Figure 9. Variation of coupling coefficient, k_{ij} with perturbation size, d .

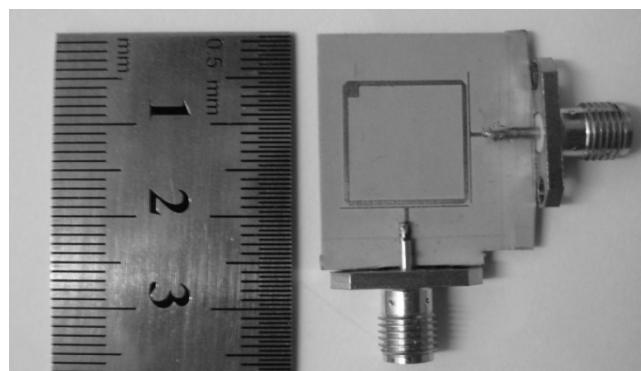
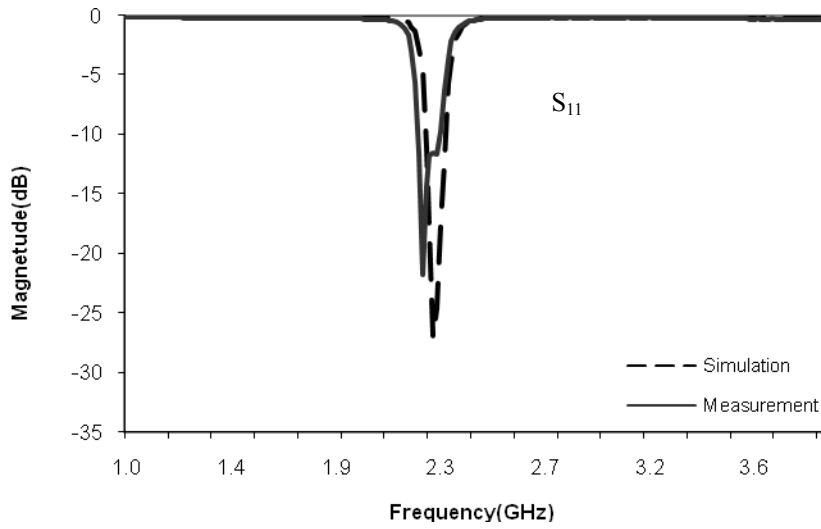
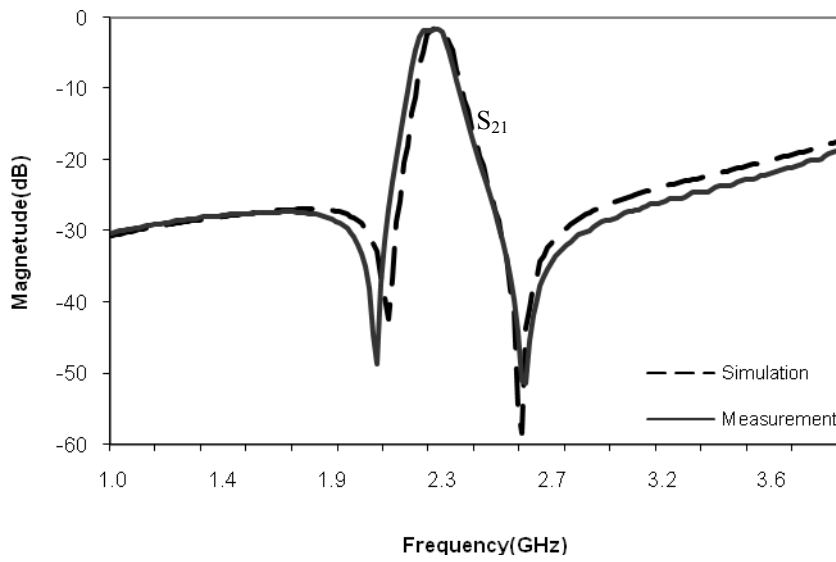


Figure 10. The photograph of the BPF



(a)



(b)

Figure 11. Measured and simulated results for the dual-mode filter
 (a) Return loss, S_{11} (b) Insertion loss, S_{21} .



The Implement of MPEG-4 Video Encoding Based on NiosII Embedded Platform

Fugang Duan

School of Optical-Electrical and Computer Engineering, USST

Shanghai, China

E-mail: dfgvvvdfgvvv@126.com

Zhan Shi

School of Economics, Peking University

School of Optical-Electrical and Computer Engineering, USST

E-mail: haolin@public2.sta.net.cn

Abstract

Using software code to achieve video coding, reduce the cost and increase portability, present a scheme using Altera SOPC to control data coding for MPEG-4 video software compressing system. According to use the DE2 board of Altera, implementing coding image data's input and output through the USB port on the board, achieves the input image MPEG-4 encoding using the configural NiosII embedded soft processor. Aiming at MPEG-4 video compression, the design adopts dynamic sprite encode to code the image data efficiently.

Keywords: MPEG-4, Sprite encode, SOPC NiosII, Embedded processor

1. Introduction

MPEG-4 ISO was formally announced in 1999 as an international standard by the Moving Picture Experts Group (ISO/IEC 14496, 1999). MPEG-4 and MPEG-1 and MPEG-2 are very different, and its compression ratio is greater, and it is the target encoding. MPEG-4 not only has a body compression algorithm, it is an international standards of integration and the demand for compression technology such as a digital television, interactive graphics applications (synthetic audio-visual content), interactive multimedia (WWW, information intake and decentralized). It can meet the needs of the three ethnic groups - multi-media content creators, network service providers and end-consumers. In addition to the traditional MPEG-4 encoding and decoding of digital video features, it has a lot of compelling features, including object-based video content object access to the scene content-based scalability, video depository check, error correction capability. MPEG-4 compression standard can be achieved between the compressed frame. The average compression ratio up to 50:1 or even higher up to 100:1, a relatively high compression ratio, and have a unified format, a good compatibility (John Viega, 2002).

Systems using Altera's DE2 development board, using SOPC configurable soft-core embedded processor NiosII realizes MPEG-4 video standard. Through the hardware design and software programming will be a large number of control and access to a wide range of peripherals to a rational allocation of work to meet the timing and functional requirements. On this basis the compiler run the MPEG-4 video encoding process to encode QCIF video file. The implement of MPEG-4 Video encoding apply to the user's specific requirements and the reduction of the actual situation, which has flexibility, taking up less resources, the use of a wide range of highly specialized nature.

2. System structure and working principle

Systems encode streaming media file which can be CIF and QCIF format. System can be divided into two parts such as hardware and software and take full advantage of the advantages of NiosII processor.

Hardware realization of some of the major functions: system design is achieved by the FPGA-based Nios II, which is constituted mainly by operation, control, input and output interfaces and peripherals. (1) Operation part use NiosII 32-bit RISC embedded system design for the system clock frequency 50MHz. (2) Control in part is constituted by the real-time control and status display. (3) Input-output interface is achieved by the USB interface based ISP1362

controller. The use of the main mode, read from the USB peripheral processor to carry out cross-source codec, and the output file is transmitted by the USB to peripheral for preservation. (4) Peripherals can be extended, for example, U disk, PC camera, video player and so on. Select the specific application according to the practice.

Software realization of some of the major functions: Using the C language to realize MPEG-4 video coding. Read code files (format YUV4: 2:0) directly from the FLASH, for each frame image of the Sprite has been the overall image motion estimation and motion compensation, the encoding of the data after a deposit to the SDRAM. After encoding the holistic files, encoding the data to write FLASH one-time from SDRAM. In the system, encoding each frame takes about 0.481s. By test, if the algorithm running on the clock frequency of 2.8GHz Pentium 4 processor, time for each frame encoding is 7.48ms, and the rate can be as high as 133.69pfs.

3. Hardware design

Using SOPC Builder system development tool to create 32-bit Nios CPU, and using automated Avalon switch fabric to form the total line to connect the system together with peripheral equipment. Hardware acceleration units and commands of the definition of the word constitute a powerful 32-bit embedded processor system (as shown in Figure 1).

USB on DE2 board Philips use ISP1362 controller chip, which is the composition of an OTG controller, a host controller and a peripheral controller. They connected with each other through a data bus interface and an external processor. The chip of ISP1362 integrate OTG transceiver, a charge VBUS actuators, as well as pull and pull-down resistors, which is used to reduce the number of external components for reducing costs.

SOPC Builder configuration shown in Figure 2.

4. Software Design

4.1 MPEG-4 encoding

At present, MPEG-4 standard-based application programs are for the most hardware, but the use of a dedicated MPEG-4 encoder chip is difficult to achieve the upgrading and because of the high cost, poor flexibility. In the system, using software to achieve the MPEG-4 video coding. First of all, the video encoder to set encoding parameters, such as the VOP size, frame rate, coding format, coding parameters such as scan mode. And then read from the FLASH file data stream QCIF to encode based on the set of encoding parameters. And then writing encoded data streams based on the appropriate file format (MP4U) into the SDRAM memory. Aim at the MPEG-4 video encoding in several key areas described as follows:

1) Definition of VOP generation.

MPEG-4 encoding unit is the VOP, VOP generation is achieved through the video segmentation, video segmentation is to achieve object-based video coding system. Image segmentation technique based on the use of segmentation information, is divided into partitions based on the texture segmentation, motion-based segmentation and space-time segmentation. Coding based on the requirements for image segmentation is not very high, mainly due to the real-time, where a selection of the joint space-time automatic video object segmentation algorithm. The first time-domain algorithm based on the F-partition hypothesis testing approach to be the initial change detection template, and then through the morphology-based segmentation of the airspace to get the ultimate fusion of moving objects. This relatively simple algorithm that can better the prospects of moving objects will be separated from the background.

2) Dynamic sprite coding.

Sprite coding is a new generation of coding technology, which generated global motion estimation using video images Sprite background paragraph, and then code the Sprite image, the context of the subsequent frames are encoded relative to the frame of the motion parameters Sprite image coding. Based on the background of the smooth and texture characteristics of a great relevance for Sprite coding panorama use a direct space prediction method.

Dynamic Sprite coding as shown in Figure 3. Video sequence of the first frame use I-VOP encoding method, and the first frame of the reconstructed image in the encoding and decoding client side to establish the same initial Sprite image. The second frame use the overall motion estimation algorithm to estimate a global campaign between the current VOP with the former VOP. Using the reference point describe the movement between the two VOP. Method using P-VOP texture code the second frame which is different with the first frame in all the VOP macroblock such as the motion compensation mode in addition to the macroblock and block motion compensation, but also can be used as a reference for Sprite image motion compensation, when the macro motion compensation block for the global motion compensation. Decoder decoding the track to be the reference point for global motion parameters, and then decoding texture information is the second frame of the reconstructed image, according to global motion parameters and the second frame image reconstruction image update Sprite. The same method used for coding sequence behind the VOP.

4.2 USB host software process

The flow chart of the USB host software 4 below, the major software part including USB host and USB peripheral

function modules. They can be independent of each other while calling each other to jointly complete the USB host function. The entire process to complete disruption through scheduling to achieve the host function. When USB bus is in the work, the system is still in accordance with the specific running timing and protocol specification. If the system online through changed level in the data bus to detect USB devices connect in or out, and then host and peripherals on the basis of prior agreement of the order implement a series of information exchange.

To identify the host if it is a USB device must pass enumeration process, host use bus enumeration to identify and manage the necessary changes in equipment status. Bus enumeration process is as follows: (1) Equipment connect. USB device access to USB.

(2) Equipment power up. USB devices can use the USB bus-powered or an external power supply.

(3) Detected the host equipment reset signal. Equipment power up, the host device through the pull-up resistor to detect if a new device connects to the host port and sends a reset signal.

(4) Equipment by default. Equipment from bus to receive a reset signal, but can't go on a bus in response to handling. Equipment reset signal is received, use the default address to addressing them.

(5) Address assignment. When the host device to receive the address of the default (00H) response time, distribution of equipment on a free address, equipment only can be response to the address.

(6) USB host read device descriptor to verify the properties of equipment.

(7) Device configuration. USB host device read the device descriptor to configure parameter, if the resources needed to meet the USB, transmit configuration commands to the USB device that means the end configuration.

(8) Hang. In order to save power, when the bus remain idle for more than 3ms, the device driver will enter the suspend state.

5. System Testing

In order to verify if the results of this coding is correct, we run the code on the PC-environment of VC++6.0 compiler to emulator running the same encoded video files, as well as the results will be decoded in VC++6.0. YUVViewer to show through the images before and after encoding: Figure 5 is the 13th frame image before encoding, Figure 6 is the frame image after decoding.

Comparison shows that MPEG-4 coding distortion is very small, NiosII now in order to verify the code is correct, as long as to compare the two results of each frame that are encoded on NiosII and VC++6.0. After encoding each frame comparison from the number of bytes. By the experimental comparison, their results are the same encoding. Finally, in the end the output encoding file on NiosII is decoded on PC, the results obtained in Figure 6. This can confirm that the coding in NiosII is entirely correct. Verify the file size before and after encoding, as shown in table 1.

Compression ratio mainly is relative to frame relevance in image, not the size of image files. According to statistics, it is available to get the average compression ratio of MPEG-4 that is the 50:1, higher to achieve more than 100:1.

6. Concluding remarks

Has been introduced an international compression standard MPEG-4 and a software code realization based on NiosII. Through the use of Altera's 32-bit embedded processor NiosII to develop software on QuartusII 5.1 IDE for the design of system. After experimental verification, embedded video coding system based on NiosII has the implementation of highly efficient compression and can achieve real-time requirements. System can be applied to monitor field, according the front terminal using USB camera without capture card, not only cost savings, but also be high stability, so the system has great value.

References

Altera Corp. (2005). Avalon Interface Specification. [Online] Available: http://www.altera.com/literature/manual/mnl_avalon_spec.pdf (May 1, 2009)

Altera Corp. (2005). NiosII Software developer's Handbook. [Online] Available: <http://www.altera.com.cn/literature/lit-nio2.jsp> (May 3, 2009)

Brown JS. (1992) *The application of code instrumentation technology in the Los Alamos debugger*. New Mexico :Alamos National Laboratory, (Chapter 1~4).

Creeg2. (2009). FPGA Configuration with JTAG. [Online] Available: <http://www.alteraforum.com/forum/showthread.php?t=4533> (May 7, 2009)

ISO/IEC 14496. (1999). INFORMATION TECHNOLOG--CODING OF AUDIO VISUAL OBJECTS-Part2: Visual. ISO/IEC 14496.

John Viega. (2002). A static Vulner-ability Scanner for C and C++ Code. *Reliable Software Technologies*. ITS4.

Latha Pillai. (2005). Color Space Converter:Y'CrCb to R'G'B'. *XAPP283*. 24 March 2005.

Seongmo Park, et. (2002). A Single-Chip Video/Audio Codec for low Bit Rate Application. *ETRI Journal*. pp.20-29.

Table 1. The test table of MPEG-4 compressing rate

Before encoding file Size (MB)	After encoding file Size (KB)	Compression ratio
0.958	15.63	61.3
3.486	53.49	64.8
10.8	116	93.1
72.5	1050	69.05
72.5	1620	44.75
76.1	335	227.2

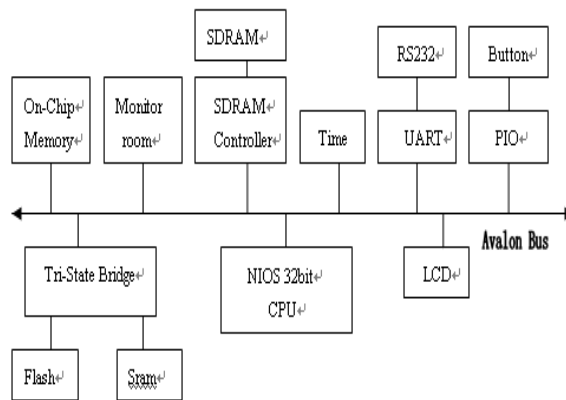


Figure 1. Main composing of system

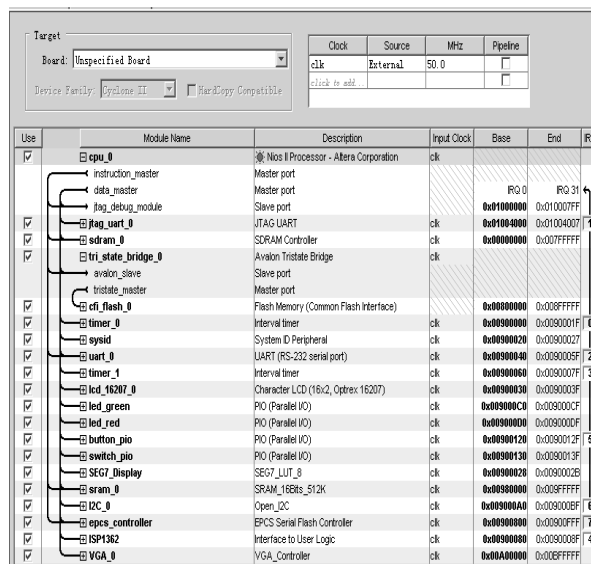


Figure 2. SOPC Builder configuration

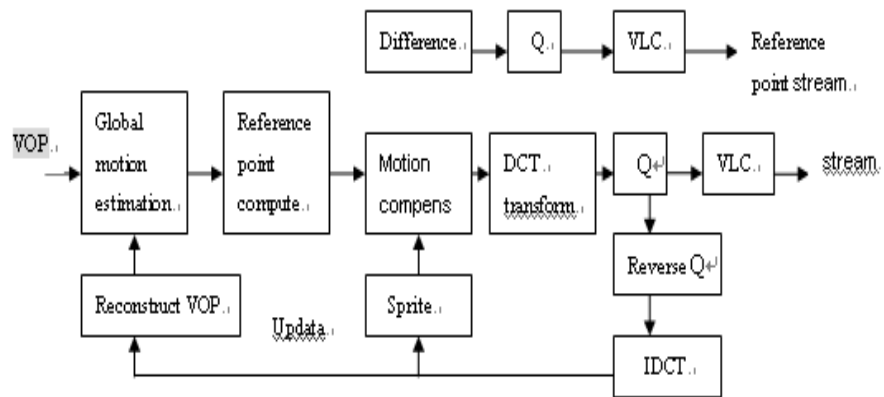


Figure 3. The chart of dynamic Sprite encode

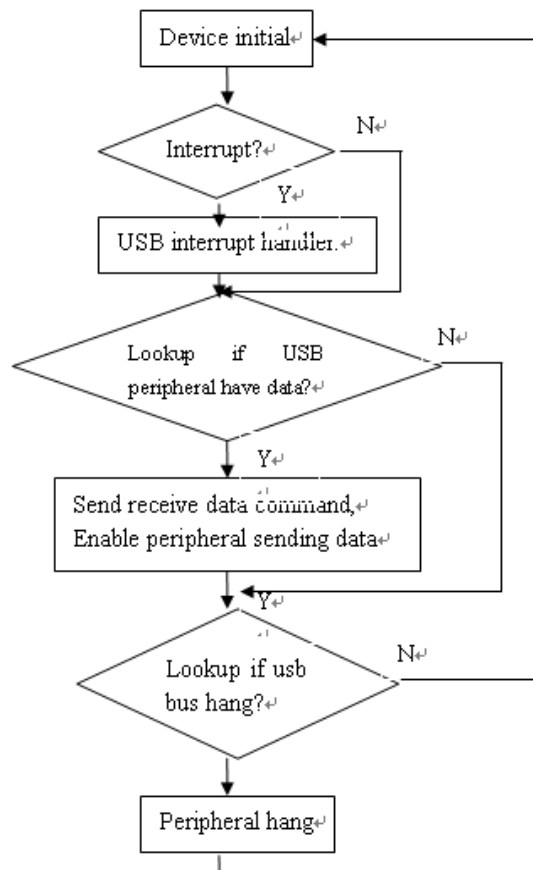


Figure 4. The flow chart of USB host software



Figure 5. Before encoding



Figure 6. After decoding



Optimal Design of Capacitive Micro Cantilever Beam Accelerometer

Othman Sidek

Collaborative Microelectronic Design Excellence Centre
Universiti Sains Malaysia, Engineering Campus, 14300 Nibong Tebal
Sri Ampangan, Pulau Pinang, Malaysia
Tel: 60-3-599-5800 E-mail: othman@cedec.usm.my

Muhamad Azman Miskam

Collaborative Microelectronic Design Excellence Centre
Universiti Sains Malaysia, Engineering Campus, 14300 Nibong Tebal
Sri Ampangan, Pulau Pinang, Malaysia
Tel: 60-3-599-5856 E-mail: azman@cedec.usm.my

H.M.T. Khaleed

School of Mechanical Engineering
Universiti Sains Malaysia, Engineering Campus, 14300 Nibong Tebal
Sri Ampangan, Pulau Pinang, Malaysia
Tel: 60-3-599-6369 E-mail: khalid_tan@yahoo.com

Mohd Fauzi Alias

Collaborative Microelectronic Design Excellence Centre
Universiti Sains Malaysia, Engineering Campus, 14300 Nibong Tebal
Sri Ampangan, Pulau Pinang, Malaysia
Tel: 60-3-599-5856 E-mail: fauzi@cedec.usm.my

Shukri Korakkottil Kunhi Mohd

Collaborative Microelectronic Design Excellence Centre
Universiti Sains Malaysia, Engineering Campus, 14300 Nibong Tebal
Sri Ampangan, Pulau Pinang, Malaysia
Tel: 60-3-599-5962 E-mail: shukri@cedec.usm.my

Abstract

This study presents the behavior of a micro cantilever beam accelerometer under electrostatic actuation by using the analytical and numerical method. The objective of this study is to determine optimal design of capacitive micro cantilever beam accelerometer in term of reducing the beam deflection with respect to applied acceleration but keeping the distance between electrodes. The structure contains proof mass which is suspended between fixed rigid electrodes to provide differential capacitance measurements. ANSYS[®] is used for finite element analysis (FEA) modeling and simulation. The analytical modeling is done by using C programming. Three dimensional modeling is done for six different loading conditions in order to come out with the optimal design. The results obtained from both the analytical and finite element models are found to be in excellent agreement.

Keywords: Microelectromechanical system, Microaccelerometer, Inertial sensors, Micromachined sensors, Silicon sensors

1. Introduction

Recent scientific and technological advances in micro technologies have produced an increasing interest in the application of micromechanical freestanding structures (cantilevers, bridges and diaphragms) in many fields where advance performance, high sensitivity and reduce dimensions are required (Bianco et al., 2008). Cantilever beams are widely used as the basic components in micro-sensors, micro-switches and RF-MEMS as well as in experimental micromechanics for evaluating mechanical properties and the strength of materials (Ballestra et al., 2008).

Sensors and actuators are the two main categories of the microelectromechanical system (MEMS). A sensor is a device that measures information from a surrounding environment and provides an electrical output signal in response to the parameter it measures. An actuator is a device that converts an electrical signal into an action. It can create a force to manipulate itself, other mechanical devices or the surrounding environment to perform some useful function. A variety of different basic principles are used to implement MEMS actuators including electrostatic, piezoelectric, magnetic, magnetostrictive, bimetallic and shape-memory alloy. MEMS accelerometers can be fabricated by using bulk micromachining or surface micromachining. (Fricke and Obermier, 1993). The technology of MEMS enables the fabrication of tiny, mechanical structures from silicon wafers offering three characteristic features of technology, miniaturization multiplicity and microelectronics.

A MEMS capacitive-type sensor is basically an electrostatic transducer that depends on electrical energy in terms of constant voltage (voltage drive) or constant charge storage (current drive) to facilitate the monitoring of capacitance change due to an external mechanical excitation such as force, acoustical pressure or acceleration. Capacitive micro accelerometers have the combined advantages of high sensitivity, good dc response and noise performance, low-drift, low-temperature sensitivity and low-power dissipation. In many of the capacitive sensing accelerometers, the acceleration force (in terms of g) deflects the proof mass. Micro fabricated cantilever beams are widely used in MEMS capacitive-type sensors as the sensing element (Chowdhury et al., 2005). Vivek et al. (2006) proposed a design methodology for a micro machined single axis silicon capacitive accelerometer. This methodology will be able to reduce time and cost. Coventorware software is used to simulate finite element analysis and the Particle Swarm Optimization (PSO) technique is used as a tool for dimensions optimization. The limitation of the design is the die size i.e. minimum beam thickness is fixed at 40 μm and the thickness of the proof mass is fixed at 575 μm . Five different structures were analyzed and it was observed that to square the square proof mass with eight Beam Bridges was the optimal solution. Heng Yang et al. (2005) studied the design, fabrication and initial measurement of a cantilever beam pull-in accelerometer. They carried out analytical modeling and found that sensitivity and nonlinearity decreased with the increase of the driving torque and increased with the increase of the damping.

Substantial efforts have been made by many researchers to know the exact behavior of the cantilever beam when it has been subjected to force. Puersy and Reyntjensz (1998) characterized a miniature silicon micromachined capacitive accelerometer with a size of 500 x 500 μm^2 and fabricated using bulk micromachined technology. They found from static measurements that the measured sensitivity (z-direction) of the device is less than the expected value and the asymmetric suspension system causes considerable deviations from the ideal behavior. Thus, it is very important to know the deflection of the cantilever beam and to optimize the design of the beam-mass structure to achieve the required deformation. The necessity to compute the deflection of the cantilever and the freely suspended mass is to know the effect of deflection on the electrode which has been placed at the air gap. In the present study, a capacitive micro cantilever beam is simulated according to device dimensions taken from the literature. ANSYS software is used to simulate the model FEM and C programming is used to analytically determine the displacement of the proof mass according to different accelerations.

2. Methods

2.1 Mathematical modeling

The simplified model for the basic mechanical properties of the beam-mass structure is shown in Figure 1. In this model, the beam and the mass are considered to have a rectangular cross section. The length, thickness and width of the beam are a_1 , h_1 and b_1 respectively. The thickness and the width of the mass are h_2 and b_2 respectively. The length of the mass is $a_2 - a_1$. If the mass center is located at $x=L$ in the coordinate system,

$$L = \frac{1}{2}(a_1 + a_2) \quad (1)$$

The differential change of the capacitance due to the deflection of the proof mass can be used to estimate the sensitivity, resolution and non-linearity of the sensor. The deflection of the beams and the proof mass can be estimated by double integration or by the successive integration method. The dynamic behavior is analyzed by determining the natural frequency and the damping force. Assuming that the mass of the beam is negligible hence the proof mass is rigid i.e.

no bending takes place. Assuming the accelerometer is under acceleration, a , in the z -direction, the stress and displacement are caused by the acceleration.

2.1.1 Stress Analysis

The differential equation for region 1 (the beam region, in $0 < x < a_1$) is:

$$-EI_1 w_1''(x) = -m_o + F_o x \quad (2)$$

Where $I = \frac{1}{12} b_1 h_1^3$, $F_o = ma$ and $m = 2(L - a_1)h_2 b_2 \rho$. The differential equation for region 2 (the mass region in $a_1 < x < a_2$) is

$$-EI_2 w_2''(x) = -m_o + F_o x - \frac{I}{2} (x - a_1)^2 b_2 h_2 \rho a \quad (3)$$

When $w_1''(a_2) = 0$;

$$m_o = maL = F_o L \quad (4)$$

By substituting equation (4) into equation (1);

$$w_1''(x) = \frac{12(L-x)ma}{Eb_1 h_1^3} \quad (5)$$

The stress on the surface of the cantilever beam $\left(z = -\frac{h_1}{2}\right)$ is:

$$T_c(x) = \frac{6ma(L-x)}{b_1 h_1^2} \quad (6)$$

The maximum stress on the beam is at $x=0$ and the value is:

$$T_{c\max} = T_c(0) = \frac{6maL}{b_1 h_1^2} \quad (7)$$

2.1.2 Displacement

According to Equation (5), ($w_1(0) = w_1'(0) = (0)$), the slope of the beam is:

$$w_1'(x) = \frac{6ma(2L-x)x}{Eb_1 h_1^3} \quad (8)$$

The displacement of the beam is:

$$w_1(x) = \frac{2ma(3L-x)x^2}{Eb_1 h_1^3} \quad (9)$$

The maximum displacement of the beam is at $x=a_1$ and the value is:

$$w_1(a_1) = \frac{2ma(3L-a)a_1^2}{Eb_1 h_1^3} \quad (10)$$

The slope at that point is:

$$w_1'(a_1) = \frac{6ma(2L-a_1)a_1}{Eb_1 h_1^3} \quad (11)$$

As the mass is much thicker than the beam, the deflection of the mass is negligible. Therefore, the displacement in region 2 can be approximated by:

$$w_2(x) = w_1(a_1) + w_1'(a_1)(x - a_1) \quad (12)$$

According to Equations 10, 11 and 12, the displacement of the mass is:

$$w_2(x) = \frac{2ma}{Eb_1 h_1^3} [3(2L - a_1)x - (3L - 2a_1)a_1] a_1 \quad (13)$$

The displacement at the mass center ($x=L$) is found to be:

$$w_2(L) = \frac{4ma}{Eb_1 h_1^3} (3L^2 - 3La_1 + a_1^2) a_1 \quad (14)$$

The maximum displacement is at the far end of the mass ($x=a_2=2L-a_1$) and can be expressed as:

$$w_{\max} = \frac{2ma}{Eb_1 h_1^3} (12L^2 - 15La_1 + 5a_1^2) a_1 \quad (15)$$

The analytical simulation is done by using C programming and the system interface is shown in Figure 2.

2.2 Finite element analysis

The design models are modeled in ANSYS and divided into the required number of segments in order to obtain element continuity. The 2D model is meshed with 2D (quadrilateral) solid ELEMENT 42 and the same elements are extruded to 3D (hexahedra) solid ELEMENT 45. The beam is fixed at the left surface, the all degree of freedom have been constrained. and load has been applied at the middle node upper surface of rear end of the mass. The simulation assumes that the deflection of the electrodes is not considered and the mass is thicker than the beam hence the deflection of the mass is negligible.

PLANE42 is used for the 2-D modeling of solid structures (Figure 3). The element can be used either as a plane element (plane stress or plane strain) or as an axisymmetric element. The element is defined by four nodes having two degrees of freedom at each node: translations in the nodal x and y directions. The element has plasticity, creep, swelling, stress stiffening, large deflection, and large strain capabilities. The geometry, node locations, and the coordinate system for this element are shown in Figure 4. The element input data includes four nodes, a thickness (for the plane stress option only) and the orthotropic material properties. Orthotropic material directions correspond to the element coordinate directions. Pressures may be input as surface loads on the element faces as shown by the circled numbers in Figure 2. Positive pressures act into the element. Temperatures may be input as element body loads at the nodes.

PLANE45 is used for the 3-D modeling of solid structure, element PLANE45 is defined by eight node element and each element node is having three degree of freedom ,translation in $x,y,$ and z direction .The 3-D structure solid is of three types, hexahedron, tetrahedral and prism, in this study hexahedron elements have been selected for meshing. the critical regions have been meshed with fine and map mesh(structured mesh) to achieve accurate results.

3. Results and Discussion

The parameters used are shown in Table 1. To study the behavior of the device, the dimension of the device is varied according to previous research (Vivek et al., 2006; Lohit and Shiva, 2008; Heng Yang et al., 2005). The design is limited to a single beam cantilever structure and square proof mass. A comparative study is made for the analytical and FEM results of three models with different beam dimensions. The maximum displacement for the first model is shown in Figure 5 while Figures 6 to 11 show the deflection contours. The maximum displacement for the second model is shown in Figure 12 while Figures 13 to 18 show the deflection contours. The maximum displacement for the third model is shown in Figure 19 while Figures 20 to 22 show the deflection contours.

The maximum displacement linearly changed with the increase of acceleration for the first and second models but for the third model, the maximum displacement increased with the increase of acceleration up to $2g$ and then it decreased. Thus, the third model showed a low scale range than the other models. The second model displaced more than the first model with the same acceleration. Furthermore, the displacement of the second model exceeded the maximum distance between the electrodes, d_0 , up to $5g$. The same pattern was showed by the third model - the displacement exceeded the maximum distance between electrodes, d_0 , up to $1g$. Thus the first model showed better performance compared to the other models. In addition, it achieved a scale range of more than $6g$ because the displacement exceeded only at about $4.5\mu\text{m}$ for $6g$ acceleration but the distance between the electrodes, d_0 , was $19\mu\text{m}$.

4. Conclusions

The study on the design and the analysis of the capacitive micro cantilever beam accelerometer focusing on the deflection behavior is presented in the current paper. A comparative study is made between the analytical and FEM results according to the dimensions taken from the literature. ANSYS software is used to model, simulate and carry out FEM analysis. An analytical model is also simulated using C programming and the results obtained by FEM are in close agreement with the analytical results. The future scope for this work is performance analysis using system-level simulation techniques.

Acknowledgement

The authors would like to express sincere appreciation for the assistance of Mr. Mohd Kusairay Musa and Mr. Faisal Mohamad for their co-operation and assistance in providing support for the software. To Mr. Fazlan, Mr. Sanusi, Mr. Zamri and Puan Rohana, thanks for your kind help. Financial support from the Universiti Sains Malaysia Short Term Grant, 3004/PELECT/6035301 is gratefully acknowledged.

Nomenclature

- ρ : Specific mass
- E : Young Modulus
- b_l : Width of the beam
- a_l : Length of the beam
- h_l : Thickness of the beam

- b_2 : Width of the mass
 l : $a_2 - a_1$
 h_2 : Thickness of the mass
 a : Acceleration
 d_0 : Distance between electrodes
 F : Force

References

Ballestra, A., E. Brusa, M. Gh Munteanu, A. Soma. (2008). Experimental characterization of electrostatically actuated in-plane bending of microcantilevers. *Microsyst Technol.*, 14, 909–918.

DOI: 10.1007/s00542-008-0597-0

Bianco, S., M. Cocuzza, I. Ferrante, E. Giuri, C. F. Pirri, A. Ricci, L. Scaltrito, D. Bich, A. Merialdo, P. Schina and R. Correale. (2008). Silicon micro cantilevers with different actuation-readout schemes for absolute pressure measurement. *Journal of Physics: Conference Series*, 100, 1-4.

DOI:10.1088/1742-6596/100/9/092008

Chowdhury, S., M. Ahmadi and W.C. Miller. (2005). A closed-form model for the pull-in voltage of electrostatically actuated cantilever beams. *J. Micromech. Microeng.*, 15, 756–763.

DOI: 10.1088/0960-1317/15/4/012

Fricke, J. and E. Obermeier. (1993). Cantilever beam accelerometer based on surface micromachining technology, *J. Micromech. Microeng.*, 3, 190-192.

<http://iopscience.iop.org/0960-1317/3/4/005>

Heng Yang, Zhengyin Yu, Xinxin Li & Yuelin Wang. (2005). A Novel Pull-in Accelerometer Based on Cantilever Beam Mass Structure, *Sensors*, 2005 IEEE, 644-647.

DOI: 10.1109/ICSENS.2005.1597781

Lohit B.H. and Shiva Kumar. J. (2008). Analysis of micro capacitive accelerometer, Proceeding of International Conference on Microelectromechanical Systems (MEMS), (MEMS-08), Bhatkal India, CP16, 22-23 Oct. 2008.

Puersy, R. and S. Reyntjens. (1998). The characterization of a miniature silicon micromachined capacitive accelerometer. *J. Micromech. Microeng.*, 8, 127–133.

DOI: 10.1088/0960-1317/8/2/021

Vivek A., Tarun K. B. and Subhadeep B. (2006). Design steps for bulk micro machined single axis silicon capacitive accelerometer with optimised device dimensions, *Journal of Physics: Conference Series*, 34, 722–727.

DOI: 10.1088/1742-6596/34/1/119

Table 1. Parameters used

Geometry dimension	First model (μm)	Second model (μm)	Third model (μm)
Width of the beam, b_1	250	500	2
Length of the beam, a_1	700	500	50
Thickness of the beam, h_1	45	20	30
Width of the mass, b_2	2500	3000	20
Total length of the mass, $a_2 (l + a_1)$	3200	3500	500
Thickness of the mass, h_2	575	200	30
Distance between electrode, d_0	19	10	3
Mechanical properties			
Free space permittivity, ϵ_0	$8.8541878 \text{ E}^{-12}$	$8.8541878 \text{ E}^{-12}$	$8.8541878 \text{ E}^{-12}$
Young modulus, E	1.7 E^{11}	1.7 E^{11}	1.7 E^{11}
Specific mass of material, ρ	2230 kg/m^3	2230 kg/m^3	2230 kg/m^3

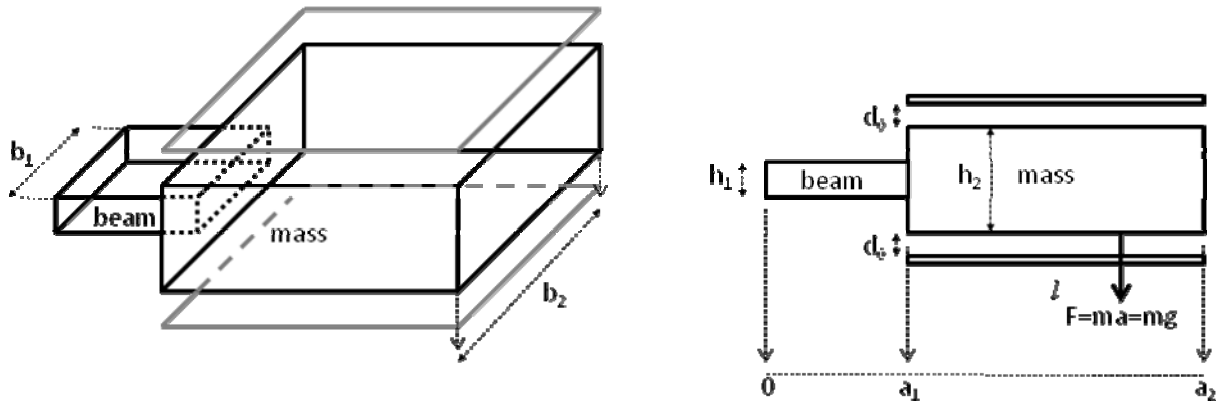


Figure 1. A simplified model for the cantilever beam-mass accelerometer

Figure 2. System interface for C programming

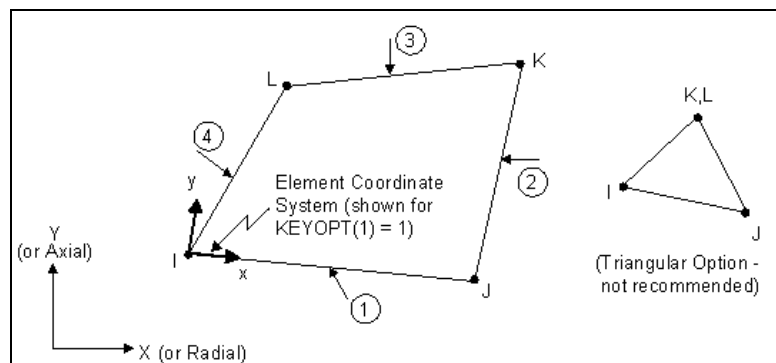


Figure 3. PLANE42 geometry

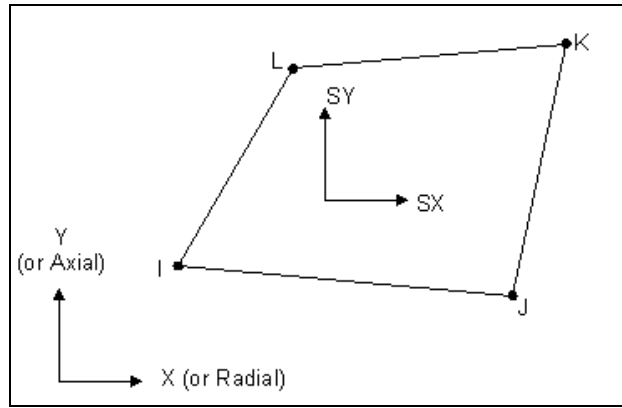


Figure 4. PLANE42 Output data

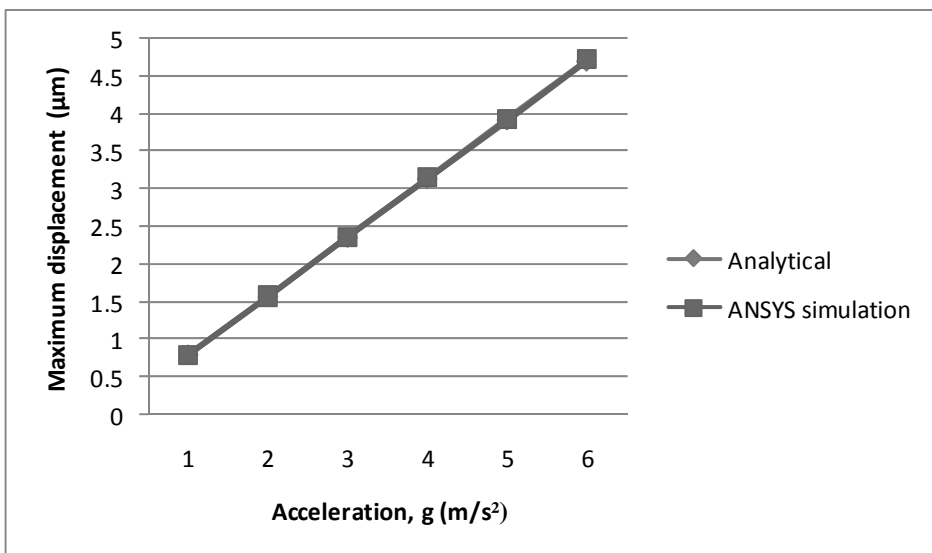


Figure 5. Maximum displacement with respect to applied acceleration for first model

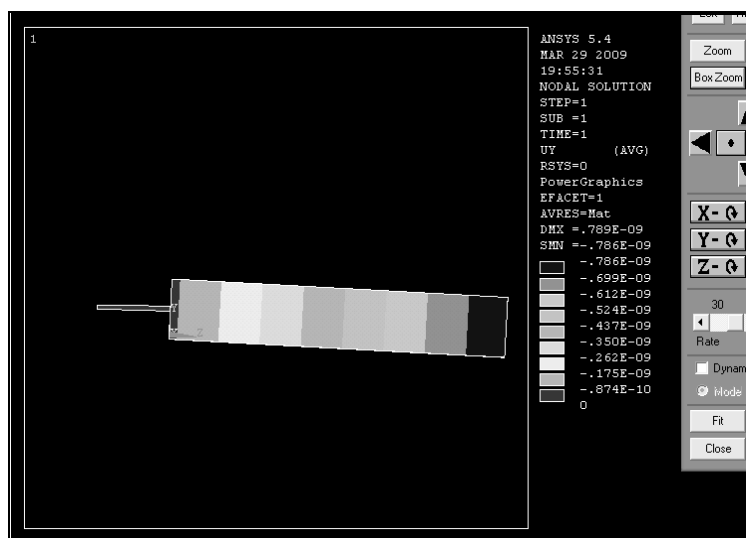


Figure 6. The maximum deflection for 1g

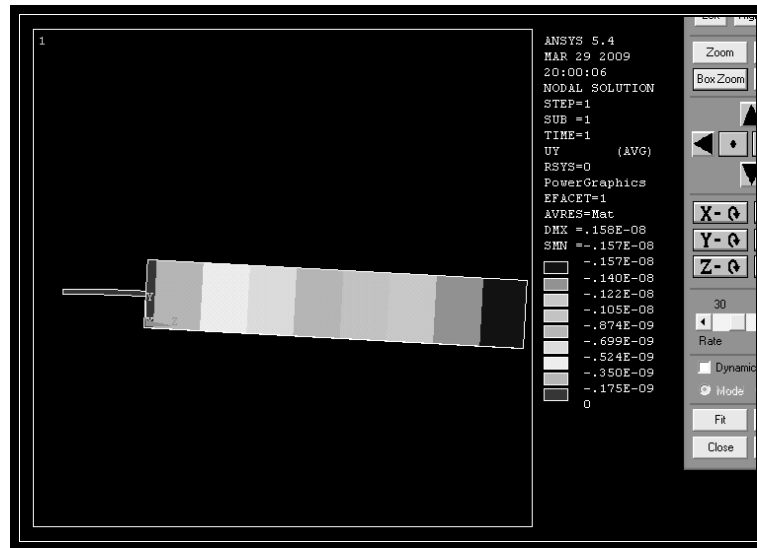


Figure 7. The maximum deflection for 2g

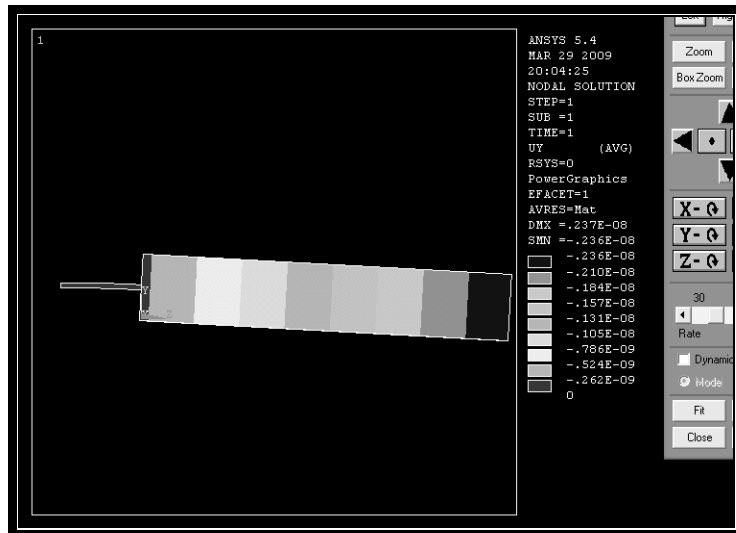


Figure 8. The maximum deflection for 3g

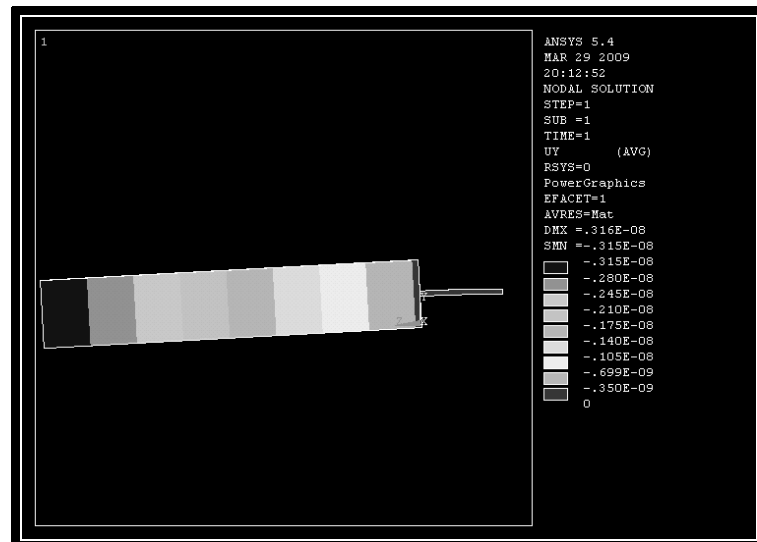


Figure 9. The maximum deflection for 4g

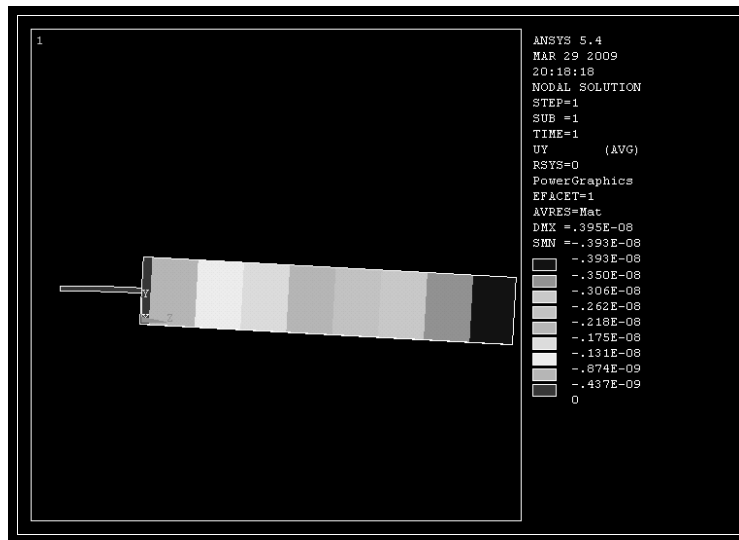


Figure 10. The maximum deflection for 5g

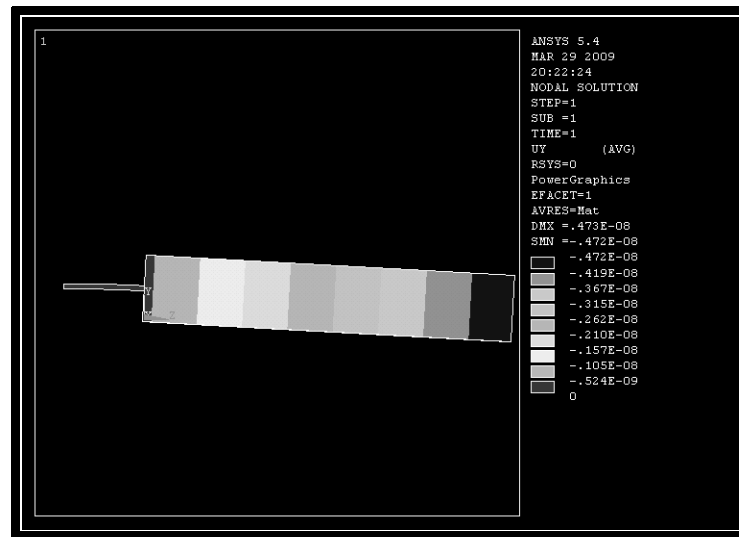


Figure 11. The maximum deflection for 6g

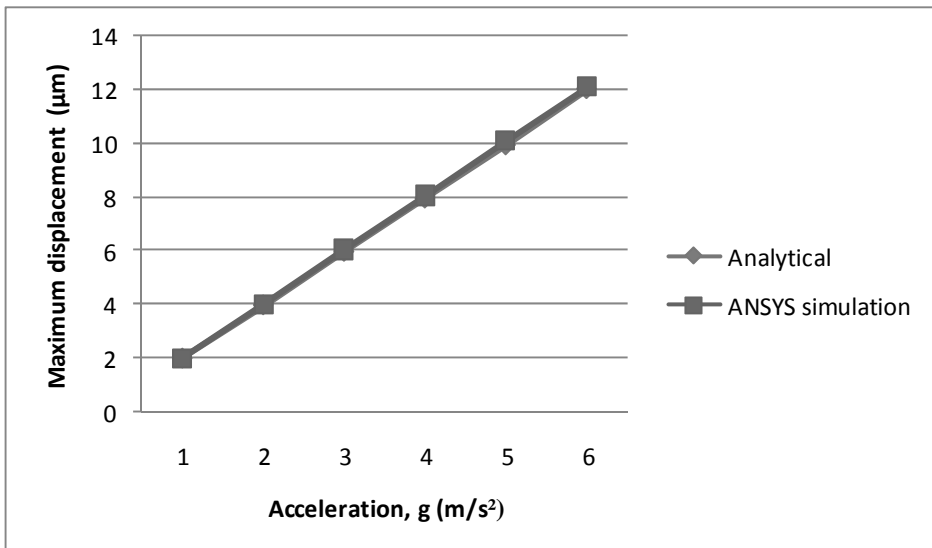


Figure 12. Maximum displacement with respect to applied acceleration for second model

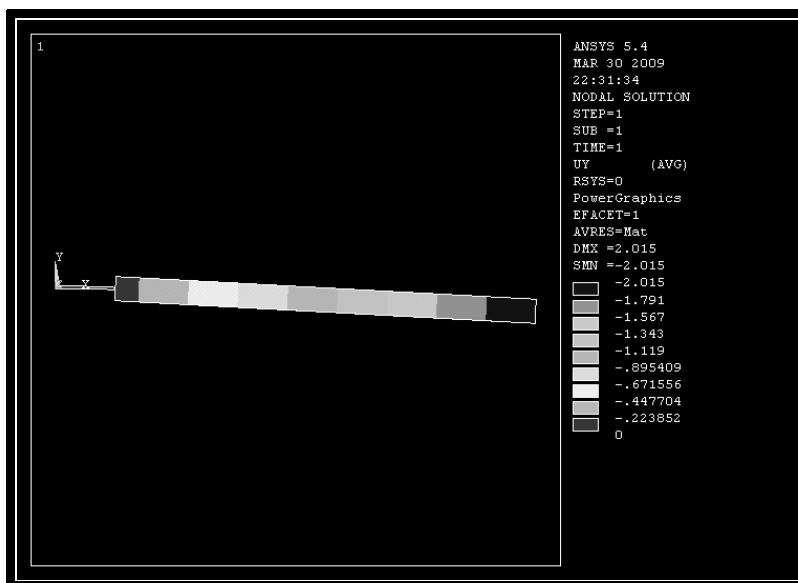


Figure 13. The maximum deflection for 1g

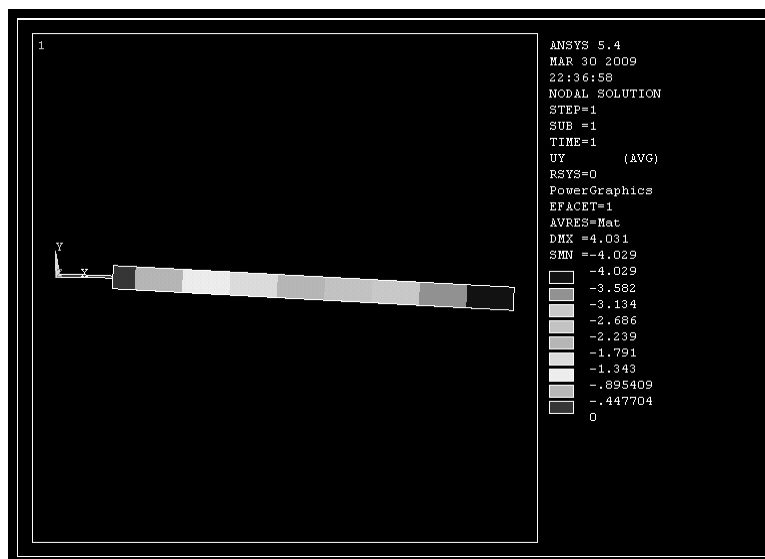


Figure 14. The maximum deflection for 2g

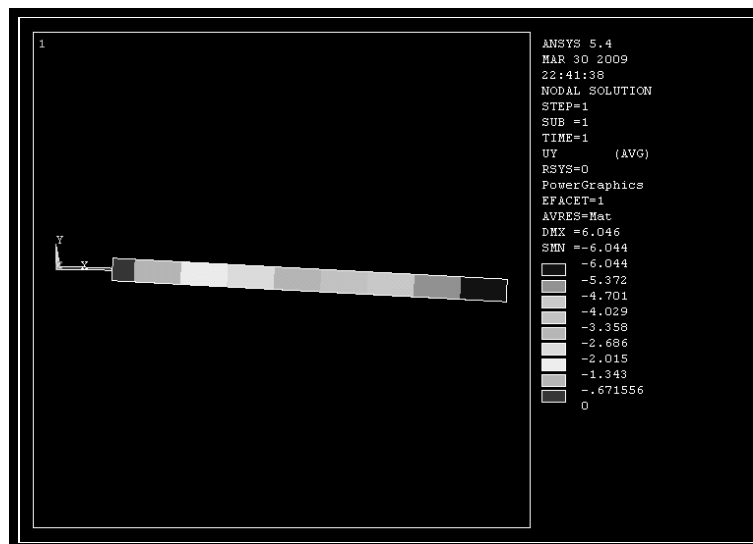


Figure 15. The maximum deflection for 3g

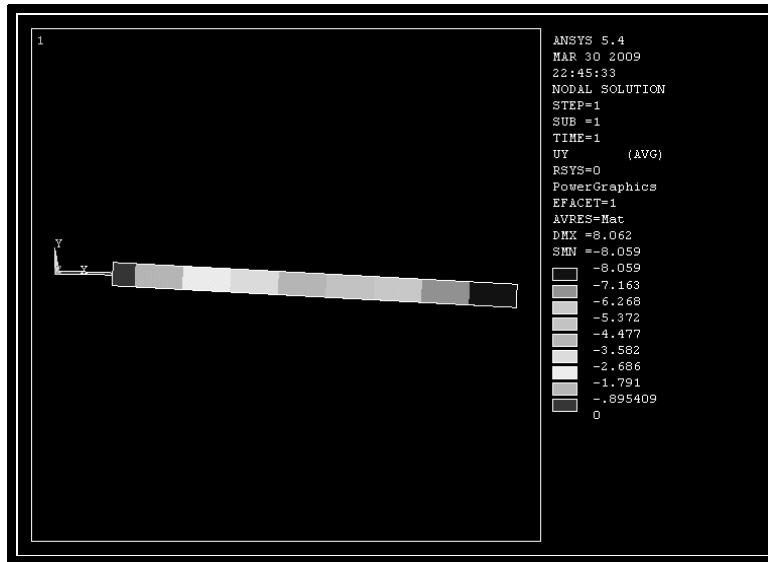


Figure 16. The maximum deflection for 4g

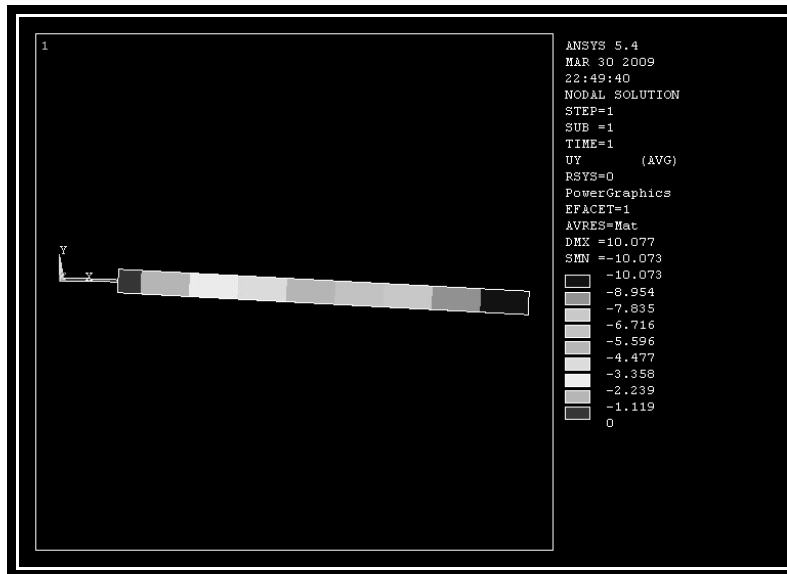


Figure 17. The maximum deflection for 5g

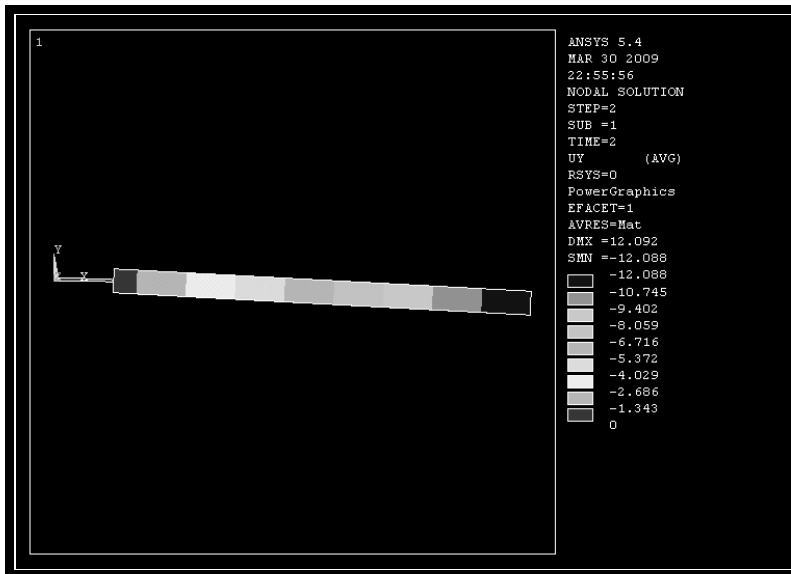


Figure 18. The maximum deflection for 6g

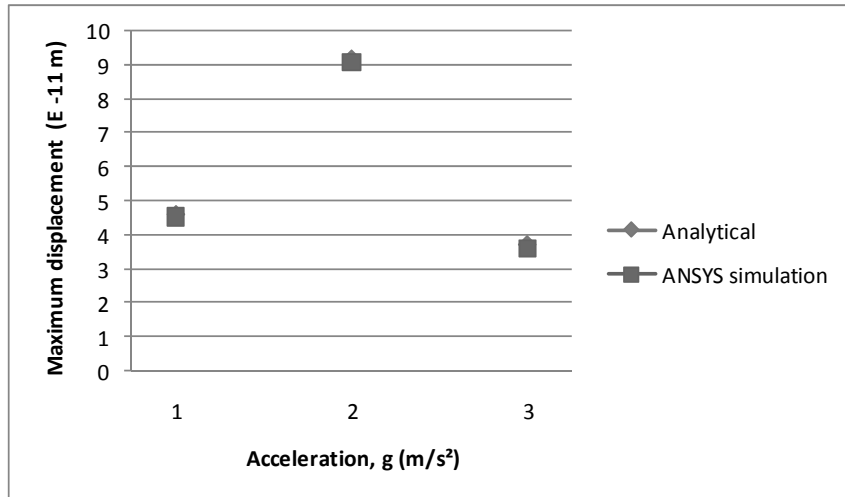


Figure 19. Maximum displacement with respect to applied acceleration for third model

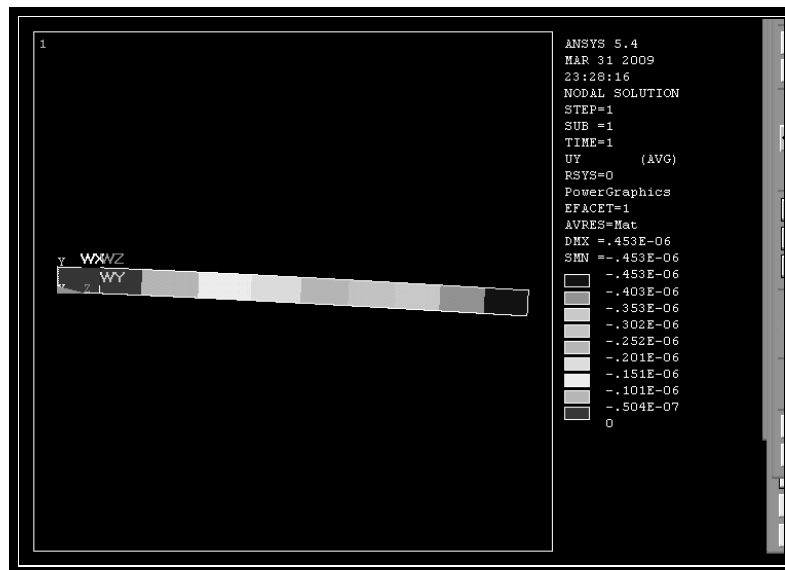


Figure 20. The maximum deflection for 1g

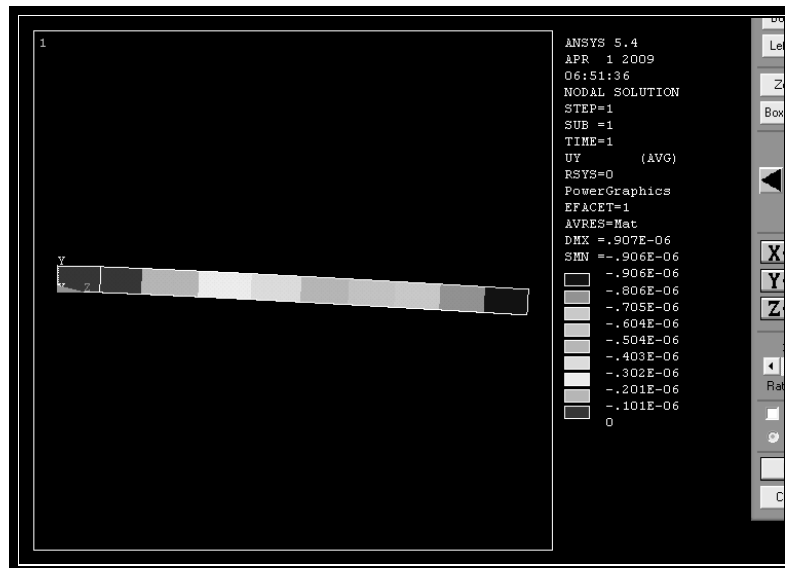


Figure 21. The maximum deflection for 2g

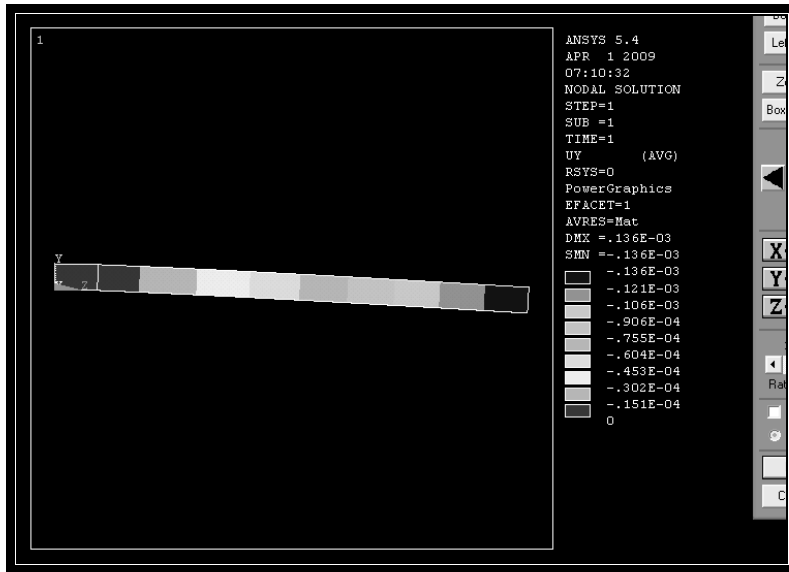


Figure 22. The maximum deflection for 3g



Dynamic Texture Segmentation Using Fourier Transform

Jianghong Li

School of Power and Energy, Northwestern Polytechnical University

Xi'an 710072, China

Tel: 86-029-8846-0464 E-mail: jhli@nwpu.edu.cn

Liang Chen

School of Power and Energy, Northwestern Polytechnical University

Xi'an, Shaan'xi, China 710072

Tel: 86-029-8846-0464 E-mail: xbgydxxs@163.com

Yuanhu Cai

School of Power and Energy, Northwestern Polytechnical University

Xi'an 710072, China

Tel: 86-029-8846-0464 E-mail: caiyh@nwpu.edu.cn

Abstract

Dynamic textures are temporally continuous and infinitely varying sequences of images with certain spatial and temporal stationarity properties and have many potential applications such as computer graphics, computer vision, animation, and computer games. These applications usually require dynamic texture segmentation that is not an easy task especially when the background is cluttered and textured. In this paper, we analyze the spatio-temporal slices of dynamic texture using Fourier analysis and then we propose a simple and efficient approach to dynamic texture segmentation using 3D Fourier transform. Experiments on several dynamic texture sequences show the effectiveness of the proposed approach.

Keywords: Dynamic texture segmentation, Fourier transform

1. Introduction

Dynamic textures are temporally continuous and infinitely varying sequences of images with certain spatial and temporal stationarity properties. Typical examples of dynamic textures include sea-waves, moving clouds, smoke, foliage, fire, walking crowd, and highway traffic. They are common in natural scenes and each of them possesses an inherent dynamics and repetitive pattern. Dynamic textures can easily be perceived by human due to their simplicity and coherence. However, they are difficult to be analyzed as the underlying motion and pattern are often complex and stochastic. The importance of analyzing dynamic textures lies in their relevance to the research areas of computer vision, video processing, and computer graphics. Dynamic textures have many potential applications such as computer graphics, computer vision, animation, computer games, and automated surveillance. In recent years, lots of research efforts have been spent on dynamic texture analysis and synthesis especially in the areas of computer vision and computer graphics. Dynamic texture analysis is to exploit the spatial and temporal properties to characterize or represent dynamic textures for analysis and recognition. While the goal of dynamic texture synthesis is to generate or reconstruct a new video sequence which is similar to the original sequence of dynamic texture without any noticeable artifacts. Both dynamic texture analysis and synthesis usually require dynamic texture segmentation that extract the regions of dynamic textures from a video before performing analysis and synthesis. The spatial extent of dynamic textures (e.g., smoke, fire, flow water) can vary over time and they can also be partially transparent. Therefore, segmenting dynamic textures from a complex background is not an easy task especially when the background is cluttered and textured. This paper considers developing a simple and efficient approach to dynamic texture

segmentation. The rest of the paper is organized as follows. The related work is reviewed in Section 2. The proposed approach is presented in Section 3, and experimental results are demonstrated in Section 4. Final conclusions are summarized in Section 5.

2. Related work

Numerous techniques have been proposed in the literature for dynamic texture segmentation. These techniques can be classified into three major categories: (1) model-based, (2) motion-based, and (3) feature-based techniques. Model-based techniques (M. O. Szummer, 1995)(B. U. Toreyin and A. E. Cetin, 2007)(G. Doretto, A. Chiuso, Y. N. Wu, and S. Soatto, 2003)(A. B. Chan and N. Vasconcelos, 2005)(B. Abraham, O. I. Camps, and M. Sznajder, 2005)(B. Ghanem and N. Ahuja, 2007) are to model the spatio-temporal interdependence among images. Szummer (M. O. Szummer, 1995) proposed the spatio-temporal auto-regressive (STAR) model. In (B. U. Toreyin and A. E. Cetin, 2007)(B. Ghanem and N. Ahuja, 2008), hidden Markov model is adopted to model the dynamic textures. Doretto et al. (G. Doretto, A. Chiuso, Y. N. Wu, and S. Soatto, 2003) derived a stable linear dynamical system model for dynamic textures. In this model, consecutive frames of a sequence are linearly related and viewed as the responses of the linear dynamical system to random noise input. This model has been applied to dynamic texture segmentation (G. Doretto, D. Cremers, P. Favaro, and S. Soatto, 2003). In (A. B. Chan and N. Vasconcelos, 2005), linear dynamical system has been extended to accommodate a mixture of dynamic textures that has been utilized for crowd and traffic segmentation. Abraham et al. (B. Abraham, O. I. Camps, and M. Sznajder, 2005) proposed to identify the underlying linear dynamic system using a set of Fourier descriptors of the image frames rather than the original sequence. All these techniques model the intensity values of a dynamic texture as a stable and linear ARMA process that leads to significant computational expense because the model directly to pixel intensities without mitigating spatial redundancy. To overcome the limitations of these techniques, Ghanem et al. (B. Ghanem and N. Ahuja, 2007) proposed a model that relates texture dynamics to the variation of the Fourier phase, which captures the relationships among the motions of all the pixels within the texture as well as the appearance of texture. Motion-based techniques (T. Amiaz, S. Fazekas, D. Chetverikov, and N. Kiryati, 2007)(S. Fazekas and D. Chetverikov, 2005)(S. Fazekas, T. Amiaz, D. Chetverikov, and N. Kiryati, 2009)(R. Peteri and D. Chetverikov, 2005)(R. Vidal and A. Ravichandran, 2005) are based on motion estimation algorithms in which frame-to-frame motion field is estimated. Motion estimation has been extensively studied and computationally efficient algorithms have been developed. The popular motion estimation algorithm used for dynamic textures is optical flow algorithm. Optical flow is usually based on the assumption of brightness constancy, i.e., the brightness of an object is constant from frame to frame. In addition, most of optical flow algorithms are often suited to estimate local and smooth motion fields. However, the spatial extent of dynamic textures can vary over time rapidly and is often not smooth. These characteristics make it difficult for optical flow algorithm to estimate motion effectively. Feature-based techniques (K. Otsuka, T. Horikoshi, S. Suzuki, and M. Fujii, 1998)(G. Zhao and M. Pietikinen, 2006)(A. Rahman and M. Murshed, 2007) use image features to characteristics of dynamic textures. In (K. Otsuka, T. Horikoshi, S. Suzuki, and M. Fujii, 1998), spatiotemporal motion trajectory is utilized for feature extraction for dynamic textures. Zhao et al. (G. Zhao and M. Pietikinen, 2006) proposed to use local binary pattern, which has been used for 2D textures, to describe dynamic textures for recognition tasks. In (A. Rahman and M. Murshed, 2007), motion co-occurrence matrix is employed to characterize dynamic textures and a segmentation method based on spatial and temporal motion co-occurrence statistics is presented.

3. Dynamic texture segmentation

In this paper, we consider developing an efficient approach to dynamic texture segmentation based on Fourier analysis. The proposed approach is motivated by the work presented in (B. Ghanem and N. Ahuja, 2007), which forms an efficient spatio-temporal model of both the appearance and global dynamics of a dynamic texture using Fourier phase. Before describing the proposed approach, we would like to review the Fourier analysis for dynamic textures.

3.1 Fourier analysis

Fourier analysis has been widely used in image processing as it has several useful properties. Fourier analysis is robust against perturbations that often appear in images, for example, illumination changes and additive noises. The frequency spectrum of an image can be calculated by using the fast Fourier transform (FFT) algorithm that is practical and computationally efficient. In (B. Ghanem and N. Ahuja, 2007), the phase content of a dynamic texture has been demonstrated to be useful for representing its appearance and temporal variations based on the assumption that symmetric Z-transform factors seldom occur in practice. In addition, the temporal variations of phase contents are empirically shown to capture most of dynamical characteristics of a dynamic texture. Motivated by this, we consider using the phase of Fourier analysis for dynamic texture segmentation. Let us choose the sequence "644ce10.avi" from (R. Peteri, S. Fazekas, and M. Huiskes, 2006) as an example. Frame 30 of this sequence is depicted in Figure 1(a). Such sequence mainly contains water waves that can be considered as a dynamic texture and a floating duck

Algorithm 1 The proposed approach to dynamic texture segmentation**Require:** An input image sequence $I(x, y, t)$ **Ensure:** The segmentation mask for each frame

1. **for** t from 1 to T **do**
2. Downsample the current frame of $I(x, y, t)$;
3. Smooth the current frame using 2D Gaussian filter;
4. **end for**
5. Perform 3D FFT for the whole sequence $I(x, y, t)$ using (1);
6. Calculate the phase spectrum using the real and imaginary parts of 3D DFT;
7. Calculate the reconstructed sequence $\hat{I}(x, y, t)$ using (2);
8. **for** t from 1 to T **do**
9. Smooth the reconstructed frame of $\mathcal{I}(x, y, t)$ using the avergaing filter;
10. Compute the mean value $\hat{\mu}(t)$ of the current frame;
11. Convert the current frame into binary image using $\hat{\mu}(t)$ as the threshold;
12. Perform morphological processing, i.e., filling and closing, to obtain binary mask for the current frame;
13. Up-sample the binary mask;
14. **end for**

in a lake. For simplicity, we take a slice of this sequence for analysis. The vertical white line shown in Figure 1(a) is the location of X-T slice, which covers pixels from water waves, the duck, and the background. The corresponding X-T slice image is depicted in Figure 1(b). We take 2D Fourier transform of this slice image using 2D FFT. The log power spectrum and phase spectrum obtained from the Fourier transform are shown in Figure 1(c) and Figure 1(d), respectively. We can see that the phase contains more significant information on the structure in the image than the magnitude. We now consider taking the magnitude and phase separately to reconstruct the slice image using 2D inverse FFT. Figure 1(e) and Figure 1(f) demonstrate the reconstructed slice images using the magnitude and phase, respectively. It is interesting to see that the reconstructed slice image from the phase carries essential information about the water waves, i.e., a kind of dynamic textures. However, the reconstructed slice image from the magnitude provides little information.

3.2 Proposed approach

In this section, we present the proposed approach to dynamic texture segmentation. According to the discussion in Section 3.1, we consider using 3D discrete Fourier transform to process the dynamic textures.

We now describe the details of the proposed approach. Given a gray-level image sequence $I(x, y, t)$ containing dynamic textures where (x, y) is the location of each pixel and t is the frame index. We perform the 3D discrete Fourier transform (DFT) of the input sequence $I(x, y, t)$:

$$F(I(x, y, t)) = \sum_{x=0}^{X-1} (\omega_X^{k_1 x} \sum_{y=0}^{Y-1} (\omega_Y^{k_2 y} \sum_{t=0}^{T-1} \omega_T^{k_3 t} I(x, y, t))) \quad (1)$$

where X and Y are the width and height of each frame, respectively. T is the total number of frames. In (1), $\omega_X = \exp(-2\pi i/X)$ and $k_1 = 0, 1, \dots, X-1$. After performing 3D DFT of $I(x, y, t)$, the phase spectrum $P[F(I(x, y, t))]$ can be obtained by using the real and imaginary parts of $F(I(x, y, t))$. We then compute the reconstructed sequence by performing 3D inverse FFT on the phase spectrum only, i.e.,

$$\hat{I}(x, y, t) = \left| F^{-1} \left\{ e^{iP[F(I(x, y, t))]} \right\} \right|^2 \quad (2)$$

Where $\hat{I}(x, y, t)$ represents the reconstructed sequence.

Each frame of the reconstructed sequence is smoothed by using an averaging filter. Here we select the circular averaging filter with the radius R . The resulting smoothed image is subsequently converted to a binary image by using thresholding. In our approach, the mean value of the image $\hat{\mu}(t)$ is chosen to be the threshold. According to our experimental results, such thresholding technique works quite well. After the binary image is obtained, the morphological processing, i.e., filling and closing, is performed as post-processing step to obtain the segmentation mask for each frame. In order to reduce the computational cost, each frame of the input sequence can be down-sampled and smoothed by a Gaussian filter before performing 3D DFT. In addition, down-sampling the image followed by

smoothing can reduce the noise in the image. If such preprocessing step is employed, the segmentation mask is required to be up-sampled. The proposed approach is summarized in Algorithm 1. It is seen that the proposed approach is quite simple and the most computational expensive step is 3D DFT, which can be computed using efficient 3D FFT.

4. Experimental results

In this section, we test our proposed approach to dynamic texture segmentation for dynamic texture sequences that are available from (R. Peteri, S. Fazekas, and M. Huiskes, 2006). The details of these sequences are described in Table 1. The image size of each sequence is 352×288 . The format of each sequence is MPEG-4 Divx. In all of our experiments, the down-sampling and up-sampling factors are set to 2. The radius of the circular averaging filter is set to 9 for each frame of the reconstructed sequence. The proposed approach is implemented in MATLAB and all the experiments are conducted on a Pentium 4 laptop with 2 GB of RAM.

Figure 2 demonstrates the segmentation results achieved by using our proposed approach to dynamic texture segmentation. The image on the left side of Figure 2(a), (b), (c), (d), (e), (f), (g), (h), (i), and (j) shows the original image, while the image on the right side shows the original image overlaid with the corresponding segmentation mask. We can see that the proposed approach can achieve reasonably good segmentation for dynamic textures especially when the camera is static or the camera motion is small.

5. Conclusions

In this paper, the Fourier analysis for spatio-temporal slices of dynamic texture sequence has been conducted and indicates that the phase spectrum is important for dynamic texture segmentation. Such analysis motivates us to have proposed a simple and efficient approach to dynamic texture segmentation using 3D Fourier transform, which can be computed using FFT. We have applied the proposed approach to a variety of dynamic texture sequences and experimental results show that it is effective for dynamic texture segmentation.

References

- A. B. Chan and N. Vasconcelos. (2005). Mixtures of dynamic textures. *Tenth IEEE International Conference on Computer Vision*, 2005., 1, 2005.
- A. Rahman and M. Murshed. (2007). Segmentation of dynamic textures. *Computer and Information Technology*, 2008. ICCIT 2008, pages 1–6, 2007.
- B. Abraham, O. I. Camps, and M. Sznai. (2005). Dynamic texture with fourier descriptors. Proc. of the 4th Int. Workshop on Texture Analysis and Synthesis, pages 53–58, 2005. Proc. Of the 4th Int. Workshop on Texture Analysis and Synthesis.
- B. Ghanem and N. Ahuja. (2007). Phase based modelling of dynamic textures. *IEEE 11th International Conference on Computer Vision*, 2007.
- B. Ghanem and N. Ahuja. (2008). Extracting a fluid dynamic texture and the background from video. *IEEE Conference on Computer Vision and Pattern Recognition*, 2008, pages 1–8, 2008.
- B. U. Toreyin and A. E. Cetin. (2007). Hmm based method for dynamic texture detection. *IEEE 15th Signal Processing and Communications Applications*, 2007, pages 1–5, 2007.
- G. Doretto, A. Chiuso, Y. N. Wu, and S. Soatto. (2003). Dynamic textures. *International Journal of Computer Vision*, 51(2):91–109, 2003.
- G. Doretto, D. Cremers, P. Favaro, and S. Soatto. (2003). Dynamic texture segmentation. *IEEE International Conference on Computer Vision*, 2:1236–42, 2003. IEEE International Conference on Computer Vision.
- G. Zhao and M. Pietiknen. (2006). Dynamic texture recognition using volume local binary patterns. Proc. ECCV 2006 Workshop on Dynamical Vision, pages 165–177, 2006.
- K. Otsuka, T. Horikoshi, S. Suzuki, and M. Fujii. (1998). Feature extraction of temporal texture based on spatio-temporal motion trajectory. *International Conference on Pattern Recognition*, 1998, 2, 1998.
- M. O. Szummer. (1995). Temporal texture modeling. PhD thesis, Massachusetts Institute of Technology, 1995.
- R. Peteri and D. Chetverikov. (2005). Dynamic texture recognition using normal flow and texture regularity. Proc. Iberian Conference on Pattern Recognition and Image Analysis, pages 223–230, 2005.
- R. Peteri, S. Fazekas, and M. Huiskes. (2006). Dyntex: A comprehensive database of dynamic textures. <http://www.cwi.nl/projects/dyntex>, 2006.
- R. Vidal and A. Ravichandran. (2005). Optical flow estimation and segmentation of multiple moving dynamic textures. *IEEE Computer Society Conference on Computer Vision and Pattern Recognition*, 2005, 2.
- S. Fazekas and D. Chetverikov. (2005). Normal versus complete flow in dynamic texture recognition: a comparative

study. *Int. Workshop on Texture Analysis and Synthesis, 2005. Int. Workshop on Texture Analysis and Synthesis.*

S. Fazekas, T. Amiaz, D. Chetverikov, and N. Kiryati. (2009). Dynamic texture detection based on motion analysis. *International Journal of Computer Vision*, 82(1):48–63, 2009.

T. Amiaz, S. Fazekas, D. Chetverikov, and N. Kiryati. (2007). Detecting regions of dynamic texture. *Lecture Notes in Computer Science*, 4485:848, 2007.

Table 1. Dynamic texture sequences used in our experiments

No.	Sequence	Description
1	“6ammb00.avi”	Small candles with flames
2	“73v192u.avi”	Smoke, fire, and steam
3	“644ce10.avi”	Duck floating on water
4	“645c620.avi”	Highway traffic
5	“648ea10.avi”	Smoke from ventilation system
6	“6481h10.avi”	Water falling over pebbles
7	“6481n10.avi”	A small winding creek
8	“6483b10.avi”	The close up of “6481n10.avi”
9	“6482f10.avi”	A small lake with water ripples
10	“6488610.avi”	Fountain and water ripples



(a) “6ammb00.avi”



(b) “73v192u.avi”



(c) "644ce10.avi"



(d) "645c620.avi"



(e) "648ea10.avi"



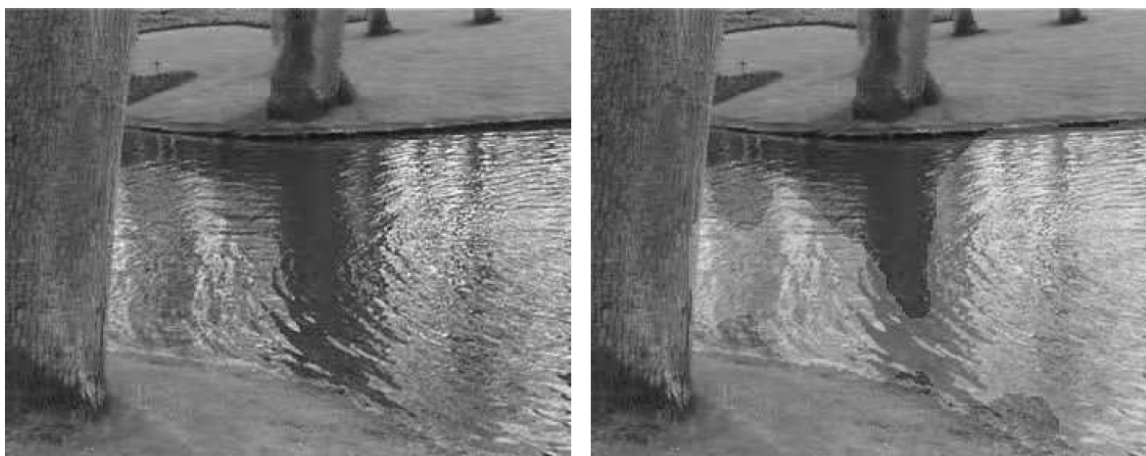
(f) "6481h10.avi"



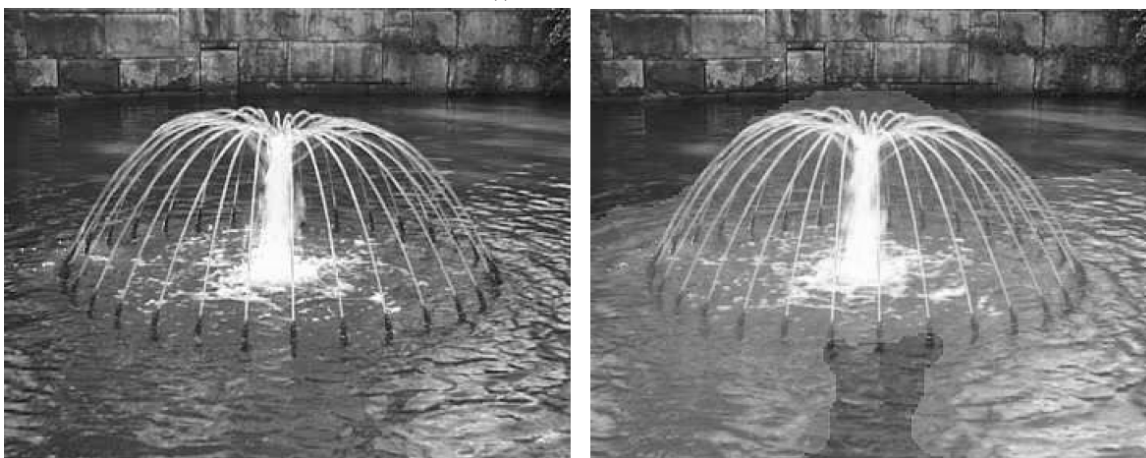
(g) "6481n10.avi"



(h) "6483b10.avi"



(i) "6482f10.avi"



(j) "6488610.avi"

Figure 2. Segmentation results obtained by using the proposed approach for some dynamic texture sequences (R. Peteri, S. Fazekas, and M. Huiskes, 2006). The images on the left and right sides of (a), (b), (c), (d), (e), (f), (g), (h), (i), and (j) depict the original image and the corresponding mask with red color, respectively. This figure is best viewed in color.



Recovery of Nickel (II) Ions from Electroplating Rinse Water Using Hectorite Clay

V.Ramamurthi (Corresponding author)

Department of Chemical Engineering, A.C. College of Technology

Anna University, Chennai- 600 025, India

E-mail: ramamur1951@yahoo.co.in & pgpriya78@yahoo.co.in

P. Gomathi Priya

Department of Chemical Engineering, A.C. College of Technology

Anna University, Chennai- 600 025, India

S.Saranya

Department of Chemical Engineering, A.C. College of Technology

Anna University, Chennai- 600 025, India

C.Ahmed Basha

Pollution Control Division, Central Electro Chemical Research Institute

Karaikudi-630 006, India

Abstract

This paper describes the recovery of Ni (II) from electroplating rinse water using the Hectorite clay. Batch mode adsorption experiments were carried out and the effect of contact time, adsorbent dosage, pH, initial metal ion concentration and temperature were studied. Different isotherms were obtained using nickel electroplating rinse waters of various concentrations. The ion exchange process follows second order kinetics and langmuir isotherm. The paper discusses thermodynamic parameters, including changes in Gibbs free energy, entropy and enthalpy for the ion-exchange of Ni (II) from electroplating rinse water on Hectorite clay, revealed that the ion-exchange process was spontaneous and exothermic under different temperatures. The maximum adsorption capacity obtained was 62.24 mg/g at pH 7-8, the optimum adsorbent dosage and contact time was found to be 2 g/l within 5 hours.

Keywords: Nickel, Hectorite, Rinse water, Adsorption and kinetics

1. Introduction

Heavy metal pollution occurs in many industrial wastewater such as those produced by metal-plating, finishing facilities, dyeing operations, mining and metallurgical engineering, electroplating, nuclear power plants, aerospace industries, battery manufacturing processes, the production of paints and pigments and glass production etc. The presence of heavy metals in the aquatic ecosystem has been of increasing concern because of their toxic properties and other adverse effects on natural waters quality, such as Ni, Cu, Zn, Cr, Cd and Pb. Elevated environmental levels of nickel ions derived from variety of sources. Nickel find its way to water bodies through waste water from metal plating industries, cadmium – nickel batteries and alloys. Exposure to nickel causes decrease in body weight, heart and liver damage and skin irritation. The higher concentration of Ni (II) in ingested water may cause severe damage to lungs, kidneys, gastrointestinal distress, e.g., nausea, vomiting, diarrhea, pulmonary fibrosis, renal edema, and skin dermatitis. It is also a known carcinogen (Axtell et al 2003). Various treatment technologies have been developed for the purification of water and waste water contaminated by heavy metals. The most commonly used methods for the removal of metal ions

from industrial effluents include: chemical precipitation, solvent extraction, reverse osmosis, ultra filtration, ion exchange and adsorption. Among those methods, adsorption has been an effective separation process for a wide variety of applications. Since activated carbon is expensive, an alternate inexpensive adsorbent able to drastically reduce the cost of adsorption system has always been searched. Naturally occurring clay minerals have been very effectively used as adsorbents for the removal of various pollutants from waste water and aqueous solutions. Clays are hydrous alumino silicates broadly defined as those minerals that make up the colloid fraction of soils, sediments, rocks and water. Clay structure is layered with interlayer space and the layers may be electrically neutral or charged. The high specific area, chemical and mechanical stability, variety of structural and surface properties, higher values of cation exchange capacities, etc make clays an excellent group of adsorbents. Presence of both Bronsted and Lewis acidity on clay surface further enhance their adsorption capacity. Clay minerals in soil play the role of a natural scavenger of pollutants from water through both ion exchange and adsorption mechanism. (Baskaralingam et al 2006)

Considering favourable characteristics, adsorption of metal ions and other substances on clays has received considerable attention. For example, illite has been shown to absorb Cd (II) and natural bentonite eliminates zinc from aqueous solution. Removal of Cr (III), Ni (II), Cu (II) and Cd (II) by natural and Na-exchanged bentonites is also reported. (Naseem et al 2001) reported that Pb (II) can be removed from aqueous/acidic solutions by using bentonite as an adsorbent. (Bektas et al 2004) reported the adsorption of lead ions from aqueous solutions by natural sepiolite. (Krishna et al 2006) reported the removal of Cu (II) from aqueous solution by using kaolinite, montmorillonite and their modified adsorbents.

Hectorite is a crystalline sheet structure composed of two layers of silica tetrahedrons and one central dioctahedral layer, which comes under smectite group. It is 2:1 smectite clay, is composed of units made of two silica tetrahedral sheets with a central Mg octahedral sheet. It has permanent negative charges that arise due to the isomorphous substitution of Li^+ for Mg^{2+} . The negative charge is counterbalanced by the presence of inorganic cations on the clay surface (Grim, 1968). The structure of hectorite clay was shown in Figure 1. In this present investigation the batch mode adsorption studies were carried out using hectorite clay

2. Materials and Methods

Nickel chloride hexahydrate, hydrochloric acid, dimethyl glyoxime and ammonia solution are obtained from Ranbaxy fine chemicals Ltd, New Delhi, India. Hectorite was obtained from Clay Mineral Society, CA, USA. **Chemical Formula:** $\text{Na}_{0.3}(\text{Mg},\text{Li})_3\text{Si}_4\text{O}_{10}(\text{OH})_2$ also the properties of hectorite clay was shown in table 1. The amount of nickel present in the solution is determined by using absorbance value noted from UV – Visible Spectrophotometer (HITACHI U 2000 Spectrophotometer).

2.1 Generation of nickel electroplating wastewater

The electrolytic cell is comprised of a set of electrodes viz. copper sheet cathode and nickel anode, placed in the acidic nickel laden solution. An electric current is applied across the electrodes and through the solution. In the acidic nickel bath solution (pH value is 4.8) the copper sheets of surface area $7.5 \times 5.0 \text{ cm}^2$ (of 2 mm thick) is the work piece and nickel metal sheet of surface area as $6.5 \times 5 \text{ cm}^2$ (of 5 mm thick) were used as cathode and anode respectively. The experiment was carried out at a fixed current density (0.024 A/cm^2). The cathode was pre-treated and pickling was done for three minutes to remove dust and rust on the surface. When current is passed through an electrolyte the positively charged metal ions are drawn to the negatively charged cathode where they deposit onto the surface. The electroplating was done in the acidic bath for 10 minutes. One liter distilled water containing tanks were kept to rinse the cathode after electroplating. The rinsing was done for 10 seconds in each tank. The rinse water collected in the first tank (spray rinse and drag out) was not taken for adsorption studies, as it will be used as to make solution for evaporation loss during plating. And the other rinse waters collected were containing heavy metal concentrations from 24.9 mg L^{-1} , 43.4 mg L^{-1} , and 60.8 mg L^{-1} were used for further experiments.

3. Adsorption Studies

Batch adsorption studies were carried out using hectorite clay. All the adsorption experiments were carried out with 50 ml of rinse water solution of required concentrations (24.9 , 43.4 and 60.8 mg L^{-1}) at solution pH in a thermo stated orbital shaker (NEOLAB, Mumbai) at a fixed shaking speed of 150 rpm. The experiments were carried out for various adsorbent dosages, different initial Ni (II) ions concentration, for various contact time, pH and temperature. pH was measured using a pH meter (Elico model LI 120, Hyderabad, India). For the studies on the effect of pH, it was varied from 2 to 12 in metal ion rinse solution concentration of 43.4 ppm and 60.8 ppm . The solution was adjusted to the desired value using 0.1N hydrochloric acid solution and 0.1N sodium hydroxide solution. Temperature studies were carried out for the range of 30°C to 40°C . From the initial and final concentration, percentage removal can be calculated by

$$\% \text{Removal} = \frac{(C_0 - C_f)}{C_0} \times 100 \quad (1)$$

Where, C_0 - initial concentration of nickel in mg L^{-1} ,

C_f - final concentration of nickel in mg L^{-1}

The data obtained in batch model kinetics were used to calculate the equilibrium metal uptake capacity. It was also calculated for adsorptive quantity of nickel by using the following expression:

$$q_e = \frac{V(C_0 - C_e)}{w} \quad (2)$$

Where q_e is the equilibrium metal ion uptake capacity in mg g^{-1} , V the sample volume in litre, C_0 the initial metal ion concentration in mg l^{-1} , C_e the equilibrium metal ion concentration in mg l^{-1} and w is the dry weight of adsorbent in grams.

4. Kinetics of Adsorption

The order of adsorbate - adsorbent interactions has been described by using various kinetic models. Traditionally, the well-known pseudo first-order model of Lagergren has found general use, but second-order kinetics has also been applied with success by various authors to describe the interactions (Krishna et al 2004).

When adsorption is preceded by diffusion through a boundary, the kinetics in most cases follow the pseudo first-order rate equation of Lagergren.

$$\frac{dq_t}{dt} = K_1 (q_e - q_t) \quad (3)$$

where q_t and q_e are the amount adsorbed at time t and at equilibrium, and K_1 is the rate constant of the pseudo first-order adsorption process. The integrated rate law, after applying the initial condition of $q_t = 0$ at $t = 0$, is

$$\log(q_e - q_t) = \log q_e - K_2 \frac{t}{2.303} \quad (4)$$

The plot of $\log (q_e - q_t)$ vs. t gives a straight line for first-order kinetics, which allows computation of the adsorption rate constant, k_1 . If the experimental results do not follow Eqs. (3) and (4), they differ in two important aspects: (i) $k_1 (q_e - q_t)$ does not represent the number of available sites, and (ii) $\log (q_e)$ is not equal to the intercept of the plot of $\log (q_e - q_t)$ against t . In such cases, the pseudo second-order kinetics (Ho et al 2002) given by

$$\frac{dq_t}{dt} = K_2 (q_e - q_t)^2 \quad (5)$$

Where K_2 is the second-order rate constant, and for the boundary conditions $t = 0$ to $t = t$ and $q_t = 0$ to $q_t = q_t$, the integrated form of the equation is

$$\frac{t}{q_t} = \frac{1}{K_2 q_e^2} + \frac{1}{q_e} t \quad (6)$$

The rate constant for intra-particle diffusion (k_{id}) is calculated by the following equation as (Weber and Morris, 1962)

$$q_t = k_{id} t^{1/2} \quad (7)$$

Where q_t is the amount of Ni (II) ions adsorbed (mg g^{-1}) at time t (min) and k_{id} ($\text{mg g}^{-1} \text{min}^{-1/2}$) is the rate constant for intra-particle diffusion. Values of k_{id} were calculated from the slopes of the linear plots of q_t versus $t^{1/2}$.

5. Isothermal Adsorption Studies

5.1 Langmuir isotherm

The Langmuir adsorption isotherm (Langmuir, 1916) was probably the most widely applied adsorption isotherm. A basic assumption of the Langmuir theory is that adsorption takes place at specific homogeneous sites within the adsorbent. The saturated monolayer isotherm can be represented as

$$q_e = \frac{q_{\max} k C_e}{1 + k C_e} \quad (8)$$

Where c_e is the equilibrium concentration (mg L^{-1}), q_e the amount of metal ion adsorbed (mg g^{-1}), q_{\max} for a complete monolayer (mg g^{-1}), where the constant related to adsorption capacity and b is the constant related to the affinity of the binding sites and energy of adsorption (L mg^{-1}).

5.2 Freundlich isotherm

This fairly satisfactory empirical isotherm can be used for non-ideal adsorption and is expressed by the following equation,

$$q_e = K_f C_e^{1/n} \quad (9)$$

where K_F and n are the Freundlich constants related to the adsorption capacity and adsorption intensity of the adsorbent respectively. The Freundlich model (Freundlich, 1906) is more widely used but provides no information on the monolayer adsorption capacity, in contrast to the Langmuir model.

5.3 Redlich-Peterson Model

$$q_e = \frac{K_{RP}C_e}{(1 + a_{RP}C_e^\beta)} \quad (10)$$

Another three parameter Equation (10) known as Redlich - Peterson model (Redlich, Peterson, 1959) where K_{RP} , a_{RP} and β are the Redlich Peterson parameters. The exponent β lies between 0 and 1. When $a_{RP} \rightarrow 0$ isotherm is linear and if $\beta \rightarrow 1$ the isotherm obeys Langmuir. Further when $a_{RP}C_e^\beta \gg 1$, the model reduces to Freundlich isotherm, The Langmuir–Freundlich model.

5.4 Sips model

This is essentially a Freundlich isotherm which approaches an adsorption maximum at high concentrations of adsorbate. An equation mathematically equivalent to the Sips Model (Nitta et al 1984) this equation can also be obtained by assuming that the surface is homogeneous, but that the adsorption is a cooperative process due to adsorbate–adsorbent interactions. The following relation represents this model:

$$q_e = \frac{K_s C_e^{\beta_s}}{1 + a_s C_e^{\beta_s}} \quad (11)$$

where K_s the sips model isotherm constant, a_s the sips model constant and β_s the sips model exponent. When $a_s \rightarrow 0$ isotherm is Freundlich and if $\beta \rightarrow 1$ the isotherm obeys Langmuir model. All the model parameters were evaluated using MATLAB software.

6. Thermodynamic studies

In environmental engineering practice, both energy and entropy factors must be considered in order to determine the spontaneous of the processes. The adsorption process of metal ions can be summarized by the following reversible process, which represents a heterogeneous equilibrium (Tahir et al 2003). The apparent distribution coefficient (K_d) of the adsorption is defined as

$$K_d = \frac{q_e}{C_e} \quad (12)$$

Where C_e the concentration of metal ion on the adsorbent at equilibrium (mg l^{-1}) and q_e is the equilibrium adsorption capacity (mg g^{-1}). The K_d value is used in the following equation to determine the Gibbs free energy of adsorption (ΔG^0)

$$\Delta G^0 = -RT \ln K_d \quad (13)$$

Van't Hoff equation is given by

$$\Delta G^0 = \Delta H^0 - T\Delta S^0 \quad (14)$$

$$\ln K_d = -\frac{\Delta H^0}{RT} - \frac{\Delta S^0}{R} \quad (15)$$

where ΔG^0 is standard free energy change (J), R the universal gas constant ($8.314 \text{ J mol}^{-1} \text{ K}^{-1}$) and T is the absolute temperature (K).

The enthalpy (ΔH^0) and entropy (ΔS^0) can be obtained from the slope and intercept of a Van't Hoff equation of $\ln K_d$ vs. $1/T$

7. Results and Discussion

7.1 Effect of Contact Time on Percentage Adsorption

The dependence of adsorption of Ni (II) using hectorite clay on contact time for various concentrations at a room temperature and solution pH is shown in Figure.2 The adsorption on hectorite clay increased with contact time and attained a maximum value at 5 h for both the solution. Further increase in contact time does not show a significant change in percentage removal (Grim, 1968). It is evident from the results that the contact time required to attain equilibrium is dependent on the initial concentration of heavy metals.

7.2 Effect of Adsorbent Dosage on Percentage Adsorption

To determine the necessary hectorite quantity required for the maximum removal of Ni (II) ions, the adsorbent dosage was increased from the range of 0.01 g to 0.5 g, the effect of hectorite dosage on percentage removal was studied. From Figure.3, it is observed that there is a sharp increase in percentage removal with adsorbent dose for Ni (II). It is apparent that the percentage removal of heavy metals increases rapidly with increase in the dose of the adsorbents due to the

greater availability of the exchangeable sites or surface area. (Selvaraj et al 1998). Hence the optimum adsorbent dosage was found to be 0.1g per 50ml of nickel bearing rinse water effluents.

7.3 Effect of Initial Ni (II) Ions Concentration on Percentage Adsorption

From Fig 4 it can be observed that the percentage removal decreases with the increase in initial heavy metal concentration. Initial metal ion concentration is varied from 24.9 ppm to 60.8 ppm of effluent solution. At lower concentration, the percentage removal is very high and it is lower at higher concentration. This is due to availability of same amount of adsorbent site for various amount of initial metal ion concentration. The maximum removal of 95% was attained at the initial concentration of 24.9ppm due to the other characteristics contents of the effluents may be low.

7.4 Effect of pH on percentage adsorption

pH is one of the most important parameter controlling uptake of heavy metals from wastewater and aqueous solutions. Figure. 5 shows the effect of pH on heavy metal removal efficiencies on hectorite. These studies were conducted at a constant initial metal ions concentration of 43.4 ppm, adsorbent dosage of 0.1g/l solution and agitation period of 5 h for all heavy metal ions at varying the pH (2 to 12) on hectorite. By increasing the pH above 10, the metal ion precipitations take place. The percentage adsorption increases with pH to attain a maximum at pH 7 and thereafter the percentage removal does not change significantly. These results are found in agreement with other studies performed with monmorillonite and bentonite. The mechanism that influences adsorption characteristics of hectorite can be given by dissolution, ion exchange/adsorption and precipitation. From the figure 5, the lowest Ni²⁺ sorption rates were at pH 2. This could be due to the increase in competition for adsorption sites by H⁺. The basic mechanism that governs the adsorption characteristics of hectorite at pH ranging between 6 to 9 is adsorption and ion exchange. At these pH levels exchangeable cations present at the exchangeable sites are exchanged with Ni²⁺ cation in the aqueous solutions (Viraraghavan et al 1994).

7.5 Effect of temperature on percentage adsorption

Fig.6 shows the experimental results obtained from a series of contact time studies for metal ions adsorption with an initial metal ion concentration of 43.4 ppm and 60.8 ppm at solution in which temperature was varied from 25 to 40 °C. The adsorption of metal ions has been found to increase with an increase in temperature from 25 to 40 °C. The increase in adsorption with temperature may be attributed to either increase in the number of active surface sites available for adsorption on the adsorbent or the desolation of the adsorbing species and the decrease in the thickness of the boundary layer surrounding the adsorbent with temperature, so that the mass transfer resistance of adsorbate in the boundary layer decreases. (Naseem et al 2005).

The values of ΔH° and ΔS° were calculated from the slope and intercept of the plot of $\log K_d$ against $1/T$. From these values Gibbs free energy can be calculated. It is evident from the table that values of ΔH° are positive, i.e., endothermic, which is quite contrary to the usual observation. One possible explanation of endothermicity of the enthalpy of adsorption is the well-known fact that ions like Ni (II) are well solvated in water. In order for metal ions to be adsorbed, they have to lose part of their hydration sheath. This dehydration process requires energy. This energy of dehydration supersedes the exothermicity of ions getting attached to the surface. The Gibbs free energy change (ΔG°) is negative as expected for a spontaneous process. The rise in ΔG° with rise in temperature shows that the reaction is more favourable at higher temperature.

7.6 The Pseudo First-Order Kinetics

It is well recognized that the characteristics of sorbent surface is a critical factor that affects the sorption rate parameters. To describe the changes in the sorption of ions studied with time, several kinetic models were tested. A plot of $\log (q_e - q_t)$ vs. time (figure 7) was drawn and the rate constant and q_e were calculated from the slope and intercept of the plot. (Runping Han et al 2005) The plots of $\log (q_e - q_t)$ Vs time were nearly linear with regression coefficients of 0.92-0.98. However the value of q_e calculated from equation does not match with experimental values shown in table.2. Hence the results were further tested for pseudo second-order kinetics.

7.7 The Pseudo Second-Order Kinetics

A plot of t/q_t Vs time (Figure 8) gives very good straight lines. Success with the second order kinetics suggests chemisorption as the rate – controlling step. Rate constant can be calculated from the slope and intercept of the plot and regression coefficients was found to be in the range of 0.99. Thus kinetics for adsorption of nickel on hectorite clay from electroplating effluents fits well to pseudo second-order equation. Table.3 shows the first, second order rate constants and the regression coefficients. It confirms that by increasing the initial metal ion concentration will decrease the second order rate constants.

7.8 Intra particle diffusion

Weber- Morris model was applied to the adsorption of Ni (II) on to hectorite as a function of rinse water concentration and the variation of q_t vs. $t^{1/2}$ was given in Figure 9 respectively. The linear portions of the curve do not pass through

the origin indicating that the mechanism of Ni(II) on hectoite was complex and both the surface adsorption as well as intra particle diffusion contributes to the actual adsorption process. The intra particle rate constants for initial rinse water concentrations for both the resins were obtained from the slope of the linear portions of the plots of qt vs. $t^{1/2}$ and the results were presented in table.2, which gives the values of k_{id} and model constants for the hectoite with respect to initial concentration.

7.9 Isothermal Studies

Duplicate runs for batch mode adsorption experiments were made for each adsorbent to determine the adsorption capacity. Many models have been used to explain adsorption equilibriums, but the most important factor is to have applicability over the entire range of process conditions. The most widely used two parameter adsorption models were Langmuir and Freundlich isotherms where Redlich-Peterson isotherm and sips model were known as three parameter model. The isotherm relate metal uptake per unit weight of adsorbent q_e to the equilibrium adsorbate concentration in the bulk fluid phase. The main reason for the extended use of these isotherm models is that they incorporate constants that are easily interpretable. The constants along with correlation coefficients obtained from these isotherm models are listed in Table 4. The Langmuir sorption model served to estimate the maximum metal uptake values, where they could not be reached in the experiments. The isotherm data were well fitted in all the isotherms. Figure [10-13] present the Langmuir, Freundlich, Redlich -Peterson isotherm and sips isotherm plots for nickel (II) ions adsorption on the hectorite clay using the electroplating effluents containing nickel solutions for different temperatures. Using the MATLAB software the graphs shows the high value of coefficient of correlation, for the adsorbent indicates the models fit well. The application of the Langmuir, Freundlich, Redlich-peterson model and sips isotherm data resulted in better R^2 correlation coefficients ($R^2 = 0.9$) indicates good agreement between experimental and predicted data. Also it clears that the hectorite clay is more effective for heavy metals removal.

8. Conclusion

Thus the adsorption experiments were carried out using hectorite clay for nickel electroplating effluents. The effects of various parameters like contact time, adsorbent dosage, pH, initial metal ion concentration and temperature on the adsorption of nickel from electroplating rinse effluent were studied. The maximum removal of Nickel (II) was found to be 95% for electroplating rinse water at initial concentration of 24.9 mg/l. Equilibrium time was found to be 5 hrs for adsorption from electroplating rinse effluent after which no effective removal was found. The effective adsorbent dosage was found to be 0.1 g per 50 ml of solution for nickel bearing industrial effluents. Optimum pH was found to be in the range of 7 – 8, at which maximum removal of nickel was observed. Effect of temperature was found to be significant as the rate of adsorption increases as the temperature increases. Thermodynamic parameters like ΔH° , ΔS° and ΔG° were calculated. ΔH° values were found to be positive and hence the adsorption process is endothermic. ΔG° values were found to be negative which confirms the spontaneous process. Kinetic studies were done and pseudo second-order equation was found to be fitted well when compared to pseudo first-order equation. Experimental values were fitted with various isotherms for different temperature range (303-313K) and all the isotherms were found using MATLAB software fit well. Maximum adsorption capacity was found to be 62.24 mg/g for adsorption from nickel electroplating effluent.

References

- Axtell, N.R., Sternberg, S.P.K., & Claussen, K. (2003). Lead and Ni (II) removal using *Microspora* and *Lemna minor*. *Bioresour Technol.*, 89, 41- 48.
- Baskaralingam,P., Pulikesi, M., Ramamurthi,V., and Sivanesan,.S. (2006). Equilibrium studies for the adsorption of acid dye onto modified hectorite. *Journal of Hazardous Materials*, B136 989-992.
- Bektas,N., Agim,B.A., Kara,S. (2004). Kinetic and equilibrium studies in removing lead ions from aqueous solutions by natural sepiolite. *Journal of Hazardous materials*, 112, 115-122.
- Freundlich, H. (1906). Uber die adsorption in losungen *Z. Phys. Chem*, 57, 385–470.
- Grim.R.E. (1968).*Clay Mineralogy*, Frank Press, London, 86.
- Ho,Y.S., McKay,G. (2002). Application of kinetic models to the sorption of Copper (II) on peat. *Adsorption Science Technology* 207, 97-815.
- Krishna, G., Bhattacharyya., Arunima Sharma. (2004). Azadirachta indica leaf powder as an effective biosorbent for dyes: a case study with Congo red solutions. *Journal of Environmental Management*, 71, 217-229.
- Krishna, G., Bhattacharyya., Sushmita Sen Gupta. (2006). Kaolinite-montmorillonite and their modified derivatives as adsorbents for removal of Cu (II) from aqueous solution. *Separation and purification Technology*, 50, 388-397.
- Langmuir, I. (1916). The constitution and fundamental properties of solids and liquids, *Journal of the American Chemical Society*, 38, 2221-2295.

- Naseem, R., Tahir,S.S. (2005). Removal of a Vanadium (IV) from aqueous solutios by adsorption process with Aluminium – Pillared Bentonite. *Indian Engineering Chemical Resources*, 44, 6667 – 6684.
- Naseem,R., Tahir,S.S. (2001). Removal of Pb (II) from aqueous acidic solutions by using bentonite as an adsorbent. *Water Resources*, 16, 3982 – 3986.
- Nitta, T., Shigetomi, T., Kuro-Oka, M., and Katayama, T. (1984). An adsorption isotherm of multi-site occupancy model for homogeneous surface. *J. Chem. Engg,Japan* 17, 39-52.
- Redlich, O., Peterson, D.L. (1959). A useful adsorption isotherm. *Journal of Physical Chemistry*, 63, 1024.
- Runping Han., Jinghua Zhang., Weihua Zou., Jie Shi., Hongmin Liu. (2005). Equilibrium biosorption isotherm for lead ion on chaff, *Journal of Hazardous materials*, B125, 266-271.
- Selvaraj,K., Chandramohan,V., Pattabhi,S. (1998). Removal of Cr (VI) from solution and chromium plating industry waste water using photofilm waste sludge. *Indian Journal of Environmental Health* 18, 641-646.
- Tahir,S.S., Naseem Rauf. (2003). Thermodynamics studies of Nickel (II) adsorptions onto bentonite from aqueous solution. *Journal of Chemical Thermodynamics*, 35, 2003-2009.
- Viraraghavan.T., Kapoor.A. (1994). Adsorption of mercury from wastewater by bentonite. *Applied clay science*, 9, 31 – 49.
- Weber, W.J., and Morris, C.J. (1962). Advances in water pollution research in proceedings of the first International Conference on Water Pollution Research, vol. 2, Pergamon Press, Oxford, 231.

Table 1. Properties of Hectorite

Constituents	Percentage (%)
SiO ₂	62.71
MgO	28.39
Li ₂ O	1.17
Na ₂ O	3.23
H ₂ O	4.70
Na	2.40
Mg	17.12
Si	29.31
H	0.53
O	50.10
Li	0.54
Specific surface area (N ₂ area)	63.19(m ² g ⁻¹)
Molecular Weight	383.25 gm
Cation exchange capacity	43.9 mEq/100 g

Table 2. Thermodynamic parameters for the removal of Ni(II) from electroplating rinse effluents

Initial Ni (II) concentration mg/l	ΔH° kJ.mol ⁻¹	ΔS° kJ.mol ⁻¹	ΔG° (kJ.K ⁻¹ mol ⁻¹)			
			T=298 K	T=303 K	T=308 K	T =313K
43.4	125.59	0.424	-0.762	-2.883	-5.002	
60.8	86.02	0.297	-7.122	-3.889	-5.374	
			-2.404			
			-6.859			

Table 3. Kinetic parameters for pseudo first-order, pseudo second order and intra particle diffusion equation for the removal of Ni (II) from electroplating rinse effluents

Initial concentration of Ni(II) mg/l	Pseudo first-order			Pseudo second order			Intra particle diffusion	
	Lagergren rate constant, K ₁ (min ⁻¹).	q _e (mg g ⁻¹)	R ²	Rate constant K ₂ (g mg ⁻¹ min ⁻¹)	q _e (mg g ⁻¹)	R ²	Kid (mg g ⁻¹ min ^{1/2})	R ²
24.9	0.0066	2.038	0.9621	0.0137	11.28	0.9945	0.4413	0.9434
43.4	0.004	2.513	0.9865	0.0038	18.58	0.9804	0.6735	0.9913
60.8	0.0103	3.189	0.9655	0.0023	19.34	0.9979	0.7535	0.9154

Table 4. Adsorption Isotherm Constants for the removal of Ni(II) from electroplating rinse effluents

Temperature (K)		303 K	308K	313K
Langmuir isotherm	q _{max} (mg g ⁻¹)	18.7	22.64	62.24
	b (g ⁻¹)	0.349	0.608	0.4121
	R ²	0.971	0.978	0.93
Freundlich isotherm	K _f	5.32	8.827	17.01
	n	0.377	0.324	0.5615
	R ²	0.983	0.976	0.962
Redlich -Peterson isotherm	K _{RP}	5.87	12.43	8.23
	a _{RP}	0.137	0.442	-0.5
	β	0.5	0.688	0.255
	R ²	0.985	0.985	0.926
Sips isotherm	K _s	5.87	12.43	8.23
	a	0.137	0.442	-0.5
	b	0.5	0.688	0.255
	R ²	0.985	0.985	0.926

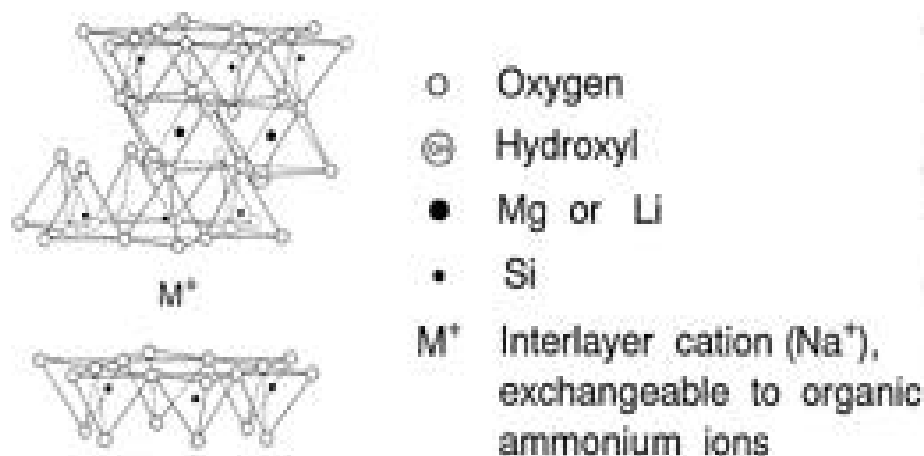


Figure 1. STRUCTURE OF HECTORITE

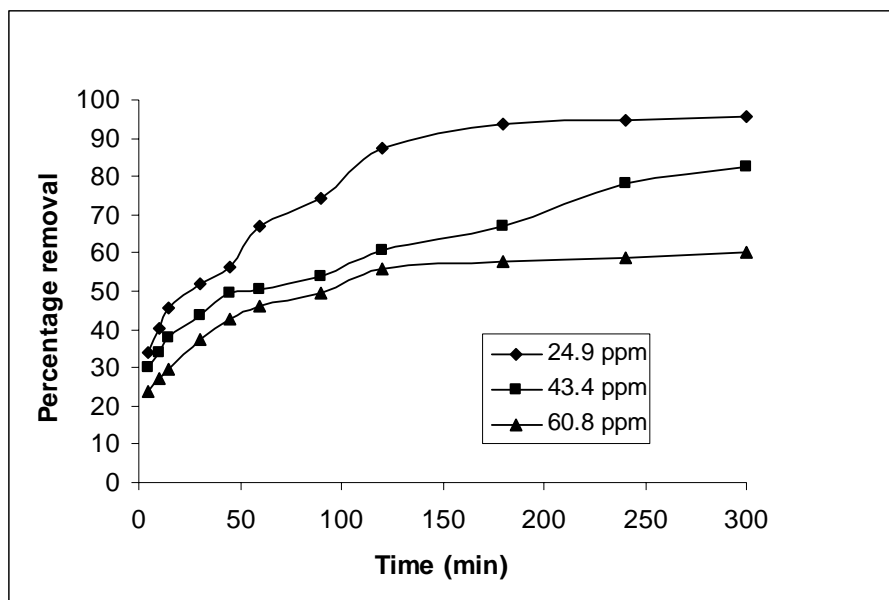


Figure 2. Effect of contact time on percentage removal of Ni (II) from electroplating effluent

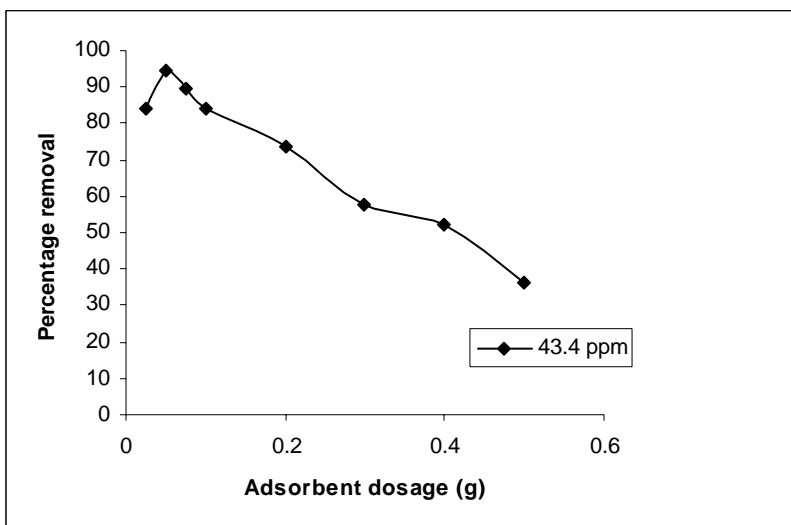


Figure 3. Effect of adsorbent dosage on percentage removal of Ni (II) from electroplating effluent

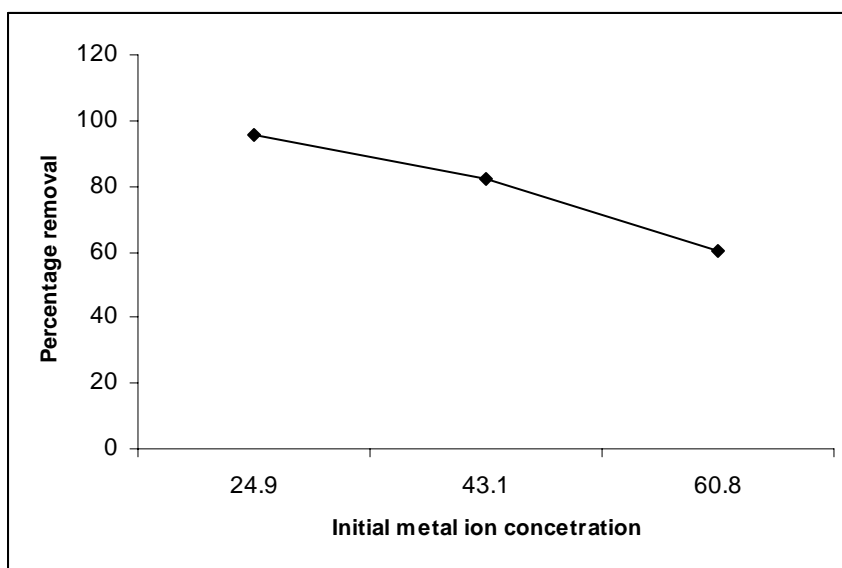


Figure 4. Effect of initial metal ion on percentage removal of Ni (II) from electroplating effluent

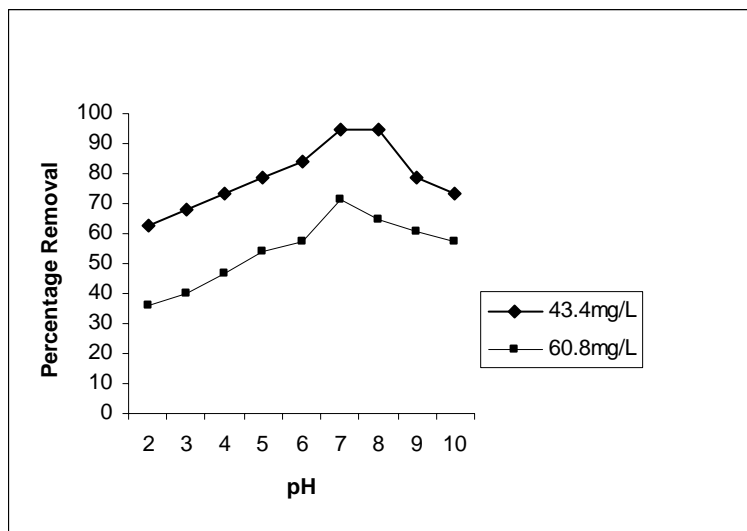


Figure 5. Effect of pH on percentage removal of Ni (II) from electroplating effluent

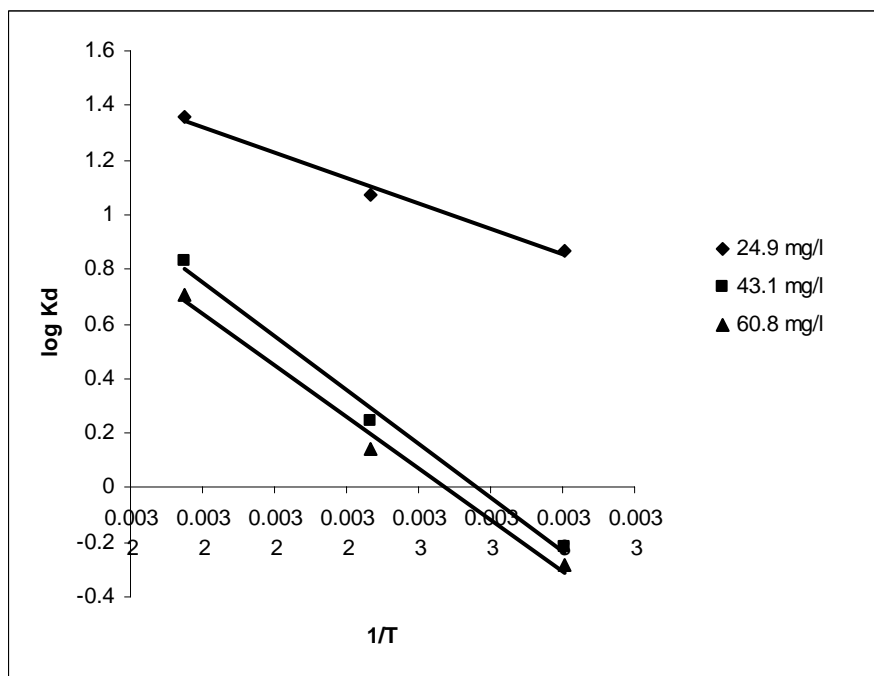


Figure 6. Effect of temperature on percentage removal for the removal of Ni (II) from electroplating effluent

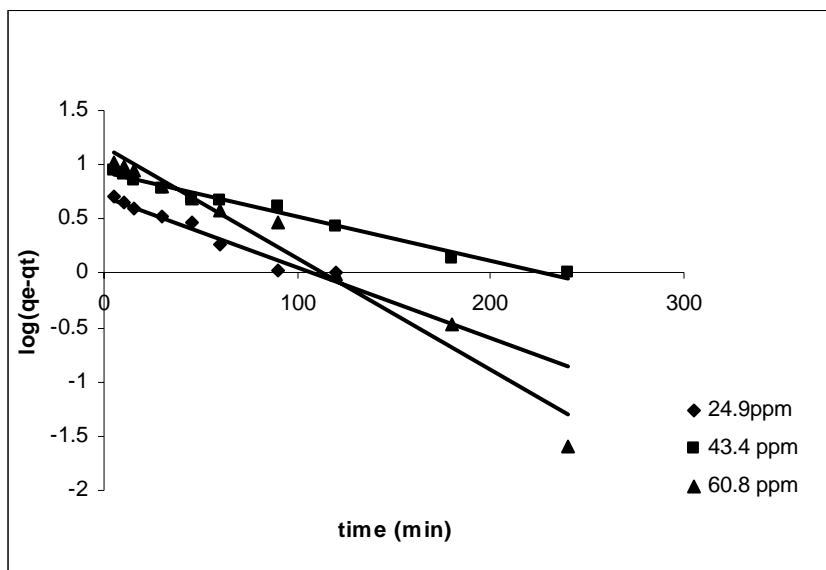


Figure 7. Pseudo – first – order for adsorption of Ni (II) from electroplating effluent

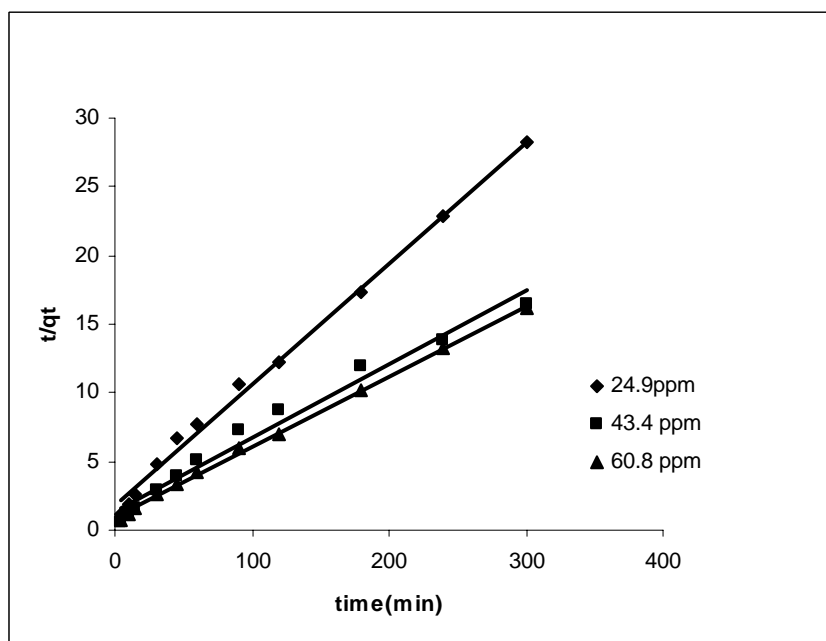


Figure 8. Pseudo – Second– order for adsorption of Ni (II) from electroplating effluent

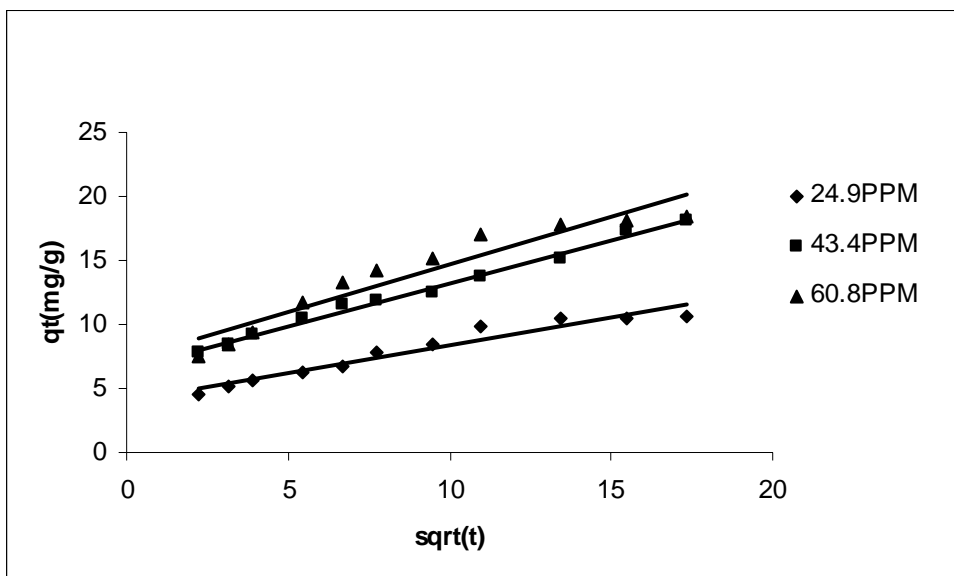


Figure 9. The Intra particle diffusion model for adsorption of Ni (II) from electroplating effluent

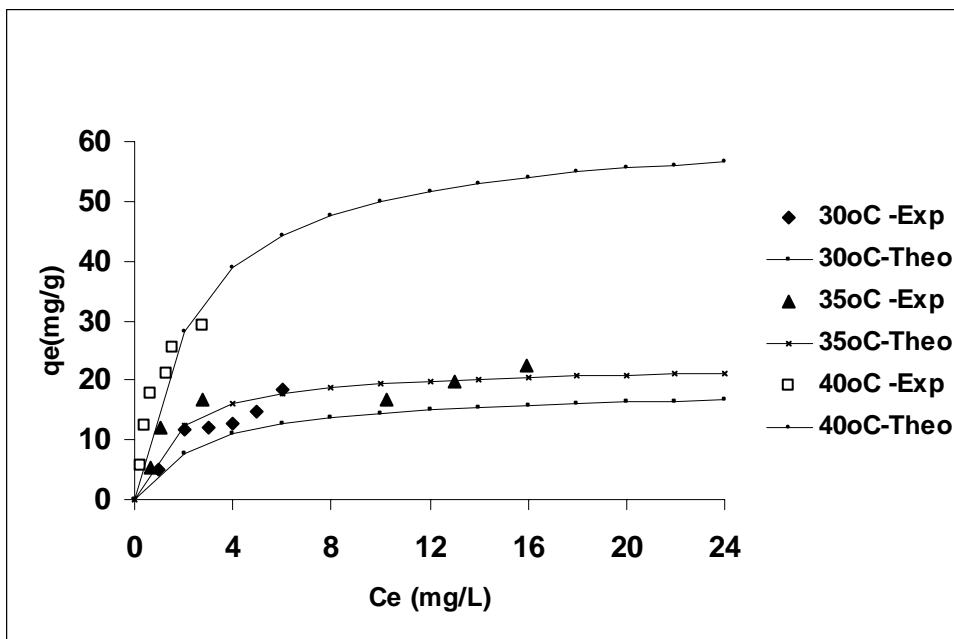


Figure 10. Langmuir plot for adsorption of Ni (II) from electroplating effluent

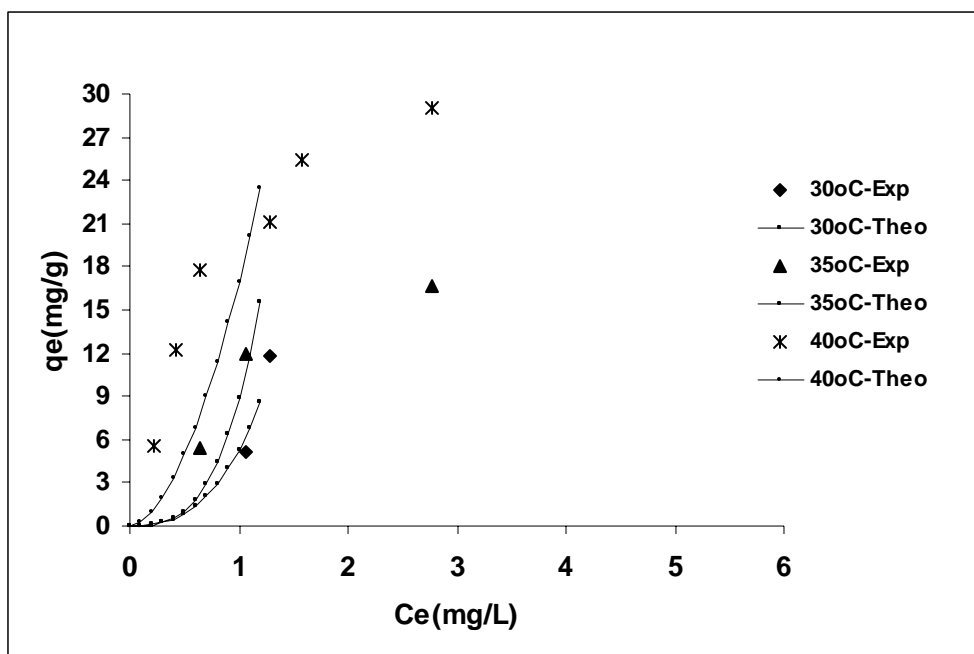


Figure 11. Freundlich isotherm for adsorption of Ni (II) from electroplating effluent

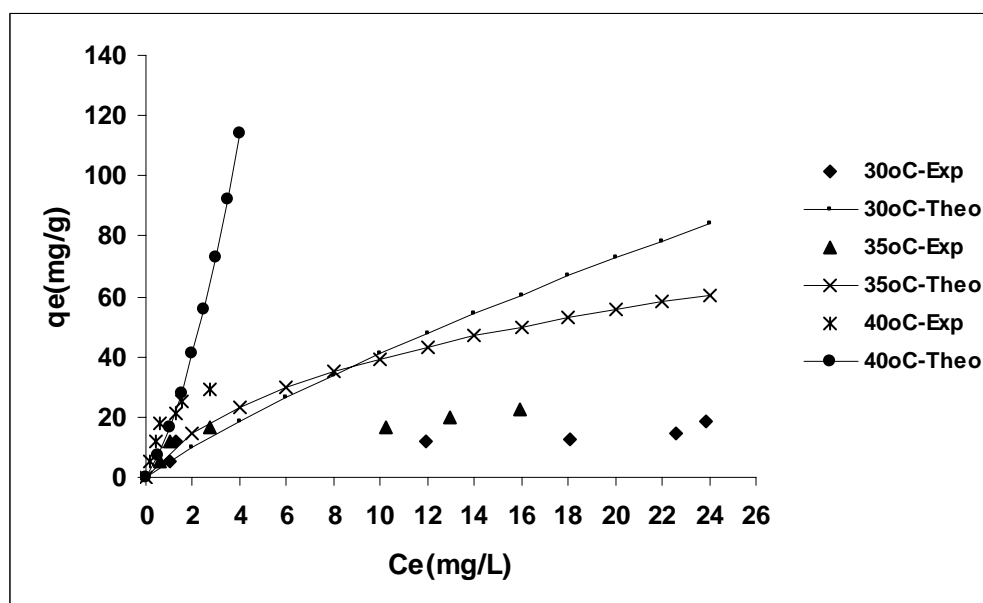


Figure 12. Redlich-Peterson isotherm for adsorption of Ni (II) from electroplating effluent

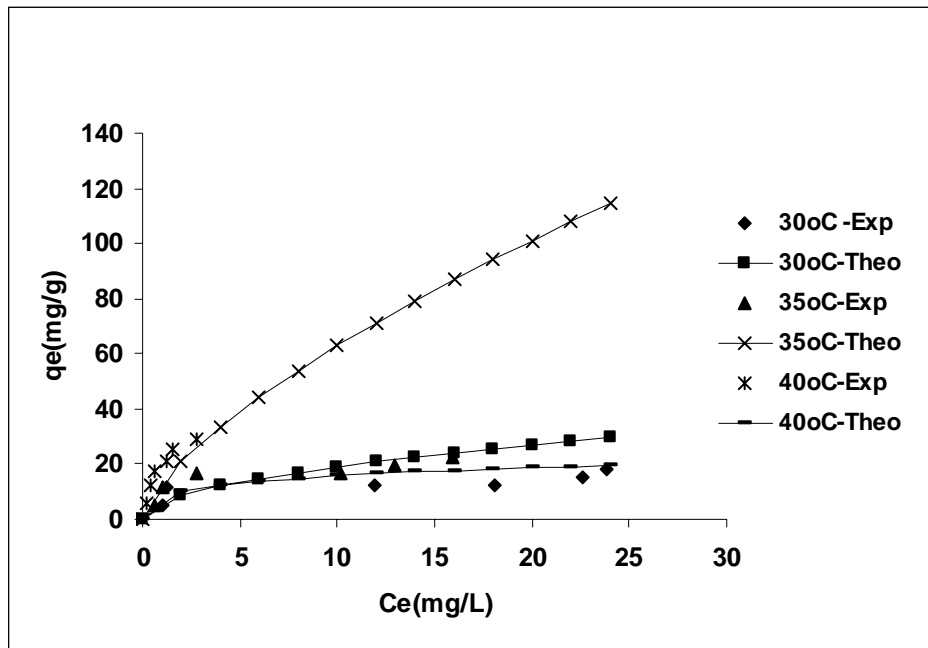


Figure 13. Sips isotherm for adsorption of Ni (II) from electroplating effluent



Study on Design Method of SRC Abnormal Exterior Joint of Large-scale Thermal Power Plant Frame-bent Structure

Xiaoli Yang

School of Civil Engineering, Xi'an University of Architecture and Technology
13 Yan Ta Street, Bei Lin District, PO box 232, Xi'an 710055, China
E-mail: yangxiaoli1228@163.com

Guoliang Bai

School of Civil Engineering, Xi'an University of Architecture and Technology
13 Yan Ta Street, Bei Lin District, Xi'an 710055, China
E-mail: guoliangbai@126.com

Hongxing Li

Northwest Electric Power Design Institute, Xi'an, 710075, China
E-mail: leeredstar9999@yahoo.com.cn

The research is financed by Northwest Electric Power Design Institute.

Abstract

Due to the demand of manufacture technology, the main factory building forms intricate frame-bent structure, many abnormal joints with strong beam-weak column and changed beam and changed column. The bearing mechanism of abnormal joints is very complex, and design of those joints becomes the hard point in the design of large-scale thermal power plant. In order to improve seismic behavior of the thermal power plant frame-bent structure, the research group put forward SRC frame-RC dispersive short-pier shear walls mixed structure, and carried out SRC frame-bent structure sub-space model test. Based on the sub-space model test, the paper chose four typical SRC abnormal exterior joints to take the experimental research. Through the pseudo-static test of the joints, this paper mainly analyses the force-transmission path and bearing mechanism of the SRC abnormal exterior joints, and studies on the main factors which affect the shear capacity of joint. Besides, it puts forward some detailing requirements. Those may be references for practical design.

Keywords: Steel reinforced concrete (SRC) abnormal exterior joint, Bearing mechanism, Force-transmission path, Detailing requirements

1. Introduction

Large-scale thermal power plant is one of the important lifeline projects, and the safety of the main building structure is directly related to the normal supply of the power. Therefore, the main building structure of power plant must have sufficient capacity to resist earthquakes. The joint is a key component in the overall structure which connects the beams with columns, and is the transmission hub of the components of the entire structure. So that safe and reliable joints are the premise for the normal work of the structure. In view of the complex production process and the larger load of the main plant in the thermal power plant, we can use SRC frame-bent with distributed RC shear walls mixed structure as the main plant structure. Thus, the structure of the main plant includes the abnormal joints with complex structure and bearing performance.

At present, the research work on joint is mainly directed against conventional joints. For SRC abnormal joints, there are

some approaches that are based on the concept and experience. So that it lacks a large number of trial bases. Moreover, SRC abnormal joints are imposed by the integrated forces of bending, shear and pressure. At the same time, there are its own abnormal characteristics which give it more complex bearing performance. In this paper, the main research object is SRC abnormal exterior joints. Firstly, it is necessary to clarify force-transferring path and to study on its bearing mechanism and the influencing factors of its shear strength. Then, to put forward some reasonable and practical structural measures to ensure the work of joints is safe and reliable. Thus, it can provide a reference for designing this kind of joints.

2. The overview of test

SRC abnormal exterior joint refers to the joint with high beam, varying column cross-section and some short-pier shear walls laid in the part of the bottom house. Such joints are widely used in industrial and high-rise buildings. To ensure shear failure of the abnormal joints doesn't happen before the structure reach the ultimate capacity state, we need to fully understand bearing and deformation behaviors of the joints. Therefore, our research group carries out the test study on bearing and deformation behavior of SRC abnormal exterior joints under the influence of the low-cycle repeated load.

2.1 Specimen design

The prototype of experimental study model is a certain thermal power plant SRC main power house. It is a twelve-bay, three-span SRC mixed construction system. The test study is based on the studies of seismic behavior of 1000MW generator set main plant three-bay, three-span SRC frame-bent subspace model containing the house with steam engine, the room with deaerators and coal bunker. We select four typical abnormal exterior joints (SJ-1, SJ-2, SJ-3 and SJ-4) to carry out experimental studies.

In accordance with the relative information of joint test (Tang, Jiuru, 1989, P. 370-the last page), the test is designed. Combined with the actual situation in the structure of main plant and laboratory conditions, model scale is 1:5. In view of the production of test specimens, the dimensions of test specimens can be adjusted. However, the principle of adjustment is to try not to change geometric properties and bearing characteristics of the prototype structure.

The design parameters of the specimens are: beam size, cross-section size of column, axial compression ratio, short-pier shear wall etc. Steel reinforcements and profile steel of samples are calculated in compliance with the scale principles and existing relevant norms. Steel bars anchoring and the selection and arrangement of steel need to meet the detailing requirements of the existing norms (Water Resources and Electric Power Press, 1993, P. the whole book; China Building Industry Press, 2002, P. the whole book). Structure types of SRC abnormal exterior joints are shown in Tab.1, the parameters are shown in Tab.2, and arrangements of steel bars are shown in Fig.1.

2.2 Experiment loading and test

2.2.1 Test loading scheme

Experimental study of seismic behavior of SRC abnormal exterior joint adopts pseudo-static loading manner, the joint test is carried out in the structure and seismic laboratory of Xi'an University of Architecture and Technology.

The whole process of the test is manipulated and controlled by MTS electro-hydraulic test servo system, axial load acted on the upper end of column is imposed by 100 tons vertical reaction force loading system, the horizontal low-cycle repeated load is imposed by the electro-hydraulic servo actuator whose displacement range is ± 150 mm. Load-bearing test-bed system is one-way reaction wall which is 12.5 m high, 18m wide, and 2.5 m thick, the bending and shearing capability of its foundation base can meet the test requirements. Test data is recorded by the MTS system computer and TDS-602 static data acquisition instrument, the number of data acquisition channels are about 100~200. After the experiment, we will sort out the test data and make the comprehensive analysis of the test results. The test device is shown in Fig.2.

In order to truly reflect the bearing state of joint in the actual engineering structure, joint test horizontal load is imposed on the upper end of column (Lu, Ying, 2007, P. the whole book) to consider the $P-\Delta$ effect which can not be ignored under the larger axial pressure. According to the axial compression ratio designed, we use constant pressure devices to exert vertical load, and keep the axial pressure constant during the test process. The test adopts force-displacement hybrid control loading system (see Fig.3), before joint samples are yielding, we use load control loading. After joints are yielding, we adopt displacement control cyclic loading until the joints are destroyed.

Test loading process is divided into three steps: first of all, a small preload was imposed to test whether the connection of the equipments and instrumentations are correct, and whether they are work normally; second, according to the formula of 'SRC Composite Structures Technical Specification' (JGJ138-2001) to estimate the bearing capacity of the joints, and to exert stepwise load. Each step load is 30kN imposed in three steps (10 k N per step). When the load is close to the estimated cracking strength (Bai, Guoliang, Zhu, Jianing and Li, Hongxing, 2003, 19, P.12-16), the load step is reduced to half (5 k N per step). Each load step makes once cycle. After per cycle load, we suspend loading.

After the deformation of the joint fully develops, we start to observe the development situation of cracks; finally, after the joint is yielding, we adopt displacement control cyclic loading. We regard the yielding of steel web as a symbol of the joint yielding, and regarded the corresponding maximum displacement at the end of the column as the yielding displacement Δ_j . At first, we imposed load for three times based on the yielding displacement, then imposed cycle load based on 1/3~1/4 yield displacement (according to the damage state course of the joints during experiment courses to control), each displacement is applied for three times until the load get to 80% of ultimate load, and then the test is over.

2.2.2 Test measurement contents

During test process, the horizontal load P is imposed by the load sensor belonged to the actuator at the end of column. Horizontal displacement Δ is measured by the displacement meter with appropriate measurement range at the corresponding position, thus, a P - Δ curve, that is, load-displacement hysteretic curve can be received; the displacement meters with appropriate measurement range are laid at the end of beams and columns, the root of beams and columns, and the top of columns, etc. to measure the displacement of every measuring point, and the P - Δ_i curves are get; the dial indicators are installed in joints core area at a certain angle to measure shear deformation, and to study the shear properties of the joint core area (location of instrumentation is shown in Fig.2). The strain gauge pasted on the measuring points which are on the longitudinal reinforcement, steel, stirrups and external concrete of the beams and columns are used to measure the strain, and used to analyze the joint bearing performance (the case of pasting strain gauges is shown in Fig.4). During the course of the experiment, the development situations of cracks in various loading stages are observed and recorded, and the destruction and deformation situations of joints are shot by the camera and recorded.

2.3 Material properties

The longitudinal stress reinforcement of joints uses HRB335 grade steel, the stirrups use HPB235 grade steel, the profile steel uses Q235 grade ordinary hot-rolled steel. Materials properties tests are carried out in the constructional material testing laboratory in our school as required. And their performance indicators are shown in Tab.3 and Tab.4.

The concrete of the joints is C35 grade commercial ready-mixed concrete. The joint models adopt vertical pouring. And they are supported with wood patterns. The test specimens are maintained in the outdoor natural surroundings. And the test starts after the strength of the joint meets requirements. When the test samples are poured, a group of test cube blocks are set aside, they are maintained in the same conditions as the joint specimens, the mechanical properties of concrete are tested by concrete blocks, and its performance indicators are shown in Tab.5.

Based on the formula- $f_{cu,k} = \mu_{fcu} \times (1 - 1.645\delta_{fcu})$ (China Building Industry Press, 2002, P. the whole book) for calculating the standard strength of concrete the actual standard strength of concrete is calculated to be $f_{cu,k} = 27.57\text{MPa}$, and the corresponding ultimate strain is $875 \mu\epsilon$. It is slightly higher than the normative value.

Wherein:

δ_{fcu} - According to the norms, the coefficient of C35 concrete is 0.13;

μ_{fcu} -Average compressive strength of test cube block.

3. Analysis of test results

3.1 Analysis of force-transmission path

Although the dimensions, reinforcement, axial force, load imposed on every stage of the four test exterior joints are different, the history and patterns of their destruction are similar. They all have gone through initial cracking, thorough cracking, ultimate and failure four stages (Li, Hongxing, Bai, Guoliang and Zhu, Jianing, 2006, 38, P.168-176). The damage situations of the joints are shown in Fig.5. Through the analysis about the state of cracking, deformation and failure during the entire loading process of the joints, we research the force-transmission path.

Before the initial cracking of concrete in the core area, joints work in the elastic state. By the time, the strain of stirrups is very small, the concrete and steel can work together well and both of them bear the shear. In the initial loading term, the beam cracks first. The beam-end tension steel is conveyed into joint core area by the beam steel flange and beam steel reinforcements, and the beam-end pressure is conveyed by the beam steel and concrete. The column steel flange and stiffening rib in the core area bind the concrete intensively, which make the shear capacity of the SRC abnormal joints increase to some extent. As the load increases, the strain gradually reaches the tensile strength of the concrete and the concrete cracks. So the cohesive force between the concrete and steel is gradually reduced. With increasing deformation of concrete, the shear shared by steel and concrete is gradually shared by the steel by itself, so the strain of steel quickly increases and the deformation of joints also develop fast. Going on loading, the strain of steel and the deformation of joints further increase, the steel webs in the core area of joints tend to yield. Because the yielding of the steel is an expansion process from the local to circumference, the shear shared by the steel can continue to increase until

the whole steel yields. Imposed on the repeated loads, the steel gradually yields; the shear shared by the concrete of the core area is increasing. Many crossed cracks come forth in the core area. The cracks divide the core area into many irregular small lozenge-shaped blocks.

Affected on the repeated loads, the crossed cracks of the concrete widen unceasingly, and the stress and strain of the stirrups soon increase. On this stage, its mode of force-transmission is basically the same as the last stage. Due to the larger deformation of concrete, the binding from steel and stirrups to the concrete strengthens and the strength of the concrete increases. As the displacement increases, the concrete are gradually crushed, squeezed out, and gradually withdraw from the work, while the binding effect weakens. Then the shear capacity of the joints begins to attenuate, until the joints reach the failure state. Through the analysis of the destruct ional joint specimen, it is found that the steel web does not warp in the whole process. It shows that steel and concrete of the core area are still bound each other until the joint is destroyed.

3.2 Analysis of bearing mechanism

At present, the common bearing mechanisms include diagonal compression strut mechanism, truss mechanism, shear friction mechanism and binding mechanism and so on. These models are commonly used to analyze the bearing of the conventional joints. Among of them, diagonal compression strut mechanism, truss mechanism and binding mechanism also apply to the abnormal joints.

In the initial loading term, the steel and the concrete in the core area bear the best part of load. At this time, the diagonal compression strut model is used to analyze the bearing performance of the joint. However, the diagonal compression strut is different from the conventional joint. On the initial loading stage, the column steel flange of the SRC abnormal joint can bear pressure together with the steel reinforcements of beam. So that the steel flange can be equivalent to the beam steel bars. The steel web can be equivalent to the concrete of core area, so it can be one of the factors which affect the bearing performance of the diagonal compression strut. Thus, the strength of the diagonal compression strut model is higher than the RC joints.

For the solid-web SRC joint, in such a case that the steel and the concrete bear the best part of load, in addition to shearing resistance, the stirrups can bind the concrete out of the steel, which can strengthen the cohesive force between the concrete and steel, and prevent the yielding of the column vertical steel reinforcements. Therefore, a certain amount of stirrups are needed to be set, particularly the relatively weak scopes of the abnormal joints, such as the part of the variable column cross-section. Stirrups must be closed, and its layout has two methods: cutting across the beam steel web and welding on beam steel.

Because of the changing cross-section of columns, so the axial force has bias that the working characteristic of the diagonal compression strut is not symmetrical when the load reverses. Hence, the width and the inclination angle of the diagonal compression strut in the joint core area are different under the repeated load (see Fig.6). When the column-end is pulled, the diagonal compression strut is located at the intersection zone of beam and the large column, and it slopes to the column outside at a smaller inclination angle. This moment, the diagonal compression strut is wider than that under the reverse load; when the column-end is pushed, the diagonal compression strut is located at the intersection zone of beam and the small column, and it tends to the column inside at a larger inclination angle. At the same time, the diagonal compression strut is smaller than that in the above case, that is, it forms the minor core area. On the effect of the eccentric axial force, the width and the inclination angle of the diagonal compression strut make the scale of compression zone different. Therefore, the outside and inside capacity and damage degree are different. As a result of bearing asymmetry, we can take some measures to ensure that the bearing of the joints is balance and reliable, such as the asymmetric layout of column longitudinal steel reinforcements, the asymmetric shape steel layout and so on.

After the core area of the joint cracks, the force shared by the steel reinforcements and steel gradually increases, but the force shared by the concrete tends to be smooth and steady, and the test specimens come into the stage on which the cracks evenly develop. With the cracking of concrete, the stress of the stirrups and steel web continuously increases. By this time, it is reasonable to use steel truss model to simulate the work of the joints.

The steel flanges and horizontal stiffening ribs of columns form the rigid frame. The diagonal compression strut composed by the concrete and steel web could be regarded as the baroclinic web member of the rigid frame. Column steel web may be regarded as the diagonal tension member of the rigid frame. Those above-mentioned constitute the quintic hyperstatic steel truss shown in Fig.7. The bending moment, axial force and shear transferred from the beam-end and column-end can be equivalent to affect on the steel truss in the joint core area. At the same time, the stirrups of the core area provide the restraining action on it, which can enhance the strength of its own.

The rigid frame of the abnormal joint isn't rectangle but right-angled trapezoid (shown in Fig.8). Under the positive displacement, the strength of the diagonal compression strut is quite high due to the large steel web area in the direction of the main tensile stress, and the main tensile strain is also small. According to the softening theory of the concrete, it is also conducive to maintain the compression strength of the concrete in the direction of the diagonal compression strut;

under the negative displacement, the inclination angle of the diagonal compression strut is smaller than that in the above case, and it will bear further more horizontal force. Therefore, the first crack of the abnormal joints in the core area may occur under the negative displacement, and the bearing capacity under the positive displacement is higher than that under the reverse displacement. The conclusion is in line with the test phenomenon all right.

Through the above analysis, it can be speculated that the steel stiffening ribs of the SRC abnormal joints form the above-mentioned the steel truss model. Assuming that we fit multi-channel stiffening ribs, it will form a multi-layer steel truss or a multi-level hyperstatic model. Thus, the shear strength of the joint can increase, and the seismic capacity can be enhanced. This is an assumption and needs the further experimental and theory research to prove. Multi-layer steel truss model is shown in Fig.9.

Compared with the diagonal compression strut shear failure model of the conventional joint, the internal structure of the SRC abnormal joints is more complex, and its bearing is also more complicated. In the initial loading term, the diagonal compression strut model is established by using the baroclinic field theory of the core area concrete, and its surrounding steel and stirrups can provide an effective constraint on it. On the whole, the binding diagonal compression strut-steel truss model (Wang, Peixin, 2008, P. the whole paper) is applied to analyze the bearing mechanism of the conventional joint; while for the SRC abnormal joint, its applicability has yet to be proved by more experimental and theory analysis, and then it can be spread the application.

3.3 Analysis of shear strength influencing factors

As the weak link of the structure, the joint is the key force-transmission junction. In the structural design, the bearing capacity of joints must be greater than that of the various components that are connected with it, that is to say, when the other components fail, the joints can also transmit internal force reliably under the combined effect of the earthquake and vertical load. There are a lot of factors influencing the shear capacity of SRC abnormal joints, such as profile steel, horizontal stirrups, column longitudinal steel reinforcements, orthogonal beams, the grade of concrete, the axial pressure, short-pier shear walls, construction techniques, etc. In this paper, we mainly analyze that profile steel, horizontal stirrups, the axial pressure and short-pier shear walls affect the shear strength of the joints.

1) Profile steel

Regarded as an important factor, the profile steel bears part of the outer load, and moreover, steel web is one of the main factors resisting shear. The steel flange-frame binds the concrete of the core area, so that the initial cracking strength and the ultimate strength of those joints are higher than the RC joints. The initial cracking strength of the joint SJ-3 with SRC-beam is about 20% higher than the joint RC SJ-2 with RC-beam (shown in Tab.6).

2) Horizontal stirrups

the horizontal stirrups is one of the factors resisting shear of the SRC joints, but its shearing resistance impact is fully exerted after the steel web yields, and its impact is weaker than the profile steel. Through experimental analysis, it is known that the rate of joint stirrups has almost no impact on the initial cracking strength of the joints. With the cracking of concrete, the truss model gradually forms, and the force shared by the stirrups increases. The stirrups can not only effectively bind the deformation of concrete and compression yielding of column longitudinal steel reinforcements to improve the strength of concrete, but also bear a part of shear. So that it delays the destruction of the joints and improved the ductility of the joints. Therefore, the minimum stirrup ratio of SRC joint should be determined with double criteria of the ductility and strength. When the joint fails, the stirrups of the core area don't yield simultaneously. The figure 10 shows the change of stress distribution of stirrups along core height with the load increasing. Taking into account the asymmetry of bearing, the stirrup resistance item in the bearing capacity formula should be reduced by multiplying a reduction factor. At present, the factor usually gets 0.8, which is safe for the test joint design.

3) Axial pressure

Because of the binding of the profile steel and stirrups, the axial pressure makes the concrete of the core area in the three dimension stress state (shown in Fig.11), which inhibits the cracking of concrete. After the cracking of concrete, the axial pressure also makes the larger mechanical friction formed between the concrete blocks, so that a moderate axial compression ratio can enhance the shear strength of the joints.

However, if the axial pressure exceeds the critical value, the concrete will be crushed, and the shear strength will reduce. The axial compression ratio critical value of the SRC abnormal joint is higher than the RC abnormal joint. That is to say SRC structure can withstand much more axial pressure than that of RC structure.

Due to the changing cross section of columns, the eccentric axial force forms, which will cause the stress of the joint area to superimpose, and the destruction of the eccentric side is serious. The stiffness, ductility and energy dissipation performance of the overall joint will decrease with the increase of eccentric bending moment. Under eccentric axial force, the distribution of cracks of the entire joint is non uniform, and the main cracks occur in the eccentric side of the axial force. The greater the axial force is, the greater the eccentric moment is, and the more seriously the joint damages.

Therefore, it should be further studied whether the beneficial effect of the axial pressure to shear capacity of SRC abnormal joint would be considered.

4) Short-pier shear wall

As can be seen from Tab.6, the skeleton curve peak of the joint SJ-1 with the vertical wall is higher than that of the joint SJ-2 without walls, the joint strength increases by about 20%; the skeleton curve peak of the joint SJ-4 with the two-way walls is higher than that of the other joints, and its strength is about 50% higher than the joints without the walls. Through the above comparative analysis, it can be seen that the vertical wall can also enhance the bearing capacity of the joint, but the effect is not obvious compared with the wall in the loading direction. As can be seen from the backbone curve of joints (see Fig.12), the strength and stiffness degradation of the joint SJ-4 is more gentle, especially in the declining stage, it shows the good ductility. All in all, the short-pier shear wall can improve the strength and stiffness and improve the seismic performance of the joint, such as ductility, energy dissipation performance and so on.

4. Conclusions and suggestions

1) In SRC frame-tent structure, the longitudinal steel reinforcements and stirrups are needed to form steel skeleton which can not only bear part of the load, but also bind the deformation of the internal concrete, while the concrete also ensure the stability of the steel. The stirrups should adopt intensive layout in the parts that is prone to damage, but the construction must be convenient and viable. In the layout of the steel reinforcements, if the steel web needs to be cut through, the steel cross-section loss rate should not exceed 25% of its web area (Metallurgical Industry Press, 1998, P. the whole book).

2) As the loading and bearing of the test abnormal exterior joint are asymmetrical, the column longitudinal steel reinforcements laid in the inside and outside of the joint may be asymmetric. The more longitudinal steel reinforcements of joint column are laid in the lateral of the joint where it is prone to damage, which must meet the requirement of steel reinforcement spacing. Or the steel flange or web can be thickened to enhance the weak side, or steel plate is welded on the weak side, and so on. Putting forward those measures is to ensure that the bearing of SRC abnormal exterior joint is balanced and harmonious.

3) Through the analysis of joint force-transmission path, we can see that the bearing of this kind of joint is very complex. So that it needs the more experiments to research on it.

4) Through the analysis of bearing mechanism, we can speculate that if we set multi-channel stiffening ribs in the joint core area, it will form a multi-layer steel truss or a multi-level hyperstatic model. Thus, the shear strength of the joint can increase, and the seismic capacity can be enhanced. However, the above content is an assumption and needs the further experimental and theoretical research to prove it.

5) Through the analysis of the shear bearing capacity influencing factors of the SRC abnormal exterior joint, we preliminary know about the bearing characteristics of it and the influencing degree of each component. It is a basis for the further research on the shear bearing capacity calculation of this kind of joints. Besides, we know the short-pier shear wall can improve the strength and stiffness and improve the seismic performance of the joint, such as ductility, energy dissipation performance and so on.

6) In the world, we can see the advantage of this kind of joints. However, for SRC abnormal joints, there are steel, steel reinforcements of columns and beams, the horizontal stirrups, some additional steel members and concrete, etc. in the joint core area, so its structure is very complicated. Besides, the type of the joint in the SRC power plant main building structure is much, such as beam-column joint, beam-wall-column joint and so on. The joint forms with good seismic performance which are received based on the test analysis must meet the feasibility of the construction. We should sort out a set of systemic standard collective drawing of SRC joint to guide design and construction. It is a long-term work and needs further in-depth experiment study and detailed theoretical analysis.

References

Bai, Guoliang, Zhu, JiaNing, Li, Hongxing. (2003). The anti-crack calculation of reinforced concrete frame abnormal joint. *World Earthquake Engineering*, 2003,19 (3):12-16.

Li, Hongxing, Bai, Guoliang, Zhu, Jianing, et al. (2006). Experimental research on seismic behavior of abnormal joint in reinforced concrete frame. *Journal of Xi'an University of Science and Technology*, 2006,38 (2) :168-176.

Lu, Ying. (2007). Experimental research and analysis for restoring force characteristics of steel high-strength high-performance concrete frame joints. Xi'an University of Architecture and Technology, 2007.

People's Republic of China national standard. *GB 50010-2002 Code for Design of Concrete Structures*. Beijing: China Building Industry Press, 2002.

People's Republic of China national standard. *GB 50011-2001 Code for seismic design of buildings*. Beijing: China

Building Industry Press, 2002.

People's Republic of China power industry standard. *DL5022-93 Technical regulation for design of civil structure of fuel power plants*. Beijing: Water Resources and Electric Power Press, 1993.

People's Republic of industry standards. *YB 90082-97 Design specification of steel reinforced concrete composite structure*. Beijing: Metallurgical Industry Press, 1998.

Tang, Jiuru. (1989). *Aseismic reinforced concrete frame joints*. Nanjing: Southeast University Press, 1989.

Wang, Peixin. (2008). *Experimental Research and Analysis of the residual ultimate strength and stiffness degradation of Steel-Reinforced High Strength and High Performance Concrete Frame Joints*. Xi'an: Xi'an University of Architecture and Technology, 2008.

Table 1. SRC abnormal exterior joints test structure type

Joint number	column	beam	Remarks
SJ-1	SRC-column	RC-beam (700 mm high)	To set up vertical walls
SJ-2	SRC-column	RC-beam (700 mm high)	-
SJ-3	SRC-column	SRC-beam (500 mm high)	-
SJ-4	SRC-column	RC-beam (700 mm high)	To set up two-way wall

The other details are seen in Table2 and Figure1.

Table 2. SRC abnormal exterior joints test design parameters

Test specimen number		SJ-1	SJ-2	SJ-3	SJ-4		
column	upper column	b × h (mm)	250×240	250×240	250×240	250×240	
		profile steel	H140×90×4×6	H140×90×4×6	H140×90×4×6	H140×90×4×6	
			(2.65%)	(2.65%)	(2.65%)	(2.65%)	
		steel (ρ _s) reinforcement	6φ12	6φ12	6φ12	6φ12	
			(1.13%)	(1.13%)	(1.13%)	(1.13%)	
	stirrups (ρ _{sv})	φ8@100	φ8@100	φ8@100	φ6@100		
		(0.40%)	(0.40%)	(0.40%)	(0.23%)		
	volumetric percentage of stirrups (ρ _v)	(0.94%)	(0.94%)	(0.94%)	(0.53%)		
	below column	b × h (mm)	250×280	250×280	250×280	250×280	
		profile steel	H180×90×4×6	H180×90×4×6	H180×90×4×6	H180×90×4×6	
(2.50%)			(2.50%)	(2.50%)	(2.50%)		
Steel (ρ _s) reinforcement		6φ12	6φ12	6φ12	6φ12		
		(0.97%)	(0.97%)	(0.97%)	(0.97%)		
stirrups (ρ _s)	φ8@100	φ8@100	φ8@100	φ6@100			
	(0.40%)	(0.40%)	(0.40%)	(0.23%)			
volumetric percentage of stirrups (ρ _v)	(0.86%)	(0.86%)	(0.86%)	(0.48%)			
the core area of joints	stirrup (ρ _s)	φ6@120	φ6@120	φ6@125	φ6@100		
		(0.20%)	(0.20%)	(0.20%)	(0.23%)		
	volumetric percentage of stirrups (ρ _v)	(0.40%)	(0.40%)	(0.40%)	(0.48%)		
beam	b × h (mm)		200×700	200×700	200×500	200×700	
	steel (ρ _s) reinforcement	upper Steel (ρ _s) reinforcement	4φ20	4φ20	2φ16	4φ20	
		(0.95%)	(0.95%)	(0.43%)	(0.95%)		
	below steel (ρ _s) reinforcement	4φ20	4φ20	2φ16	4φ20		
		(0.95%)	(0.95%)	(0.43%)	(0.95%)		
profile steel			H400×60×5×6	(4.43%)			
stirrups (ρ _s)	φ10@100	φ10@100	φ8@100	φ10@100			
	(0.79%)	(0.79%)	(0.51%)	(0.79%)			
shear wall	b × h _w (mm)	longitudinal wall	-	-	longitudinal wall	transverse wall	
		80×220	-	-	80×220	80×450	
	vertical distributed steel reinforcements (ρ _s)	16φ5	-	-	16φ5	12φ5	
		(2.01%)	-	-	(2.01%)	(0.71%)	
	horizontal distributed steel reinforcements (ρ _s)	φ4@60	-	-	φ4@60	φ4@60	
(0.53%)		-	-	(0.53%)	(0.53%)		
axial compression ratio		0.25	0.15	0.15	0.25		
grade of concrete		C35	C35	C35	C35		

Table 3. Steel bar materials performance

steel-bars diameter	detailed parameters	F_s (kN)	F_y (kN)	f_s (Mpa)	f_y (Mpa)	E_s (Mpa)	ε_y ($\mu\varepsilon$)	ε_s ($\mu\varepsilon$)
3.5	3.6	7.25	-	712.629	-	2.1×10^5	-	339 3
6	6.4	16.3	-	506.942	-		-	241 4
8	8.1	23	-	446.569	-		-	212 7
10	9.9	34.5	-	448.414	-		-	213 5
12	11.75	66	44.25	608.974	408.289	2.0×10^5	204 1	304 5
16	15.4	121	82.5	649.942	443.142		221 6	325 0
18	16.9	138	90.5	615.511	403.651		201 8	307 8
20	19.1	171	113.5	597.117	396.332		198 2	298 6

Table 4. Profile steel materials performance

steel type	width	thickness	F_y (kN)	F_s (kN)	f_y (Mpa)	f_s (Mpa)	E_s (Mpa)	ε_y ($\mu\varepsilon$)	ε_s ($\mu\varepsilon$)	$\bar{\varepsilon}_y$ ($\mu\varepsilon$)	$\bar{\varepsilon}_s$ ($\mu\varepsilon$)
4	49.9	3.6	60	81	334.001	450.902	2.06×10^5	162 1	218 9	165 9	224 3
4	50.5	3.6	63.5	86	349.285	473.047		169 6	229 6		
5	50.8	4.4	71	104	317.645	465.283		154 2	225 9	155 0	226 4
5	49.6	4.4	70	102	320.748	467.375		155 7	226 9		
6	50.3	5.7	88	125	306.930	435.981		149 0	211 6	154 1	203 8
6	53	5.7	99	122	327.706	403.840		159 1	196 0		

Table 5. Concrete materials performance

Test specimen number	actual dimension (cm^3)	area of cross section (mm^2)	actual bearing load (N)	actual strength (Mpa)	modulus of elasticity (Mpa)	ε_u ($\mu\varepsilon$)
1	15×15×15	225 00	820 000	36.444	3.15×10^4	115 7
2	15×15×15	225 00	690 000	30.667		974
3	15×15×15	225 00	900 000	40.000		127 0
4	15×15×15	225 00	685 000	30.444		966
5	15×15×15	225 00	805 000	35.778		113 6
6	15×15×15	225 00	835 000	37.111		117 8

Table 6. SRC abnormal exterior joints test loads

Joint	test cracking load (kN)		test ultimate load (kN)		cracking load /ultimate load (%)		axial compression ratio
	Push	Pull	Push	Pull	Push	Pull	
SJ-1	70	-60	105	-106	67	57	0.25
SJ-2	50	-60	80	-92	63	65	0.15
SJ-3	60	-60	80	-80	75	75	0.15
SJ-4	120	-80	203	-122	59	66	0.25

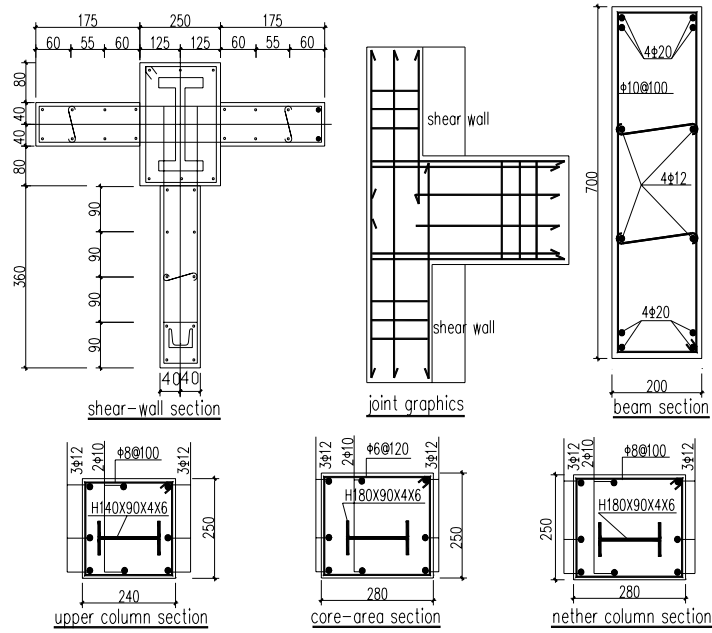


Figure 1. SRC abnormal exterior joints test working drawing

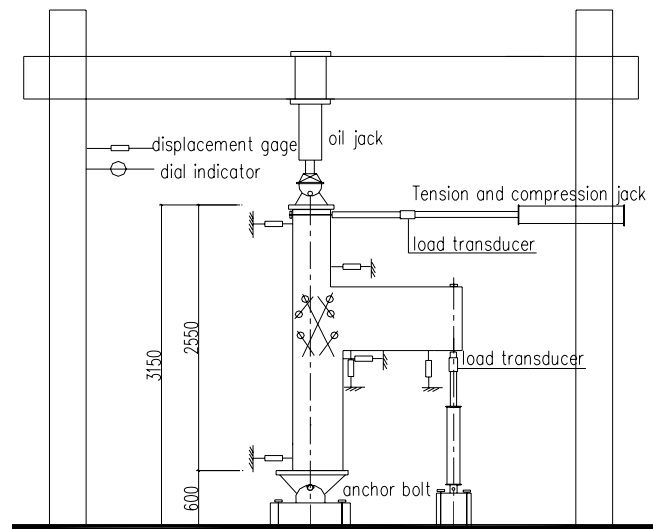


Figure 2. SRC abnormal exterior joints test setup drawing

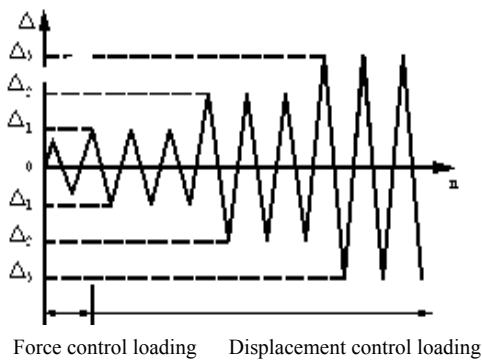


Figure 3. Test loading system of the test joint

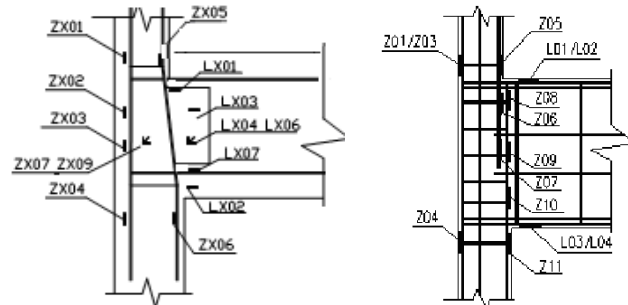


Figure 4. Arrangement of strain gauges in the test joint

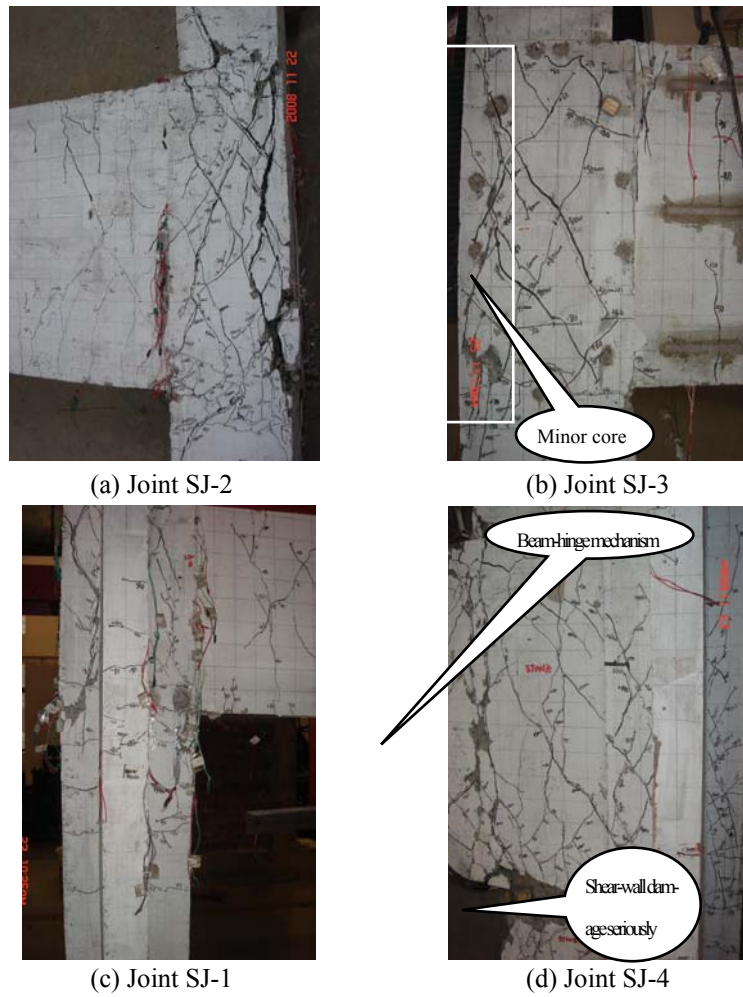
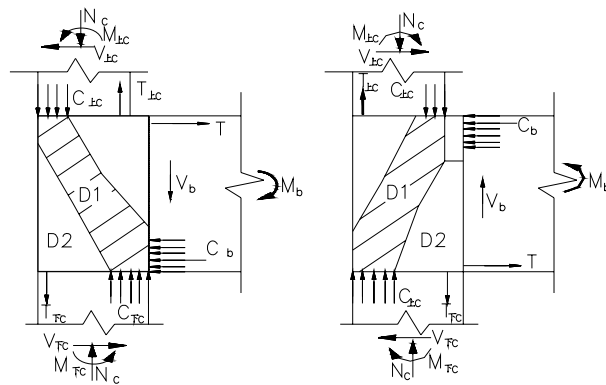


Figure 5. Damage situations of the test joints



(a) Column-end is pulled (b) Column-end is pushed

Figure 6. The bearing analysis of SRC abnormal exterior joints

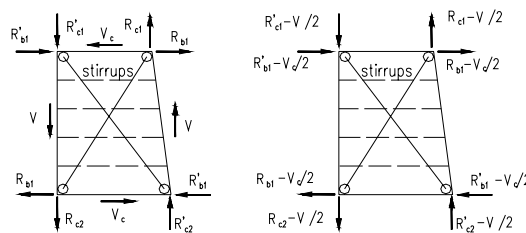


Figure 7. Steel truss model of test joints

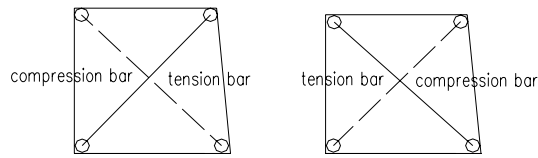
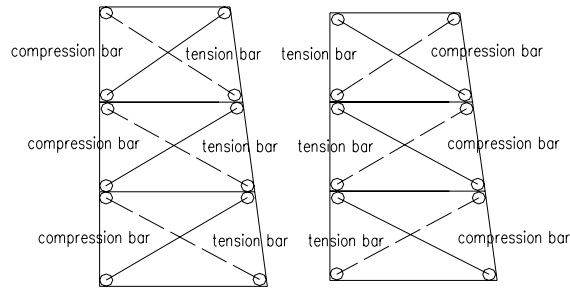


Figure 8. Tensile-compressive strut model of test joints



(a) Positive (push) displacement (b) Negative (pull) displacement

Figure 9. Multi-layer steel truss model of the joint

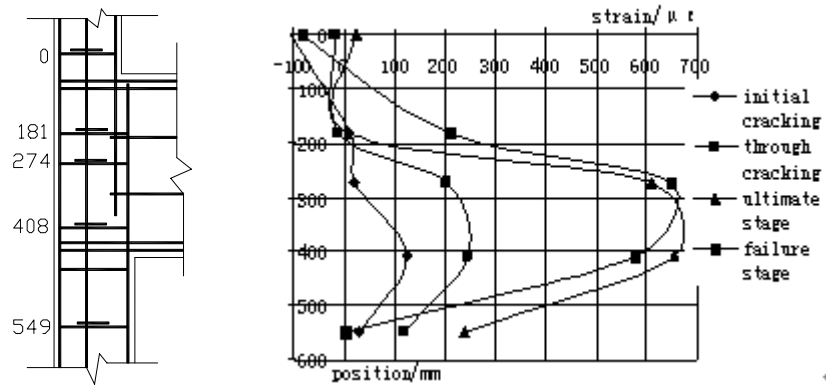


Figure 10. Strain analysis of stirrups in the joint core area

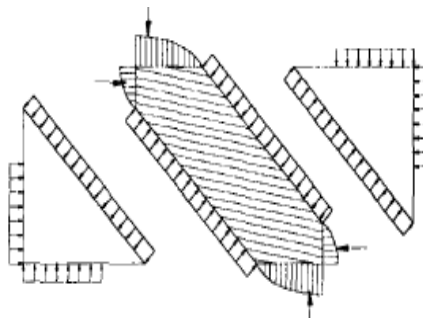


Figure 11. Surrounding concrete restricted diagonal struts

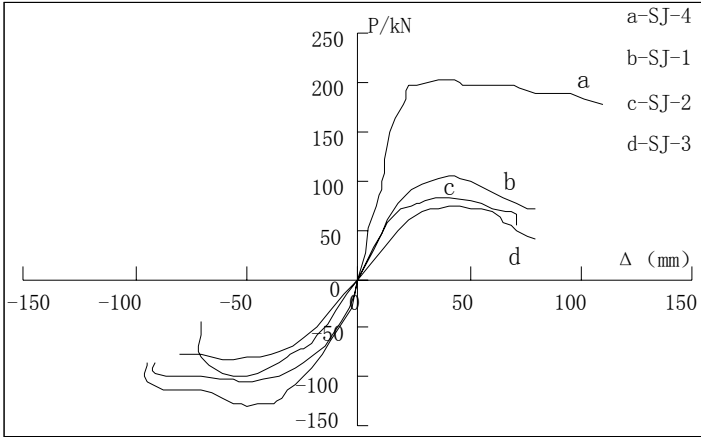


Figure 12. Backbone curve of test joints